Search for tZ production at the Large Hadron Collider

Artur Amorim

Mestrado em Física
Departamento de Física e Astronomia
2015

Orientador
Doutor Nuno Filipe da Silva Fernandes Castro,
Investigador Auxiliar no Laboratório de Instrumentação e Física Experimental de Partículas

Todas as correções determinadas pelo júri, e só essas, foram efetuadas.

O Presidente do Júri,

Porto, ______/______/_________

Artur Amorim

Search for tZ production at the Large Hadron Collider

Departamento de Física e Astronomia

Faculdade de Ciências da Universidade do Porto
Outubro de 2015

Artur Amorim

Search for tZ production at the Large Hadron Collider

Tese submetida à Faculdade de Ciências da
Universidade do Porto para obtenção do grau de Mestre
em Física

Departamento de Física e Astronomia
Faculdade de Ciências da Universidade do Porto
Outubro de 2015

"I was early taught to work as well as play,
My life has been one long, happy holiday;
Full of work and full of play-
I dropped the worry on the way-
And God was good to me everyday."
John D. Rockefeller

Acknowledgements

First of all, I would really like to thank Dr. Nuno Castro for being a very supportive and patient advisor. I learned from you a lot of Physics and had an amazing year thanks to the opportunities you gave to me. In the difficult times you managed to make me confident that I would achieve my goals.

My friend Juan Pedro Araque, thanks a lot for helping me, without your expertise in programming this thesis would be much harder. With your advice and support I expanded my programming skills to a level I would not achieve if you did not encourage me.

Many thanks to José Santiago and Rui Santos for their help in developing the UFO model used in this work. I also thank José Santiago for his hospitality during my stay in Zurich. It was an amazing experience working in particle physics with a large group of motivated people.

I would like to thank the whole LIP team for their constant support, especially João Pedro and Natália for being there every time I had to deal with paperwork.

I also have many thanks to some of my friends and colleagues, especially André Gonçalves for the amazing conversations about Physics and hilarious discussions about hedonistic lifestyle; Ester Simões for presenting me to LIP and for help; João Azevedo and Pedro Faria for the long friendship, great moments together including trips to other side of the world, trails and interesting talks. Thanks also to João Moura, Mafalda Monteiro and Tiago Lima for the moments we spent during my undergraduate degree.

The last and most important thanks go to my mother Amélia, my father Fernando, my sister Ana , my brother José and my grandparents José and Sara. They had and still have a very important role in my life. They motivate me to keep moving forward and in the hard times they have the gift to make me think "It could be worse" and make me laugh.

I finally acknowledge Laboratório de Instrumentação de Física Experimental de Partículas (LIP), the Portuguese ATLAS group and Fundação Calouste Gulbenkian for the significant support provided through the grants FEDER/COMPETE-QREN, FCT, Portugal (ref. IF/00050/2013/CP1172/CT0002) and Programa de Estimulo à Investigação.

Resumo

Esta dissertação teve como objetivo estudar a produção de eventos tZ através de Mudanças de Sabor por Correntes Neutras no LHC (Large Hadron Collider) que se encontra localizado no CERN. Os processos de mudança de sabor por correntes neutras são bastante raros no contexto do Modelo Padrão, uma vez que são ausentes a *tree-level* e altamente suprimidos a *loop-level.* Contudo, em modelos de Nova Física estes processos são bastante mais prováveis de ocorrer e possivelmente o LHC será sensível aos mesmos, tornando-se uma evidência que existe Física para além do Modelo Padrão se detectarmos estes processos no LHC. Neste trabalho é apresentado um lagrangeano que descreve todos os processos de mudança de sabor por correntes neutras, assim como a sua implementação no formato UFO que é passível de ser utilizado por um gerador de eventos de Monte Carlo. De seguida fazemos um estudo de como é que os parâmetros deste lagrangeano influenciam a cinemática dos processos tγ, tH e tZ. Em particular, no caso de tZ estudamos a cinemática tanto a nível partónico como a nível de simulação de detetor. Efetuamos ainda uma análise multivariacional usando *Boosted Decision Trees* (BDTs) de forma a estabelecer possíveis limites do LHC aos acoplamentos anómalos para uma energia de centro de massa de 13 TeV e uma luminosidade integrada de 10 fb^{-1}.

Abstract

The subject of this dissertation is the study of tZ event production by Flavour Changing Neutral Currents at the LHC (Large Hadron Collider) located in CERN. The Flavour Changing Neutral Currents processes are very rare in the Standard Model because they are not allowed at tree-level and highly suppressed at one loop-level. However in New Physics models they are much likely to occur and possibly the LHC will be sensible to these precesses, being a evidence that there is Physics Beyond the Standard Model if they are detected at the LHC. In this work we present a lagrangian that describes all the Flavour Changing Neutral Currents processes of the top quark. We also describe the implementation of this lagrangian in an appropriate format that can be used in Monte Carlo event generators. Then we study how the kinematics of the $t\gamma$,tH and tZ processes are influenced by the parameters of the lagrangian. In particular we study the kinematics of tZ both at parton and detector level. We also perform a multivariational analysis with *Boosted Decision Trees* (BDTs) to compute possible LHC limits on the anomalous couplings at a center of mass energy of 13 TeV and integrated luminosity of 10 fb^{-1}.

Contents

List of Figures

List of Tables

List of Abbreviations

ATLAS A Toroidal LHC ApparatuS

BDT Boosted Decision Tree

C.L. Confidence Level

CKM Cabibbo-Kobayashi-Maskawa

CMS Compact Muon Solenoid

CERN Conseil Européen pour la Recherche Nucléaire

EWSB Electroweak Symmetry Breaking

FCNC Flavour Changing Neutral Current

MVA Multivariate Analysis

NLO Next-to-Leading Order

LHC Large Hadron Collider

LO Leading Order

SM Standard Model

SPS Super Proton Synchrotron

PDF Parton Distribution Function

PS Proton Synchrotron

QCD Quantum Chromodynamics

TMVA Toolkit for Multivariate Analysis

UFO Universal FeynRules Output

Chapter 1

Introduction

The Standard Model of Particle Physics (SM) is the most successful about the nature of the subatomic world that mankind has achieved so far. This model describes the world around us as being composed of point particles that interact with each other by exchanging between other point particles. Among its major predictions are the existence of the W and Z bosons [1, 2, 3], the discovery of the top quark [4, 5] and more recently the confirmation of the existence of the Higgs boson [6, 7].

Despite its successes the Standard Model is thought not to be the most complete theory about particle physics because it cannot explain phenomena like the mass hierarchy, what is dark matter and dark energy or explain without fine tuning why the Higgs boson mass is low compared to the Planck scale [8, 9, 10]. To answer these questions several ideas that extend the Standard Model have been proposed. Among these ideas are supersymmetry, extra-dimensions, composite Higgs models or vector-like quarks [11, 12, 13, 14]. If this New Physics exists it predicts new symmetries, new particles and new interactions among the particles.

Among the SM particles the one that couples more strongly to this New Physics models is the top quark making the study of its properties a good place to search for the unknown. The top quark is also the most massive particle known to date with a mass of $173.34 \pm 0.27(stat) \pm 0.71(syst)$ GeV/c^2 [15], which is about the same mass as an atom of tungsten. The top has also an electric charge of +2/3 e and spin 1/2. The anti-particle of the top is the anti-top quark which has the same properties that the top has except opposite electric charge.

In the SM the top quark can decay through electroweak charged currents to b,s or d quarks. Due to unitarity of the CKM matrix the branching ratios $Br(t \to W^+s)$ and $Br(t \to W^+d)$ are close to zero but $Br(t \to W^+b)$ is very close to unity. The top quark decay through a neutral current , i.e. a top quark Flavour Changing Neutral Current (FCNC), is not possible at *tree-level* due to GIM mechanism [16]. However it is possible at *loop-level* but it is highly suppressed because of unitarity of CKM and due to the small values of the masses of other quarks with respect to the W boson.

In extensions of the SM it is possible to have FCNCs at *tree-level* or at *loop-level* due to additional interactions. Hence in New Physics scenarios top's FCNCs can have branching ratios several orders of magnitude higher then the ones predicted by the SM (see table 2.3 in section 2.5). In some cases the LHC can be sensible to the branching ratios predicted by New Physics models meaning that a detection of a top's FCNC is compelling evidence that there is physics beyond the SM because the branching ratios predicted by the SM are not high enough to this processes be detected at the LHC.

At hadron colliders top's FCNCs have been searched by CDF and D0 Collaborations at the Tevatron. Both CDF and D0 searched for the FCNC process $t \to Zq$ and obtained limits on the branching ratio $Br(t \to Zq)$ of 3.7 % and 3.2 %, respectively, at 95 % confidence level, where q is either an up or charm quark [17, 18] . At the LHC, CMS had also performed a search in this channel and had established that the branching ratio must be smaller than 6×10^{-4} at 95 % confidence level. ATLAS has also studied top's FCNCs but in the channel $t \to qg$ obtaining the limits 3.1×10^{-5} and 1.6×10^{-4} for $Br(t \to gu)$ and $Br(t \to gc)$ respectively at 95 % C.L. [20] . Searches for $t \to \gamma q$ have also been performed by the CMS experiment and for $t \to \gamma u$ and $t \to \gamma u$ we have as the limits of the corresponding branching ratios the values 0.0161 % and 0.182 % at 95 % C.L. respectively [21]. Concerning the Higgs channel ATLAS performed a search for top quark decays $t \to cH$ and established a limit for $Br(t \to cH)$ of 0.83 % at 95 % C.L. These experimental results point that the LHC is starting to be sensitive to some New Physics predictions about top quark FCNCs. We can also look for top FCNCs in e^+e^- collisions (as in LEP), through the processes $e^+e^- \to \gamma, Z^* \to t\bar{q}$ and its charge conjugate, or in $e^\pm p$ collisions (as in HERA) through the processes $e^\pm u \to e^\pm t$. LEP has upper limits at 95 % confidence level for $Br(t \to Zq) \leq 0.137$ and $Br(t \to \gamma q) \leq 0.041$ as well as upper limits for the anomalous couplings $|k_\gamma|$ and $|k_Z|$ around 0.4 [22, 23, 24, 25]. At HERA the H1 Collaboration has set $Br(t \to u\gamma) < 0.64\%$ at 95 % C.L. [26] while the ZEUS Collaboration has also set at 95 % C.L. $Br(t \to u\gamma) < 0.5\%$ and $Br(t \to uZ) < 30\%$ [27]. In figure 1.1 a summary of the branching ratios of the FCNCs of the top quark is presented.

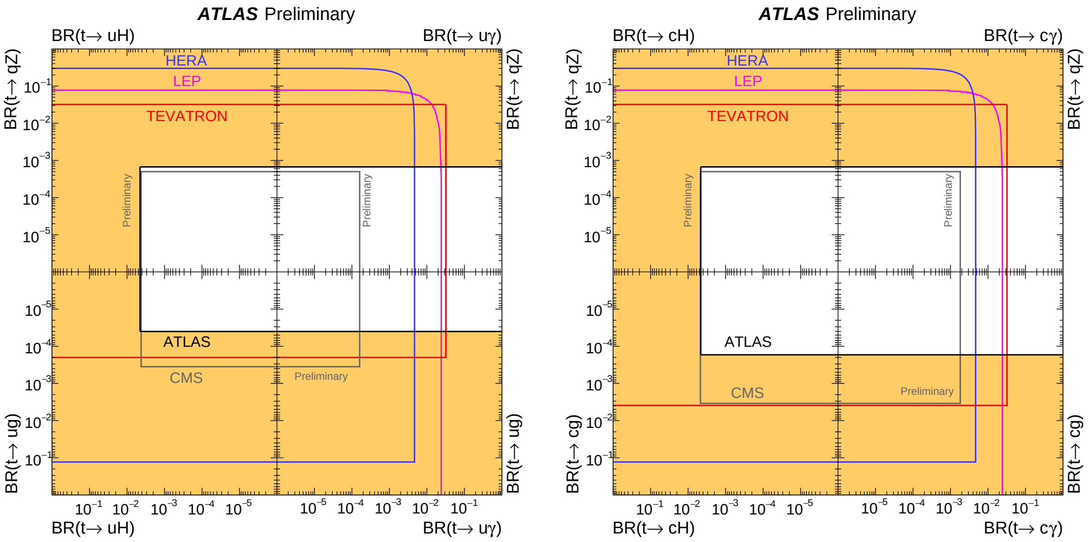

a) b)

Figure 1.1: Summary of the current 95 % confidence level observed limits on the branching ratios of the top quark decays via flavour changing neutral currents to a) an up quark and a neutral boson t->uX (X=g, Z, γ or H) or b) a up quark and a neutral boson t->cX (X=g, Z, γ or H). The coloured lines represent the results from HERA (the most stringent limits between the ones obtained by the H1 and ZEUS collaborations, in blue), LEP (combined ALEPH, DELPHI, L3 and OPAL collaborations result, in magenta), TEVATRON (the most stringent limits between the ones obtained by the CDF and D0 collaborations, in red) and the CMS Collaboration (in grey). The yellow area represents the region excluded by the ATLAS Collaboration. Extracted from [28].

Another way of studying the top FCNCs is by looking for its production with a neutral boson. These kind of studies allow to study more than one anomalous coupling at a time (see chapter 5). In this thesis we will study $t\gamma$, tH and tZ production through FCNCs with more emphasis in the former process. tZ can be produced by either an anomalous coupling with the gluon or with the Z. In the first case the Z boson is off-shell while in the latter an off-shell up or charm quark couples to on-shell top quark and on-shell Z boson. A search for tZ production at $\sqrt{s} = 13$ TeV at an integrated luminosity of 5 fb^{-1} was made by CMS and it established the branching ratios $Br(t \to gu) \leq 0.56\%$, $Br(t \to gc) \leq 7.12\%$, $Br(t \to Zu) \leq 0.51\%$ and $Br(t \to gu) \leq 11.40\%$ with the associated anomalous couplings limits $\frac{k_{gut}}{\Lambda} < 0.10$ TeV^{-1}, $\frac{k_{gut}}{\Lambda} < 0.35$ TeV^{-1}, $\frac{k_{Zut}}{\Lambda} < 0.45$ TeV^{-1} and $\frac{k_{gut}}{\Lambda} < 2.27$ TeV^{-1} respectively[19].

The first objective of this thesis is to study how the LHC will be sensible to tZ production at the Run II. To do that we will perform an analysis with simulated events at $\sqrt{s} = 13$ TeV and with a benchmark integrated luminosity of 10 fb^{-1} and derive limits to the anomalous couplings $\frac{k_{gut}}{\Lambda}$, $\frac{k_{gct}}{\Lambda}$, $\frac{k_{Zut}}{\Lambda}$ and $\frac{k_{Zct}}{\Lambda}$. In the tZ analysis of CMS they assumed that the anomalous couplings responsible for tZ production were all left-handed. In this thesis we will show how our results at 13 TeV change with the chirality of coupling. This thesis has also the objective of implementing in a UFO model a lagrangian that describes in a general way top FCNCs processes using dimension-six gauge invariant operators. The study of the dependence of kinematical observables on the anomalous couplings values of this lagrangian is performed.

Before we end this introduction let us review the content of each chapter: in Chapter 2 we review the Standard Model and present a lagrangian used to study top FCNC processes; since this thesis performs a sensibility study of the LHC to tZ processes in chapter 3 we perform a review of the LHC and of the ATLAS and CMS detectors; in chapter 4 a brief description of steps necessary to perform an appropriate Monte Carlo simulation of events as well as the implementation of the lagrangian in an UFO model is presented; chapter 5 describes the analysis used to study the properties of different FCNCs processes, in particular the tZ production; in chapter 6 we describe a multivariate analysis used for the study of the LHC sensibility to tZ production; and in chapter 7 we present the limits expected on the anomalous couplings of tZ in the Run II of the LHC at $\sqrt{s} = 13$ TeV with an integrated luminosity of 10 fb^{-1}.

Chapter 2

Theoretical Background

In this chapter we start with a quick review about the Standard Model of Particle Physics. The objectives of this review are to deduce relations that will be useful to write a lagragian characterising all the top FCNCs interactions and to explain qualitatively why these processes have very small probability amplitudes in the Standard Model. We end this chapter presenting how we deduced a lagrangian that describes top's FCNCs in the context of an Effective Theory using dimensions-six gauge invariant operators.

2.1 The Standard Model and Gauge symmetry

In the Standard Model (SM) every piece of matter in the universe is made up of particles. These particles interact through each other by exchanging particles between them. The particles of the Standard Model are divided in fermions and bosons. The fermions (spin 1/2) are also divided in quarks and leptons. There are six quarks and six leptons. There are also three families of quarks and three families of leptons. There is the family of the up (u) and down (d) quarks, the family of the charm (c) an strange (s) quarks and the family of the top (t) and bottom (b) quarks. In the lepton sector we have the family of the electron (e^-) and the electron neutrino (ν_e); the family of the muon (μ^-) and muon neutrino (ν_μ) and the family of tau (τ^-) and tau neutrino (ν_τ).

The Standard Model describes all the interactions in the universe except gravity. To each interaction there is an associated particle which is exchanged when particles interact through a given force. The photon (γ) is responsible to the electromagnetic force; the three vector bosons W^+,W^- and Z^0 are responsible for the weak nuclear force; and there are 8 gluons responsible for the strong nuclear force. All these particles are spin-1 particles.

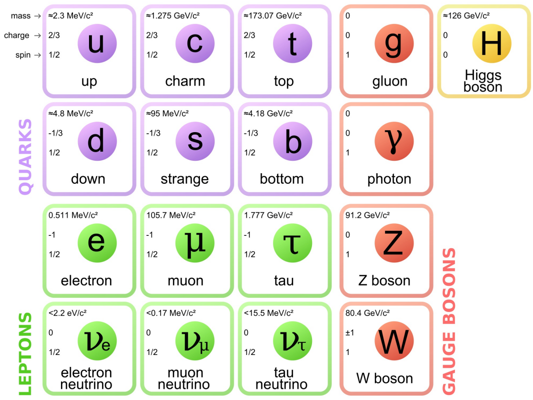

Figure 2.1: The Standard Model of Particle Physics.

Besides all these particles there is a key single ingredient to the Standard Model, the Higgs boson. This particle is responsible to give mass to all of the remaining particles. As we will see in the next sections, the principle of local gauge symmetry is the mathematical principle that governs particle interactions. But in order to have a theory invariant by such transformations it is necessary that all or some particles to be massless. However if we assume the existence of the Higgs boson it is possible to particles to have mass but also to preserve local gauge symmetry. The Standard Model is summed up in figure 2.1.

2.2 Quantum Electrodynamics

To illustrate how the principle of local gauge invariance allows us to derive how particles interact with each other let us consider the case of the gauge group U(1). As we will see demanding our theory to be local gauge invariance under U(1) transformations gives us Quantum Electrodynamics (QED).

Consider the Dirac Lagrangian that describes free spin 1/2 particles :

$$\mathcal{L}_{Dirac} = \text{ß}\bar{\psi}\gamma^{\mu}\partial_{\mu}\psi - m\bar{\psi}\psi \tag{2.1}$$

where ψ is the Dirac field, γ^μ represents Dirac's gamma matrices, m is the fermion mass and $\bar{\psi} = \gamma^0 \psi^\dagger$. This lagrangian is clearly invariant under a global U(1) gauge transformation :

$$\psi \rightarrow e^{iQ\theta}\psi \tag{2.2}$$

where Q is in units of the electric charge of the proton and θ is a real number. However if θ is a function of position and time i.e. a local gauge transformation the lagrangian transforms as

$$\mathcal{L} \rightarrow \mathcal{L} - Q\bar{\psi}\gamma^\mu \partial_\mu \theta \psi \tag{2.3}$$

In order to the lagrangian to be invariant under local gauge transformations we add the term $Q\bar{\psi}\gamma^\mu A_\mu \psi$ where A_μ is a vector field that transforms as

$$A_\mu \rightarrow A_\mu + \partial_\mu \theta \tag{2.4}$$

We are also interested in a dynamical gauge field A_μ so we must also include the term $-\frac{1}{4}F^{\mu\nu}F_{\mu\nu}$, where $F_{\mu\nu} = \partial_\mu A_\nu - \partial_\nu A_\mu$. With all these terms we finally obtain the QED lagrangian :

$$\mathcal{L}_{QED} = \text{ß}\bar{\psi}\gamma^\mu \partial_\mu \psi - m\bar{\psi}\psi - \frac{1}{4}F^{\mu\nu}F_{\mu\nu} + Q\bar{\psi}\gamma^\mu A_\mu \psi \tag{2.5}$$

By defining the covariant derivative as $D_\mu = \partial_\mu - \text{ß}QA_\mu$ we can rewrite the lagrangian as

$$\mathcal{L}_{QED} = \text{ß}\bar{\psi}\gamma^\mu D_\mu \psi - m\bar{\psi}\psi - \frac{1}{4}F^{\mu\nu}F_{\mu\nu} \tag{2.6}$$

Before ending this section it is important to note that the most general lagragian that describes a free vector field is the Proca Lagrangian

$$\mathcal{L} = -\frac{1}{4}F^{\mu\nu}F_{\mu\nu} + \frac{1}{2}m^2 A_\mu A^\mu \tag{2.7}$$

The corresponding gauge boson of the field has a mass m. However the mass term spoils local gauge-invariance in QED and we are forced to conclude that the local gauge invariance principle demands this gauge boson associated with the gauge field A_μ to be massless. This is the case for the photon. As we will see in the next sections this is not the case for the Weak interactions because as a short-range interaction it must be described by three massive gauge bosons. The subtle way to council the principle of local gauge invariance with massive vector gauge bosons in the Standard Model is through Spontaneous Symmetry Breaking and the existence of scalar field known as the Higgs Boson.

2.3 Quantum Chromodynamics - QCD

Quantum Chromodynamics is a non-abelian quantum field theory that describes the interactions between quarks and gluons which make up hadrons such as the proton and the neutron. In the Standard Model each quark has an internal degree of freedom known as colour which is analogous to the electric charge in Quantum Electrodynamics. Each quark can be in a Red, Green or Blue colour state and as in QED charged electrons interact through photon exchange, in QCD quarks interact with each other through gluon exchange. The gluon exchange changes the colour state of the interacting quarks. This implies that gluons are also colour carriers making it possible to gluons interact to each other.

Each quark flavour is in the fundamental representation of $SU(3)_{colour}$ and contains a triplet of fields [29, 30]. Each field is a Dirac spinor and is associated to a specific colour state. We denote this triplet by q and it can be represented as:

$$q = \begin{pmatrix} q_R \\ q_G \\ q_B \end{pmatrix} \tag{2.8}$$

The QCD lagrangian is derived by imposing a $SU(3)_{colour}$ local gauge invariance , i.e. the theory must be invariant by $q \rightarrow Uq$, where U is an element of $SU(3)_{colour}$. The lagrangian of this theory is

$$\mathcal{L}_{QCD} = \bar{q}(i\gamma^{\mu} D_{\mu} - m)q - \frac{1}{4} G^{a}_{\mu\nu} G^{\mu\nu}_{a} \tag{2.9}$$

with covariant derivative $D_{\mu} = \partial_{\mu} + i g_s \lambda_a G^{a}_{\mu}$ and strength field tensor

$$G^{a}_{\mu\nu} = \partial_{\mu} G^{a}_{\nu} - \partial_{\nu} G^{a}_{\mu} - g_s f_{abc} G^{b}_{\mu} G^{c}_{\nu} \tag{2.10}$$

where $\lambda_a, a = 1, 2, ...8$ are the Gell-Mann matrices, G^{a}_{μ} are the gluon fields, g_s is the QCD gauge coupling constant and f_{abc} are the structure constants of $SU(3)_{colour}$ [33].

QCD is unique relative to other interactions because of :

- Confinement, which means that if we separate quarks the energy of the gluon field will become high enough to create quark-anti-quark pairs, making it impossible to observe free quarks in the laboratory.

- Asymptotic freedom, which means that at very high energies quarks and gluons interact weakly with each other which allows the use of perturbation theory to compute observables. This phenomenon was theoretically discovered by Gross and Wilczek [31] and independently by Politzer [32].

2.4 Electroweak Interaction

The Electroweak interaction is responsible for the change of flavour of quarks and leptons. As the name suggests it is a theory in which electromagnetism and the weak nuclear force are unified in to a single interaction. This unification was done by Sheldon Lee Glashow, Abdus Salam and Steven Weinberg who were awarded a Physics Nobel Prize in 1979 for this work [34].

Each quark and lepton in the Standard Model has a left and right handed component. If ψ is a spinor associated with a quark or a lepton then its left and right component are respectively

$$\psi_L = \frac{1-\gamma^5}{2}\psi \qquad\qquad \psi_R = \frac{1+\gamma^5}{2}\psi \tag{2.11}$$

with adjoints

$$\bar{\psi}_L = \bar{\psi}\frac{1+\gamma^5}{2} \qquad\qquad \bar{\psi}_R = \bar{\psi}\frac{1-\gamma^5}{2} \tag{2.12}$$

where $\gamma^5 = i\gamma^0\gamma^1\gamma^2\gamma^3$ and $\bar{\psi} = \psi^\dagger\gamma^0$ with γ^μ ($\mu = 0, 1, 2, 3$) being the Dirac matrices. These matrices with a metric signature $(+, -, -, -)$ satisfy the anti-commutation relation $\{\gamma^\mu, \gamma^\nu\} = 2\eta^{\mu\nu} I_4$ where I_4 is the 4×4 identity matrix. In the Dirac representation these matrices are written as

$$\gamma^0 = \begin{pmatrix} 1 & 0 & 0 & 0 \\ 0 & 1 & 0 & 0 \\ 0 & 0 & -1 & 0 \\ 0 & 0 & 0 & -1 \end{pmatrix} \qquad \gamma^1 = \begin{pmatrix} 0 & 0 & 0 & 1 \\ 0 & 0 & 1 & 0 \\ 0 & -1 & 0 & 0 \\ -1 & 0 & 0 & 0 \end{pmatrix}$$

$$\gamma^2 = \begin{pmatrix} 0 & 0 & 0 & -i \\ 0 & 0 & i & 0 \\ 0 & i & 0 & 0 \\ -i & 0 & 0 & 0 \end{pmatrix} \qquad \gamma^3 = \begin{pmatrix} 0 & 0 & 1 & 0 \\ 0 & 0 & 0 & -1 \\ -1 & 0 & 0 & 0 \\ 0 & 1 & 0 & 0 \end{pmatrix} \tag{2.13}$$

and γ^5 as

$$\gamma^5 = \begin{pmatrix} 0 & 0 & 1 & 0 \\ 0 & 0 & 0 & 1 \\ 1 & 0 & 0 & 0 \\ 0 & 1 & 0 & 0 \end{pmatrix} \tag{2.14}$$

In several experiments it was found that weak interactions violate the parity symmetry. This means that the weak interactions only couples left-handed quarks and leptons. Mathematically the electroweak theory is a $SU(2)_L \times U(1)_Y$ non-abelian quantum field theory (the subscript reminds us that only left-handed states are involved). In this context the left-handed and right-handed components of quarks and leptons weak eigenstates (which can be linear combinations of flavour/mass eigenstates) are grouped in doublets and singlets of $SU(2)_L$ respectively. The members of a given doublet or singlet have the same weak hypercharge Y. Members from doublets have also a weak isospin quantum number I_3 that can take the values 1/2 and -1/2. These quantum numbers are related to the electric charge Q by the relation $Q = T_3 + Y$. There are three quark doublets, three lepton doublets , six quark singlets and six lepton singlets.

For quarks we denote these doublets and singlets by

$$q_{Li} = \begin{pmatrix} u_{Li} \\ d_{Li} \end{pmatrix}, \qquad u_{Ri}, \qquad d_{Ri} \qquad (i = 1, 2, 3) \tag{2.15}$$

with $(u_1, u_2, u_3 = (u, c, t)$ and $(d_1, d_2, d_3 = (d, s, b)$. For leptons doublets and singlets we have a similar notation :

$$l_{Li} = \begin{pmatrix} \nu_{Li} \\ e_{Li} \end{pmatrix}, \qquad \nu_{Ri}, \qquad e_{Ri} \qquad (i = 1, 2, 3) \tag{2.16}$$

with $(\nu_1, \nu_2, \nu_3 = (\nu_e, \nu_\mu, \nu_\tau)$ and $(e_1, e_2, e_3 = (e, \mu, \tau)$.

	T_3	Q	Y
ν_{Li}	1/2	0	-1/2
e^-_{Li}	-1/2	-1	-1/2
ν_{Ri}	0	0	0
e^-_{Ri}	0	-1	-1

Table 2.1: Weak quantum numbers of leptons.

	T_3	Q	Y
u_{Li}	1/2	2/3	1/6
d_{Li}	-1/2	-1/3	1/6
u_{Ri}	0	2/3	2/3
d_{Ri}	0	-1/3	-1/3

Table 2.2: Weak quantum numbers of quarks.

Before writing the electroweak lagrangian it is important to do two remarks. First, under a $SU(2)_L$ transformation the right-handed components of the fermionic fields are unchanged because they are singlets of $SU(2)_L$. Secondly, a lagrangian with local $SU(2)_L$ invariance can not have fermionic mass terms because

$$m\bar{\psi}\psi = m(\bar{\psi}_L + \bar{\psi}_R)(\psi_L + \psi_R) = m(\bar{\psi}_L\psi_R + \bar{\psi}_R\psi_L) \tag{2.17}$$

which is clearly invariant under a local U(1) symmetry, but not invariant under a local $SU(2)_L$ symmetry.

Then the lagrangian of this theory is

$$\mathcal{L}_{EW} = \mathcal{L}_{gauge} + \mathcal{L}_f \tag{2.18}$$

$$\mathcal{L}_{gauge} = -\frac{1}{4} W_a^{\mu\nu} W_{\mu\nu}^a - \frac{1}{4} B^{\mu\nu} B_{\mu\nu} \tag{2.19}$$

$$\mathcal{L}_f = \bar{q}_{Li} i\not{D} q_{Li} + \bar{u}_{Ri} i\not{D} u_{Ri} + \bar{d}_{Ri} i\not{D} d_{Ri} + \bar{l}_{Li} i\not{D} l_{Li} + \bar{e}_{Ri} i\not{D} e_{Ri} + \bar{\nu}_{Ri} i\not{D} \nu_{Ri} \tag{2.20}$$

The $\mathcal{L}_{gauge}$ term describes the interaction between the three W particles and the B particle since

$$W_{\mu\nu}^a = \partial_\mu W_\nu^a - \partial_\nu W_\mu^a - g_W \epsilon_{abc} W_\mu^b W_\nu^c \tag{2.21}$$

$$B_{\mu\nu} = \partial_\mu B_\nu^a - \partial_\nu B_\mu^a \tag{2.22}$$

with $a = 1, 2, 3$, g_W (g') is the $SU(2)_L$ ($U(1)_Y$) gauge coupling , ϵ_{abc} is the totally antisymmetric symbol and W_μ^a and B_μ are the gauge bosons of $SU(2)_L$ and $U(1)_Y$ respectively. The covariant derivative D_μ acting on the left-handed fields is

$$D_\mu = \partial_\mu + \frac{ig}{2} \tau_a W_\mu^a + ig' Y B_\mu \tag{2.23}$$

being τ^a the three Pauli matrices. The covariant derivative acting on the right-handed fields is the same as the one acting on the left-handed minus the term $\frac{ig}{2} \tau_a W_\mu^a$.

Although $\mathcal{L}_{EW}$ is the most general local $SU(2)_L \times U(1)_Y$ gauge invariant lagrangian it describes an unphysical theory because we know from experiment that both quarks and leptons are not massless and that there is only one massless gauge boson (the photon). The solution to these difficulties is known as Higgs Mechanism and was proposed by three independent groups in 1964 : by Brout and Englert [35]; by Higgs [36]; and by Guralnik, Hagen and Kibble [37].

The Higgs mechanism consists of a complex Higgs doublet in the spinor representation of $SU(2)_L$ with weak hypercharge 1/2 that after acquiring a non-zero vacuum expectation value spontaneously breaks the gauge symmetry i.e. the theory itself is gauge invariant but its ground state spoils the symmetry. In the remaining of this section we will first see how the existence of a Higgs boson changes the Electroweak lagrangian and secondly how gauge bosons acquire mass after spontaneous symmetry breaking.

The Higgs doublet can be written as

$$\phi = \begin{pmatrix} \frac{1}{\sqrt{2}}(\phi^1 + i\phi^2) \\ \frac{1}{\sqrt{2}}(\phi^3 + i\phi^4) \end{pmatrix} \tag{2.24}$$

where ϕ_i are hermitian fields. It is also assumed that associated to this field there is a potential $V(\phi) = -\frac{\mu^2}{2}\phi^\dagger\phi + \frac{\lambda}{4}(\phi^\dagger\phi)^2$ with $\mu^2 > 0$. The lagrangian describing this field is then

$$\mathcal{L}_\phi = D_\mu\phi^\dagger D^\mu\phi - V(\phi) \tag{2.25}$$

where D_μ is the covariant derivative of ϕ

$$D_\mu = \partial_\mu + ig_W\frac{\tau^a}{2}W_\mu^a + i\frac{g_Y}{2}B_\mu \tag{2.26}$$

Note that since ϕ has hypercharge 1/2 under $SU(2)_L$ it transforms as

$$\phi \to e^{i\alpha_i\frac{\tau^i}{2}}e^{i\frac{\beta}{2}}\phi \tag{2.27}$$

which means that L_ϕ is invariant under $SU(2)_L \times U(1)_Y$ but also that the most general lagrangian with couplings between the Higgs field and fermions is

$$\mathcal{L}_{Yukawa} = -Y_d^{ij}\bar{q}_{Li}\phi d_{Rj} - Y_u^{ij}\epsilon_{ab}\bar{q}_{Li}^a\phi^{\dagger b}u_{Rj} + H.c. \tag{2.28}$$

where Y_d^{ij} and Y_u^{ij} are general, not necessarily symmetric or Hermitian, complex-valued matrices. As can be seen in equation 17, the couplings of the Higgs with the other gauge bosons are present in the covariant derivative. The most general $SU(2)_L \times U(1)_Y$ gauge invariant lagragian with all Standard Model fermions plus a Higgs boson is

$$\mathcal{L} = \mathcal{L}_{gauge} + \mathcal{L}_{Yukawa} + \mathcal{L}_f + \mathcal{L}_\phi \tag{2.29}$$

$\mu^2 > 0$ in the potential of the Higgs field means that this potential has a minimum for which the vacuum expectation value is non-zero. A minimum for this potential occurs when

$$|\phi| = (\frac{\mu^2}{\lambda})^{1/2} = \frac{v}{\sqrt{2}} \tag{2.30}$$

Note that all the minimum for the potential are connected to each other through a

$SU(2)_L \times U(1)_Y$ transformation. If we assume that the field acquired the vacuum expectation value

$$< \phi >= \frac{1}{\sqrt{2}} \begin{pmatrix} 0 \\ v \end{pmatrix} \tag{2.31}$$

and consider the following expansion in the neighbourhood of this minimum

$$\phi = \frac{1}{\sqrt{2}} \begin{pmatrix} 0 \\ v + H(x) \end{pmatrix} \tag{2.32}$$

from $D_\mu \phi^\dagger D^\mu \phi$ (see the appendices for the computation of $D_\mu \phi$ we get the relevant term

$$\delta\mathcal{L} = \frac{1}{2}\frac{v^2}{4}[g_W^2 (W_\mu^1)^2 + g_W (W_\mu^2)^2 + (-g_W W_\mu^3 + g_Y B_\mu)^2] \tag{2.33}$$

There are three massive vector bosons, which we will notate as follows :

$$W_\mu^\pm = \frac{1}{\sqrt{2}}(W_\mu^1 \mp i W_\mu^2) \qquad \text{with mass} \qquad m_W = g\frac{v}{2}; \tag{2.34}$$

$$Z_\mu^0 = \frac{1}{\sqrt{g_W^2 + g_Y^2}}(g_W W_\mu^3 - g_Y B_\mu) \qquad \text{with mass} \qquad m_Z = \sqrt{g_W^2 + g_Y^2}\frac{v}{2}. \tag{2.35}$$

The fourth vector field, orthogonal to Z_μ^0, remains massless :

$$A_\mu = \frac{1}{\sqrt{g_W^2 + g_Y^2}}(g_Y W_\mu^3 + g_W B_\mu) \qquad \text{with mass} \qquad m_A = 0. \tag{2.36}$$

Now we can write the covariant derivate that acts in the fermionic fields in terms of these mass eigenstates as

$$\begin{aligned} D_\mu = \partial_\mu - i\frac{g_W}{\sqrt{2}}(W_\mu^+ T^+ + W_\mu^- T^-) - i\frac{1}{\sqrt{g_W^2 + g_Y^2}} Z_\mu (g_W^2 T^3 - g_Y^2 Y) \\ -i\frac{g_W g_Y}{\sqrt{g_W^2 + g_Y^2}} A_\mu (T^3 + Y) \end{aligned} \tag{2.37}$$

where

$$T^\pm = \frac{1}{2}(\sigma^1 \pm \sigma^2) \tag{2.38}$$

We can start to write the covariant derivative in a more useful and familiar way by defining the electron charge e as

$$e = \frac{g_W g_Y}{\sqrt{g_W^2 + g_Y^2}} \tag{2.39}$$

and remembering the relationship $Q = T^3 + Y$. We also define the weak mixing angle θ_W as $tan\theta_W = g_Y/g_W$ which allows us to write

$$cos\theta_W = \frac{g_W}{\sqrt{g_W^2 + g_Y^2}}, \qquad sin\theta_W = \frac{g_Y}{\sqrt{g_W^2 + g_Y^2}} \tag{2.40}$$

The Z_μ^0 and A_μ fields can then be written as

$$Z_\mu^0 = cos\theta_W W_\mu^3 - sin\theta_W B_\mu \tag{2.41}$$

$$A_\mu = sin\theta_W W_\mu^3 + cos\theta_W B_\mu \tag{2.42}$$

The covariant derivative acting in a fermionic field is then

$$D_\mu = \partial_\mu - i\frac{g_W}{\sqrt{2}}(W_\mu^+ T^+ + W_\mu^- T^-) - i\frac{g_W}{cos\theta_W} Z_\mu (T^3 - sin^2\theta_W Q) - iQeA_\mu \tag{2.43}$$

where

$$g_W = \frac{e}{sin\theta_W} \tag{2.44}$$

Let us focus on the quark sector. After Electroweak symmetry breaking $\mathcal{L}_{Yukawa}$ becomes

$$\begin{aligned} \mathcal{L}_{Yukawa} = & -\frac{Y_d^{ij} v}{\sqrt{2}}\bar{d}_{Li} d_{Ri} - \frac{Y_u^{ij} v}{\sqrt{2}}\bar{u}_{Li} d_{ui} - \\ & -\frac{Y_d^{ij} H}{\sqrt{2}}\bar{d}_{Li} d_{Ri} - \frac{Y_u^{ij} H}{\sqrt{2}}\bar{u}_{Li} u_{Ri} + H.c. + leptons \end{aligned} \tag{2.45}$$

To have mass terms we need that Y_d^{ij} and Y_u^{ij} to be diagonal matrices. Let

$$u'_{Li} = (u'_L, c'_L, t'_L), \qquad d'_{Li} = (d'_L, s'_L, b'_L) \tag{2.46}$$

be the quarks in the basis that diagonalizes the matrices Y_d^{ij} and Y_u^{ij}. Since with these quarks we have mass terms present in $\mathcal{L}_{Yukawa}$ they are the physical ones. These two basis are related by unitary transformations :

$$u_{Li} = U_u^{ij} u'_{Lj}, \qquad d_{Li} = U_d^{ij} d'_{Lj} \tag{2.47}$$

In this basis the matrices Y_d and Y_u are respectively

$$\begin{pmatrix} y_d & 0 & 0 \\ 0 & y_s & 0 \\ 0 & 0 & y_b \end{pmatrix}, \begin{pmatrix} y_u & 0 & 0 \\ 0 & y_c & 0 \\ 0 & 0 & y_t \end{pmatrix} \tag{2.48}$$

where the y_i is the Yukawa coupling of the quark i. In the Yukawa lagrangian $\mathcal{L}_{Yukawa}$ we will have mass terms related to the mass of the quark i as

$$m_i = \frac{y_i v}{\sqrt{2}} \tag{2.49}$$

With this change of basis, the form of the coupling between quarks and W boson is written as

$$-i\frac{g_W}{\sqrt{2}}\bar{u}_{Li}\gamma^\mu d_{Li} W_\mu^+ + H.c. = -i\frac{g_W}{\sqrt{2}}\bar{u'}_{Li}\gamma^\mu (U_u^\dagger U_d)_{ij} d'_{Lj} W_\mu^+ + H.c. \tag{2.50}$$

This expression can then be written as

$$-i\frac{g_W}{\sqrt{2}}\bar{u'}_{Li}\gamma^\mu V_{ij} d'_{Lj} W_\mu^+ + H.c. \tag{2.51}$$

where V_{ij} is a unitary matrix called the Cabibbo-Kobayashi-Maskawa (CKM) matrix. The non-zero off-diagonal terms in CKM matrix allows transitions between quarks of different generations. By performing a global fit to all available measurements and imposing three generation unitarity the CKM matrix according to [38] is

$$\begin{pmatrix} |V_{ud}| & |V_{us}| & |V_{ub}| \\ |V_{cd}| & |V_{cs}| & |V_{cb}| \\ |V_{td}| & |V_{ts}| & |V_{tb}| \end{pmatrix} = \begin{pmatrix} 0.97427 \pm 0.00014 & 0.22536 \pm 0.00061 & (3.55 \pm 0.15) \times 10^{-3} \\ 0.22522 \pm 0.00061 & 0.97343 \pm 0.00015 & (41.4 \pm 1.2) \times 10^{-3} \\ (8.86 \pm 0.33) \times 10^{-3} & (40.5 \pm 1.1) \times 10^{-3} & 0.99914 \pm 0.00005 \end{pmatrix} \tag{2.52}$$

2.5 top FCNCs in the Standard Model

As it was mentioned in the introduction a Flavour Changing Neutral Current is a process with a change in the flavour of a fermion without changing its electric charge. This change occurs with an emission of neutral gauge boson. By looking at equations 2.43 and 2.46 (after diagonalization) we see that there are not vertices contributing at tree level to these processes. However they are possible at one-loop level as shown by figure 3.

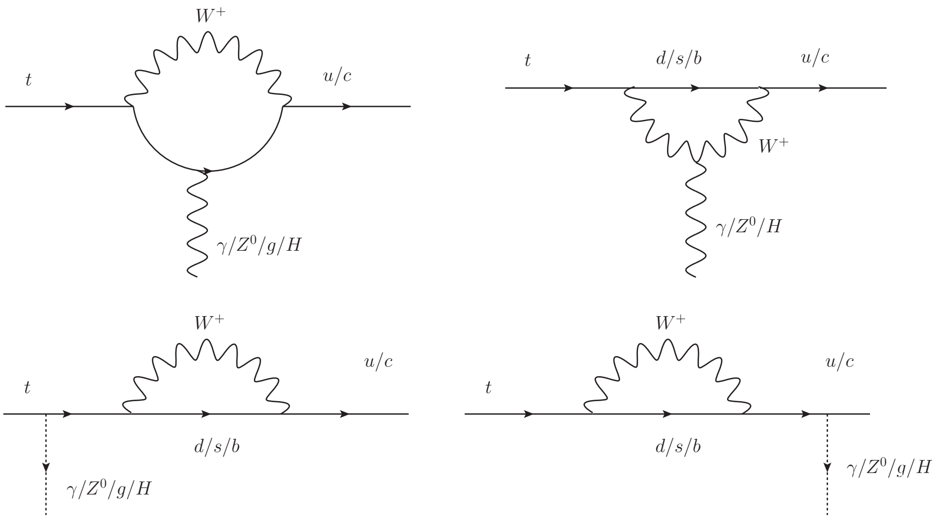

Figure 2.2: Feynman diagrams at one-loop level for top quark Flavour Changing Neutral Currents in the Standard Model.

As an example, for the case that the vector boson is the Z^0 the probability amplitude $\mathcal{M}$ is proportional to

$$F(m_d/m_W)V_{td}V_{qd}^* + F(m_s/m_W)V_{ts}V_{qs}^* + F(m_b/m_W)V_{tb}V_{qb}^* \tag{2.53}$$

with $q = u, c$ and the function $F(x)$ resulting from the loop integrals. These functions are known as Inami-Lim functions and for this case have the form [39, 40]

$$F(x) = \frac{x}{8}[\frac{x+2}{x-1} + \frac{3x-6}{(x-1)^2}\ln x] \tag{2.54}$$

Because $m_d \ll m_s \ll m_b \ll m_W$ the F's in equation 2.54 take a very small value. Moreover the CKM matrix elements V_{td},V_{ts} and V_{qb} are very-small in the Standard Model hence these processes are highly suppressed. Note also that unitarity of CKM implies

$$V_{id}V_{jd}^{*} + V_{is}V_{js}^{*} + V_{ib}V_{jb}^{*} = 0 \tag{2.55}$$

meaning that FCNCs would vanish if the masses of the down quarks were degenerate.

In models beyond the Standard Model it is possible to have FCNCs at tree-level or also new contributions at loop-level. In either case, several new physics models predict FCNCs with higher branching ratios by several orders of magnitude. A comparison between Standard Model predictions and New Physics models predictions are present in table 3.

Process	Standard Model	2HDM	MSSM	Extra-Dimentions
$t \to gc$	4.6×10^{-12}	$\sim 10^{-4}$	8.5×10^{-5}	$\sim 10^{-5}$
$t \to Zc$	1×10^{-14}	$\sim 10^{-7}$	2×10^{-6}	$10^{-11} - 10^{-5}$
$t \to \gamma c$	4.6×10^{-12}	~ 10ˆ-6	2×10^{-6}	$\sim 10^{-6}/1.08 \times 10^{-10}$
$t \to Hc$	3×10^{-15}	1.5×10^{-3}	10^{-5}	$10^{-11} - 10^{-5}$

Table 2.3: Branching ratios of top's FCNCs for the SM and New Physics models for the decay of the top to a charm quark and a neutral boson. Extracted from [41, 42, 43, 44].

2.6 top FCNCs Lagrangian

In general the experimental studies of top quarks FCNCs are performed in a model independent way. This demands a general theoretical description and parameterisation of New Physics contributions to top's FCNCs. This is done using an Effective Field Theory which allows us to describe New Physics effects at low energies while we neglect the structure of the underlying New Physics model. This can be done by writing our lagrangian as a power series expansion of $\frac{1}{\Lambda}$

$$\mathcal{L} = \mathcal{L}_{SM} + \frac{1}{\Lambda}\mathcal{L}^{(5)} + \frac{1}{\Lambda^2}\mathcal{L}^{(6)} + ... \tag{2.56}$$

where $\mathcal{L}_{SM}$ is the Standard Model lagrangian, $\mathcal{L}^{(5)}$ is a dimension-five gauge invariant operator and $\mathcal{L}^{(6)}$ is a dimension-six gauge invariant operator and Λ is the New Physics energy scale. In this work $\mathcal{L}^{(5)}$ is not considered because these operators violate total lepton number conservation [45, 46]. This assumption is not in contradiction with the discovery of neutrino oscillation [47, 48, 49, 50, 51, 52] because these processes in the

Standard Model conserve total lepton number, i.e. the sum of the lepton numbers of all lepton flavours.

With this considerations the most general dimension-six gauge invariant operator can be written as

$$\mathcal{L}^{(6)} = \sum_x C_x O_x \tag{2.57}$$

where C_x is a complex number and O_x a dimension-six gauge invariant operator. The operator expansion of equation 9 makes sense only if the set of operators O_x is a basis and if they are not redundant. Concerning anomalous couplings of the top quark this issue has been studied in [53, 54] where it is shown that the most relevant operators contributing to flavour changing neutral interactions of the top with the photon and Z boson , gluons and the Higgs are equations 10 , 11 and 12 respectively.

$$\begin{aligned}
O_{\phi q}^{(3,ij)} &= i(\phi^\dagger \tau^I D_\mu \phi)(\bar{q}_{Li}\gamma^\mu \tau^I q_{Lj}), \\
O_{\phi q}^{(1,ij)} &= i(\phi^\dagger D_\mu \phi)(\bar{q}_{Li}\gamma^\mu q_{Lj}), \\
O_{\phi u}^{ij} &= i(\phi^\dagger D_\mu \phi)(\bar{u}_{Ri}\gamma^\mu u_{Rj}), \\
O_{uW}^{ij} &= (\bar{q}_{Li}\sigma^{\mu\nu}\tau^I u_{Rj})\tilde{\phi} W_{\mu\nu}^I, \\
O_{uB\phi}^{ij} &= (\bar{q}_{Li}\sigma^{\mu\nu} u_{Rj})\tilde{\phi} B_{\mu\nu} && (2.58) \\
O_{uG\phi}^{ij} &= (\bar{q}_{Li}\lambda^a \sigma^{\mu\nu} u_{Rj})\tilde{\phi} G_{\mu\nu}^a, && (2.59) \\
O_{u\phi}^{ij} &= (\phi^\dagger \phi)(\bar{q}_{Li} u_{Rj} \tilde{\phi}) && (2.60)
\end{aligned}$$

Before we present the lagrangian that parameterises New Physics contributions to top's FCNCs let us present how we compute the Htc vertex as an example of how to obtain all the vertices of the lagrangian. According to [54] the relevant operators for an effective Htc interaction are the operators $O_{u\phi}^{32}$ and $O_{u\phi}^{23}$:

$$\begin{aligned}
O_{u\phi}^{32} &= (\phi^\dagger \phi)(\bar{q}_{L3} u_{R2} \tilde{\phi}) \\
O_{u\phi}^{23} &= (\phi^\dagger \phi)(\bar{q}_{L2} u_{R3} \tilde{\phi})
\end{aligned} \tag{2.61}$$

After Electroweak $\phi = \begin{pmatrix} 0 \\ \frac{v+H}{\sqrt{2}} \end{pmatrix}$ and $\tilde{\phi} = i\tau^2\phi$. Since $\bar{q}_{L3} = (\bar{t}_L, \bar{b}_L)$, $u_{R2} = c_R$ and

$u_{R3} = t_R$ we can write these operators as

$$O^{32}_{u\phi} = \frac{(v+H)^3}{2\sqrt{2}}\bar{t}P_R c$$
$$O^{23}_{u\phi} = \frac{(v+H)^3}{2\sqrt{2}}\bar{c}P_R t$$

In the expansion of $(v+H)^3$ the only relevant term is $3v^2H$ and then we can finally write a lagrangian for a Htc interaction

$$\mathcal{L}_{Htc} = \frac{C^{32}_{u\phi}}{\Lambda^2}\frac{3v^2}{2\sqrt{2}}\bar{t}P_R cH + \frac{C^{23}_{u\phi}}{\Lambda^2}\frac{3v^2}{2\sqrt{2}}\bar{c}P_R tH + H.c. \tag{2.62}$$

Since the Hermitian conjugate of $\bar{t}P_R c$ is $\bar{c}P_L t$ and defining

$$\eta^L_{ct} = -\frac{3}{2}C^{32*}_{u\phi}\frac{v^2}{\Lambda^2}$$
$$\eta^R_{ct} = -\frac{3}{2}C^{23}_{u\phi}\frac{v^2}{\Lambda^2}$$

we finally arrive at the Lagrangian describing a Htc interaction

$$\mathcal{L}_{Htc} = -\frac{1}{\sqrt{2}}\bar{c}(\eta^L_{ct}P^L + \eta^R_{ct}P^R)tH + H.c. \tag{2.63}$$

We note that the corresponding lagrangian for a Htu interaction is derived in the same way by making $2 \to 1$ in equations 13. The derivations of the lagrangians $\mathcal{L}_{gtq}$, $\mathcal{L}_{Ztq}$ and $\mathcal{L}_{\gamma tq}$ with $q = u, c$ are lengthier and for this reason are present in the appendices A and B.

After all these computations we arrive to the lagrangian that parametrizes the New Physics contributions to the the FCNCs of the top quark

$$\begin{aligned}\mathcal{L}_{topFCNC} = \sum_{q=u,c}\frac{g_s}{2m_t}\bar{q}\lambda^a\sigma^{\mu\nu}(\zeta^L_{qt}P^L + \zeta^R_{qt}P^R)tG^a_{\mu\nu} - \frac{1}{\sqrt{2}}\bar{q}(\eta^L_{qt}P^L + \eta^R_{qt}P^R)tH - \\ -\frac{g_W}{2c_W}\bar{q}\gamma^\mu(X^L_{qt}P_L + X^R_{qt}P_R)tZ_\mu + \frac{g_W}{4c_W m_Z}\bar{q}\sigma^{\mu\nu}(K^L_{qt}P_L + K^R_{qt}P_R)tZ_{\mu\nu} + \\ + \frac{e}{2m_t}\bar{q}\sigma^{\mu\nu}(\lambda^L_{qt}P_L + \lambda^R_{qt}P_R)tA_{\mu\nu} + H.c.\end{aligned} \tag{2.64}$$

From now on couplings with a superscript L are called left-handed couplings while couplings with a superscript R are called right-handed couplings. Before we end this section we just recall that in the Standard Model all the anomalous couplings are zero because FCNCs are not allowed at tree-level as we saw in the previous section. In chapter 4 we show how we implemented $\mathcal{L}_{topFCNC}$ in an UFO model to be used for event generation.

Chapter 3

Experimental Apparatus

In this section we give a brief description about the European Organisation for Nuclear Research, also known as CERN, the Large Hadron Collider (LHC) and the ATLAS [55] and CMS [56] detectors.

3.1 CERN

At the end of the World War 2 the European science faced two major problems: costs in fundamental science started to be so huge that it would be hard for a single state to support them and European science was no longer world-class due to the migration of the best minds to the United States of America due to the Nazi regime. In an effort to solve these issues a group of physicists proposed the formation of a nuclear physics laboratory. In 1952 a provisional council named Conseil Européen pour la Recherche Nucléaire (CERN) was formed to establish such laboratory. The formation of this council was signed by eleven countries and the acronym CERN was born. This council decided that CERN would be built at Geneva, Switzerland.

Since its beginning CERN was behind of some of the the most important discoveries in particle physics. Among them are the discovery of the W and Z in the UA1 and UA2 experiments [1, 2, 3] , the determination of the number of light neutrinos families at LEP [57] , the discovery of direct CP violation in the NA48 experiment [58] and more recently the discovery of a boson consistent with the properties of the Standard Model Higgs Boson [6, 7]. CERN was also responsible for technological developments, being the creation of the World Wide Web as we know it today by Tim Berners-Lee

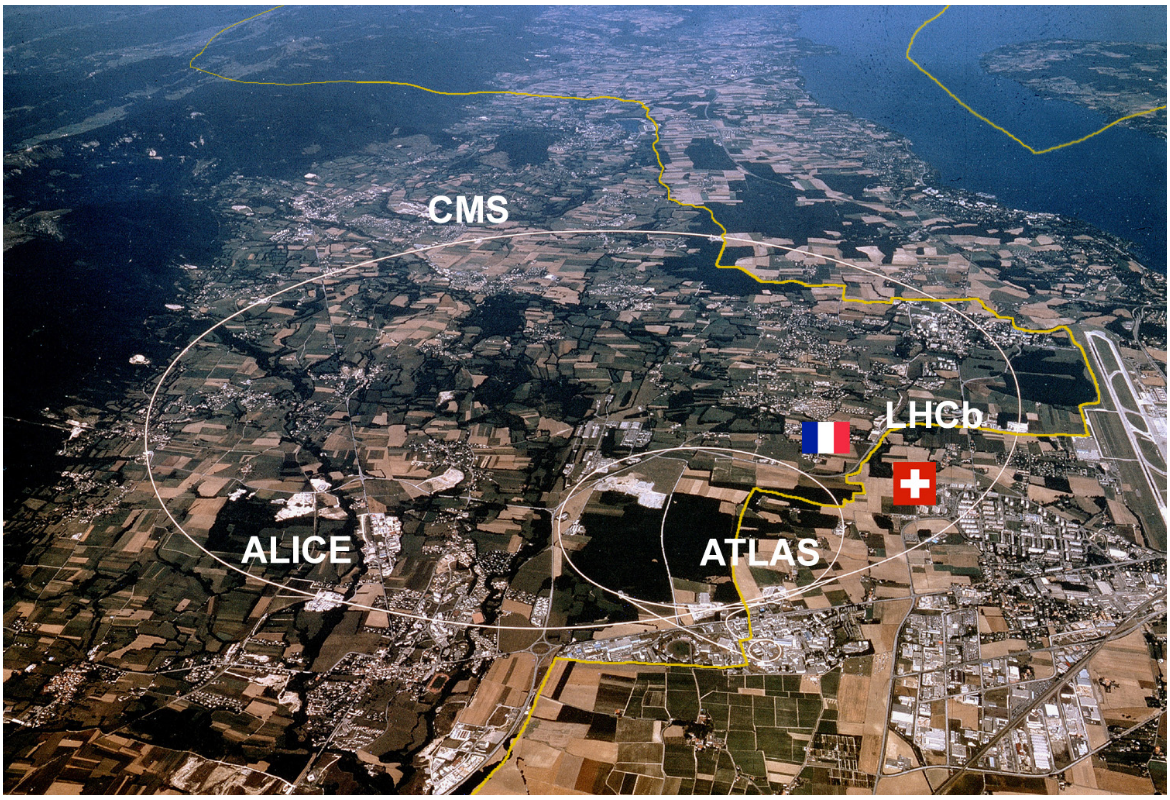

Figure 3.1: Aerial view of the LHC. The yellow line is the border between France and Switzerland. To have an idea of how big is the LHC note that on the right is the Geneva airport and the Geneva Lake. Figure extracted from [60]

the most famous example, and more recently it became a facility for the development of grid computing.

3.2 Large Hadron Collider

The Large Hadron Collider (LHC) [59] is the largest and most powerful particle accelerator ever built. It is a circular accelerator with a perimeter of 27 Km that is located inside a tunnel 100 m below the floor that crosses the border between Switzerland and France.

The LHC accelerates protons in opposite directions to speeds close to the speed of light. The protons come from ionization of hydrogen and accelerated in different stages. First they are accelerated at the linear accelerator LINAC where they reach an energy of 50 MeV. After that they are accelerated again in the Proton Synchrotron Booster (PSB) where they reach an energy of 1 GeV. Then in the Proton Synchrotron (PS) they reach an energy of 25 GeV. Then they are injected and accelerated in the

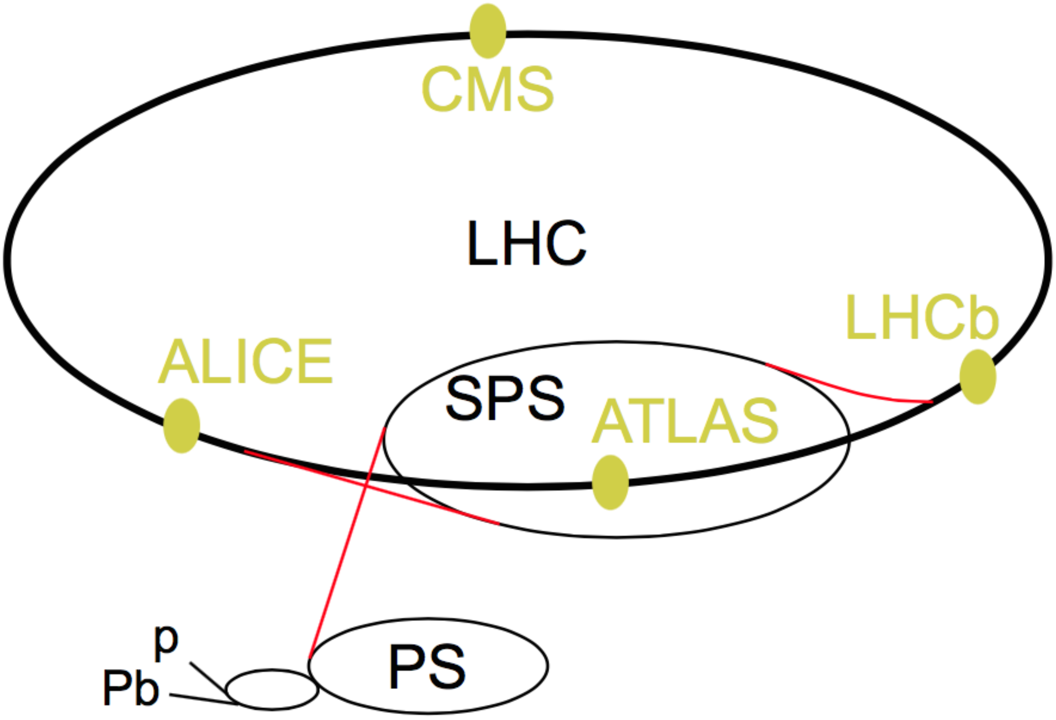

Figure 3.2: Scheme of the LHC experiments ATLAS, ALICE, CMS and LHCb; and preaccelerators PS (Proton Synchrotron) and SPS (Super Proton Synchrotron); figure extracted from [61].

Super Proton Synchroton (SPS) until they have an energy of 450 GeV. Finally they are injected in the LHC in bunches, each bunch having around 10^{11} protons. Some bunches travel clockwise and other anti-clockwise. The energy that they reach in the first period of operation of the LHC was first of 3.5 TeV (3500 GeV) per beam between 2010 and 2012. In 2012 it started to operate at 4 TeV per beam until its first shutdown in 2013. Recently, in May 2015 the LHC started to accelerate beams up to an energy of 6.5 TeV but it may reach 7 TeV depending on magnet training. In this second stage of operation, run 2, the LHC will also have higher luminosities. In run 1 it reached a luminosity around $6 \times 10^{33} cm^{-2} s^{-1}$ and it is thought that in run 2 it may peak somewhere between $1.5 - 2.0 \times 10^{34} cm^{-2} s^{-1}$.

The beams travel in separated pipe-tubes kept at ultrahigh vacuum. Since the protons are charged particles strong magnetic fields are necessary to curve protons around the circular accelerator. This is done employing 1232 dipole magnets made niobium-titanium cables that are maintained at a temperature of 1.9 K (-271.3 °C) which is inferior than the temperature of outer space (2.7 K or -270.5 °C). At this temperature this dipole magnets are superconducting and generate a magnetic field of 8 T. 392

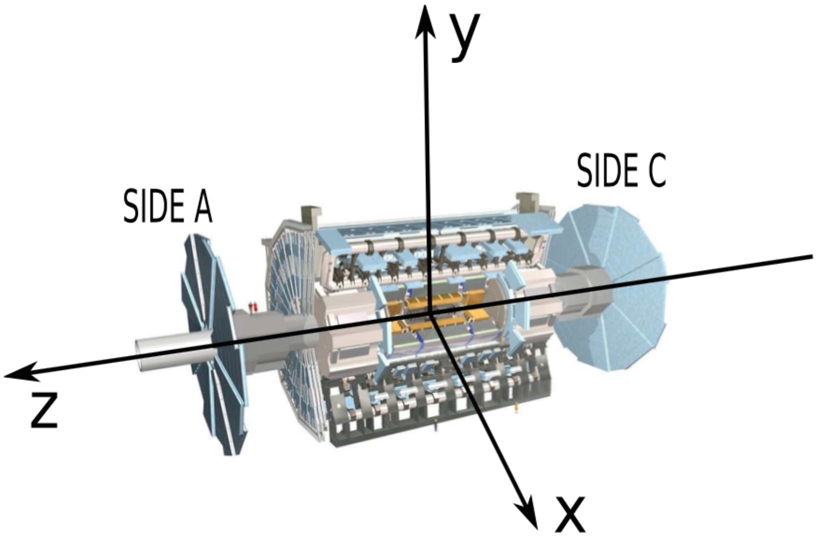

Figure 3.3: ATLAS coordinate system: the side-A of the detector is defined as the one with positive z and side-C as that with negative z. The azimuthal angle ϕ is measured around the beam axis, and the polar angle θ is measured from the beam axis. Figure extracted from [61]

quadrupole magnets are used in order to maintain the beams focused. RF cavities delivering 2 MV at 400 MHZ operating at 4.5 K are responsible for accelerating protons as well keeping their energy constant (there are losses mainly due to Synchrotron Radiation).

When the beams have the energy necessary they are collided in four main distinct points where there a particle detector at each point. They are the ALICE, ATLAS, CMS and LHCb detectors. In this work we will only focus in the ATLAS and CMS detectors.

3.3 ATLAS Detector

ATLAS is the acronym for **A** **T**oroidal **L**HC **A**pparatu**S** and is the largest detector at the LHC as well the one with the greatest collaboration which has more than 3000 people. New Physics at the LHC can manifest itself in a variety of processes demanding ATLAS to be a general-purpose detector rather than a detector designed to search for a specific process. In order to achieve this ATLAS is composed of ever-larger concentric cylinders around the interaction point. These layers are divided in four components: an inner detector, an electromagnetic calorimeter, a hadronic calorimeter, a muon spectrometer and a magnet system consisting of central solenoid and a toroidal structure.

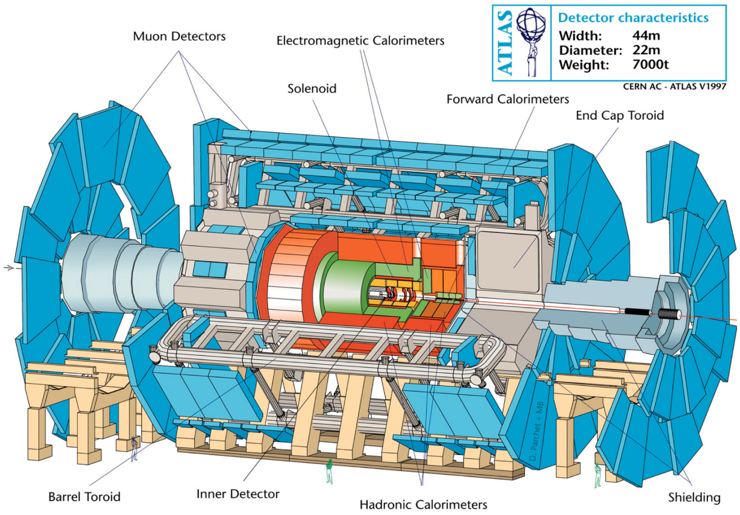

Figure 3.4: Cut view of the ATLAS detector. It has a width of 44 m, a diameter of 22 m and a weight of 7000 tonnes. Coloured people are present in order to visualize the size of ATLAS. Next to the beam line (the red line in the figure) we have the inner detector. At green we have the Electromagnetic Calorimeter (ECAL), at red we have the Hadronic Calorimeter (HCAL) and blue we have the Muon Detectors. Figure extracted from [62]

Before we do a review of each detector we introduce its coordinate system. The origin of the coordinate system is defined as the interaction point. The z axis is along the beam line and the x-y axis is perpendicular to the beam line. For this reason it is known as the transverse plane. The momentum measured of the detected particles in the transverse plane is known as transverse momentum and it is denoted by p_T. The positive x-axis points from the interaction point to the center of the LHC and the positive y-axis points upward to the surface of earth. With respect to the coordinate system the detector is divided in two sides. An "A-side" which is where z-values are positive and a "C-side" where z values take negative values. The azimuthal angle ϕ is measured relative to the x-axis around the beam line. The polar angle θ is defined as the angle from the positive z-axis. This angle is related to quantity known as pseudo-rapidity by the formula $\eta = -\ln\tan(\theta/2)$. In the $\phi - \eta$ space it is defined the distance ΔR as $\Delta R = \sqrt{\Delta\eta^2 + \Delta\phi^2}$.

The inner detector is responsible for measuring particle momentum and its electric charge. It begins a few centimetres from the proton beam axis, extends to a radius of 1.2 metres, and is 6.2 metres in length along the beam pipe. The inner detector is immersed in a 2T magnetic field generated by the central solenoid and provides charged-particle tracking in the range $|\eta| < 2.5$. In order to achieve very good granularity and momentum resolution, pixel and silicon microstrip trackers are used in combination with straw tube of the transition radiation tracker.

The calorimeter closest to the beam is the electromagnetic calorimeter (EMC). It is divided in to a barell and two end-caps regions. As a sampling calorimeter it has an absorver material which is lead while the active medium is liquefied Argon (LAr). The active medium is between two layers of lead. The accordion geometry provides complete ϕ symmetry without azimuthal cracks. Next to the EMC we have the hadronic calorimeter which uses either scintillator tiles or liquified Argon as active mediums and the absorver materials are steel, copper and tungsten. Like the EMC it is composed of three subdetectors: the tile calorimeter (TileCal) and two liquified Argon hadronic end-caps. The entire calorimeter system covers the pseudo-rapidity range $|\eta| < 4.9$. Surrounding these two calorimeters we have the muon spectrometer. It measures the deflection of muons with $|\eta| < 2.7$ using multiple layers of high-precision tracking chambers located in a magnetic field of 0.5 T or 1 T. These fields are generated respectively by the barrel toroid and two end-cap toroids which make up the toroidal structure of ATLAS. The muon spectrometer is also instrumented with separate trigger-chambers covering $|\eta| < 2.4$. In table 4 we find a summary of the sensivity to energy and p_T measurements of the ATLAS detector. Table 5 summarizes the pseudorapidity coverage, granularity and segmentation in layers for each calorimeter.

There is also a three-level trigger system to reduce the amount of raw date. The level-1 trigger is implemented in hardware and uses a subset of detector information to reduce the event rate to a design value of at most 75 kHz. This is followed by two software-based trigger levels, level-2 and the event filter, which exploit full detector information and reduced the event rate to about 400 Hz during 2012.

3.4 CMS Detector

CMS is acronym for **C**ompact **M**uon **S**olenoid and like ATLAS it is a multipurpose detector. The coordinate-axis definition of CMS is also the same as ATLAS. CMS is also formed of different layers : a tracker, an electromagnetic calorimeter, a hadronic calorimeter, a magnet and a muon detector.

The main feature of this detector is the superconducting solenoid with 6m in diameter that generates a strong magnetic field of 3.8 T. Inside this solenoid the tracker and calorimeters are compact enough to fit inside. Outside of the magnet are large muon detectors which are inside the return yoke of the magnet.

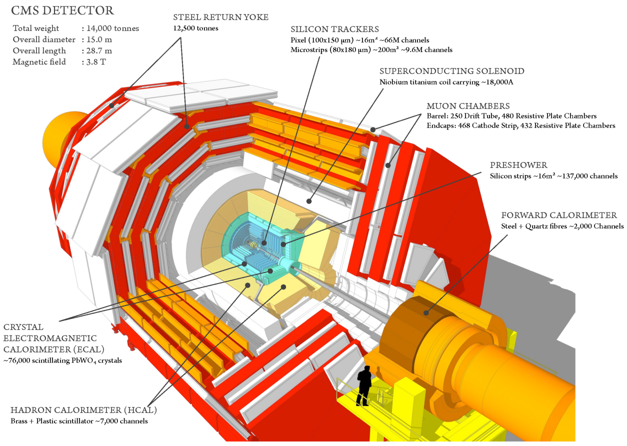

Figure 3.5: Cut view of the CMS detector. It has a length of 28.7 m and a diameter of 15.0 m weighting 14000 tonnes. The black person is placed in the figure to visualize the dimension of the CMS detector. Next to the beam pipe (grey in the figure) we have the Silicon Trackers; at light blue we have the Crystal Electromagnetic Calorimeter (ECAL); next to the ECAL with a light yellow colour we have the Hadronic calorimeter (HCAL). The white plates between the red Steel Return Yoke are the Muon Chambers.

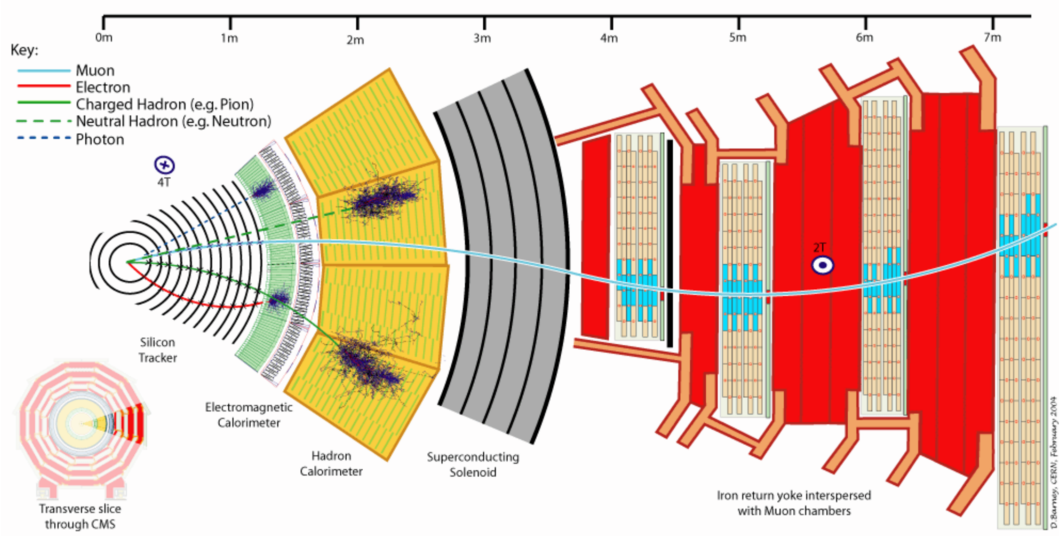

Figure 3.6: Sliced transversal representation of the CMS detector. Here we can see the trajectories of the different types of particles that are detected by the CMS detector. A charged particle that is bend in the Silicon Tracker and stopped in the ECAL is an electron candidate (red line) while a neutral one that is stopped in the ECAL is a photon candidate (dashed blue line). A charged hadron (green line) is a particle whose trajectory is bend and is stopped at the HCAL and a neutron hadron (dashed green line) is a particle that has a straight line trajectory in the tracker that is stopped by the HCAL. Finally the muons (wavy light blue line) cross all the detector. Extracted from [64]

The tracking system is the innermost part of the CMS detector. Its purpose is to measure with precision the momentum and charge of charged particles produced in the proton collisions and bent by the magnetic field produced by the solenoid. To achieve high granularity so that it identifies properly particle tracks silicon detectors are used. These detectors add up to a length of 5.8 m and a diameter of 2.5 m, covering a region of $|\eta| < 2.5$.

The Electromagnetic calorimeter used in the CMS experiment is a homogeneous one. It is installed around the inner tracking system so that it covers a region of $|\eta| < 3.0$. It is made of lead tungstane ($PbWO_4$) crystals and is divided in three subdetectors : the Barrel Electromagnetic Calorimeter, two Endcap Electromagnetic Calorimeter both at the front and back and the Preshower. The Preshower is placed in the front of the end-cap crystals and granularity such that it offers the possibility to identify neutral pions decaying into two collimated photons. The hadronic calorimeter completely surrounds both the tracking system and the electromagnetic calorimeter while is mainly inside the magnet. The objective of this device is to measure with accuracy both the energy of hadronic jets and invisible particles by determination of missing transverse energy. To do this this detector covers a pseudo-rapidity up to $|\eta| = 5.2$ so that it covers almost all the particles generated in an interaction. This calorimeter is formed by four sub-detectors : the Hadron barrel, the Hadron outer, the Hadron end-cap and the Hadron forward. The Hadron outer is necessary because the Hadron barrel dimensions are limited by the outermost circumference of the barrel electromagnetic calorimeter and the innermost border of the solenoid. The muon system is outside of the magnet solenoid. The entire system covers the region $|\eta| < 2.4$ and is formed by three subdetectors : Drift Tube (DT) chambers, Cathod Strip Chambers (CSC) and Resistive Plate Chambers (RPC). Each chamber is composed of a positively charged wire or plate in a volume filled with gas. The DTs are used for precise trajectory measurements in the central barrel region, while the CSCs are used in the end caps. The RPCs are installed both in the barrel and end caps and provide a fast signal when a muon passes thorough the muon detector.

CMS has also a trigger system to reduce the rate of interesting events. All the data from each crossing is buffered within the detector while a small amount is used to look for special properties of the particles detected (e.g. p_T). This is known as the Level 1 trigger and is performed using field-programmable gate arrays (FPGA). It selects about 100 000 events each second from the billion available. When an event passes the Level 1 trigger, all the data is sent over fibre-optic links to the "High Level" trigger, which is software running on ordinary computer servers. Since the rate of information arriving at this higher level is smaller these CPUs can run more complex physics tests like matching tracks to hits in the muon chamber or spotting photons due to their high energy deposit in the electromagnetic calorimeter but lack of electric charge.

We would like to end this section with a comparison between the expected performance of the CMS detector with the performance of the ATLAS detector. This comparison is summarized in the tables 3.1, 3.2 , 3.3, 3.4 and 3.5. From these tables we can conclude that both ATLAS and CMS have high granularity both in the electromagnetic and hadronic calorimeters. The resolution of the calorimeters of both detectors is also good although CMS has better resolution than ATLAS in the ECAL and in muon detection and ATLAS a better resolution in the HCAL.

In this work all the samples with detector simulation are done using a card that characterizes the CMS detector. This card is a default one provided within Delphes framework. A detailed description of this card will be given in the next chapter.

	ATLAS	**CMS**
Reconstruction efficiency for muons with $p_T = 1GeV$	96.8 %	97.0 %
Reconstruction efficiency for pions with $p_T = 1GeV$	84.0 %	80.0 %
Reconstruction efficiency for electrons with $p_T = 5GeV$	90.0 %	85.0 %
Momentum resolution at $p_T = 1$ GeV and $\eta \approx 0$	1.3 %	0.7 %
Momentum resolution at $p_T = 1$ GeV and $\eta \approx 2.5$	2.0 %	2.0 %
Momentum resolution at $p_T = 100$ GeV and $\eta \approx 0$	3.8 %	1.5 %
Momentum resolution at $p_T = 100$ GeV and $\eta \approx 2.5$	11 %	7 %
Transverse i.p. resolution at $p_T = 1$ GeV and $\eta \approx 0(\mu m)$	75 %	90 %
Transverse i.p. resolution at $p_T = 1$ GeV and $\eta \approx 2.5(\mu m)$	200 %	220 %
Transverse i.p. resolution at $p_T = 1000$ GeV and $\eta \approx 0(\mu m)$	11 %	9 %
Transverse i.p. resolution at $p_T = 1000$ GeV and $\eta \approx 2.5(\mu m)$	11 %	11 %
Longitudinal i.p. resolution at $p_T = 1$ GeV and $\eta \approx 0(\mu m)$	150 %	125 %
Longitudinal i.p. resolution at $p_T = 1$ GeV and $\eta \approx 2.5(\mu m)$	900 %	1060 %
Longitudinal i.p. resolution at $p_T = 1000$ GeV and $\eta \approx 0(\mu m)$	90 %	22-42 %
Longitudinal i.p. resolution at $p_T = 1000$ GeV and $\eta \approx 2.5(\mu m)$	190 %	70 %

Table 3.1: Main performance characteristics of the ATLAS and CMS trackers. Examples of typical reconstruction efficiencies, momentum resolutions and transverse and longitudinal impact parameter are given for various particle types, transverse momentum and pseudorapidities. Extracted from [66]

	ATLAS		**CMS**	
Technology	Lead/LAr accordion		$PbWO_4$ scintillating crystals	
Channels	Barrel	End caps	Barrel	End caps
	110,208	63,744	61,200	14,648
Granularity		$\Delta\eta \times \Delta\phi$		$\Delta\eta \times \Delta\phi$
Presampler	0.025×0.1	0.025×0.1		
Strips/ Si-preshower	0.003×0.1	0.003×0.1 to 0.006×0.1		32×32 Si-strips per 4 crystals
Main Sampling	0.025×0.025	0.025×0.025	0.017×0.017	0.018×0.003 to 0.088×0.015
Back	0.05×0.025	0.05×0.025		
Depth	Barrel	End caps	Barrel	End caps
Presampler (LAr)	10 mm	2×2 mm		
Strips/ Si-preshower	$\approx 4.3X_0$	$\approx 4.0X_0$		$3X_0$
Main sampling	$\approx 16X_0$	$\approx 20X_0$	$26X_0$	$25X_0$
Back	$\approx 2X_0$	$\approx 2X_0$		
Noise per cluster	250 MeV	250 MeV	200 MeV	600 MeV
Intrinsic resolution	Barrel	End caps	Barrel	End caps
Stochastic term a	10%	10 to 12 %	3 %	5.5 %
Local constant term b	0.2 %	0.35 %	0.5 %	0.5 %

Table 3.2: Main parameters of the ATLAS and CMS electromagnetic calorimeters. The intrinsic energy resolutions are quoted as parametrizations of the type $\sigma(E)/E = a/\sqrt{E} \oplus b$. For the ATLAS EM barrel and end-cap calorimeters and for the CMS barrel crystals the numbers quoted here are based on stand-alone test-beam measurements. Extracted from [66]

	ATLAS	**CMS**
Technology		
Barrel/Ext. barrel	14 mm iron/3 mm scint.	50 mm brass/3.7 mm scint.
End caps	25-50 mm copper/8.5 mm LAr	78 mm brass/3.7 mm scint.
Forward	Copper(front) - Tungsten (back)/0.25-0.50 mm LAr	Steel/0.6 mm quartz
Channels		
Barrel/Ext. barrel	9852	2592
End caps	5632	2592
Forward	3524	1728
Granularity ($\Delta\eta \times \Delta\phi$)		
Barrel/Ext. barrel	0.1×0.1 to 0.2×0.1	0.087×0.087
End caps	0.1×0.1 to 0.2×0.2	0.087×0.087 to 0.18×0.175
Forward	0.2×0.2	0.175×0.175
Samplings ($\Delta\eta \times \Delta\phi$)		
Barrel/Ext. barrel	3	1
End caps	4	2
Forward	3	2
Abs. lengths (min. - max.)		
Barrel/Ext.barel	9.7-13.0	7.2 - 11.0 10-14 (with coil/HO)
End caps	9.7-12.5	9.0-10.0
Forward	9.5-10.5	9.8

Table 3.3: Main parameters of the ATLAS and CMS hadronic calorimeters. Extracted from [66]

	ATLAS				**CMS**	
	Barrel LAr/Tile		**End – cap LAr**			
	Tile	**Combined**	**HEC**	**Combined**	**Had.barrel**	**Combined**
Stochastic term	$45\%/\sqrt{E}$	$55\%/\sqrt{E}$	$75\%/\sqrt{E}$	$85\%/\sqrt{E}$	$100\%/\sqrt{E}$	$70\%/\sqrt{E}$
Constant term	1.3%	2.3%	5.8%	<1%		8.0%
Noise	Small	3.2 GeV		1.2 GeV	Small	1 GeV

Table 3.4: Comparison between the expected resolutions of the ATLAS and CMS hadronic calorimeters. Extracted from [66].

	ATLAS	**CMS**
Drift Tubes	MDTs	DTs
-Coverage	$\|\eta\| < 2.0$	$\|\eta\| < 1.2$
-Number of chambers	1170	250
-Number of channels 354000	172000	
-Function	Precision measurement	Precision measurement, triggering
Cathode Strip Chambers		
-Coverage	$2.0 < \|\eta\| < 2.7$	$1.2 < \|\eta\| < 2.4$
-Number of chambers	32	468
-Number of channels	31000	500000
-Function	Precision measurement	Precision measurement, triggering
Resistive Plate		
-Coverage	$\|\eta\| < 1.05$	$\|\eta\| < 2.1$
-Number of chambers	1112	912
-Number of channels	374000	160000
-Function	Triggering, second coordinate	Triggering
Thin Gap Chambers		
-Coverage	$1.05 < \|\eta\| < 2.4$	-
-Number of chambers	1578	-
-Number of channels	322000	-
-Function	Triggering, second coordinate	-
Combined (stand-alone) momentum resolution at		
-$p = 10$ GeV and $\eta \approx 0$	1.4%(3.9%)	0.8%(8%)
-$p = 10$ GeV and $\eta \approx 2$	2.4%(6.4%)	2.0%(11%)
-$p = 100$ GeV and $\eta \approx 0$	2.6%(3.1%)	1.2%(9%)
-$p = 100$ GeV and $\eta \approx 2$	2.1%(3.1%)	1.7%(18%)
-$p = 1000$ GeV and $\eta \approx 0$	10.4%(10.5%)	4.5%(13%)
-$p = 1000$ GeV and $\eta \approx 2$	4.4%(4.6%)	7.0%(35%)

Table 3.5: Main parameters of the ATLAS and CMS muon chambers as well as a summary of the expected combined and stand-alone performance at two typical pseudorapidity values (averaged over azimuth). Adapted from [66]

Chapter 4

Monte Carlo Generation, Simulation and Reconstruction

To study a process of interest (signal) or other processes that mimic the interesting process (backgrounds), as well their physical properties, we need to use large samples of simulated events. In this chapter we give a brief description of all the necessary steps to achieve a good simulation. We start by giving a short description of PDFs in section 4.1. In section 4.2 we do a summary of the processes that we will generate in this work. Next we talk about the event generator used in this work as well as the implementation of tha lagrangian 2.6 in a suitable format to start event generation in section 4.3. In the remaining of this we talk about hadronization and detector simulation. The chain necessary to a successful simulation is presented in figure 4.1.

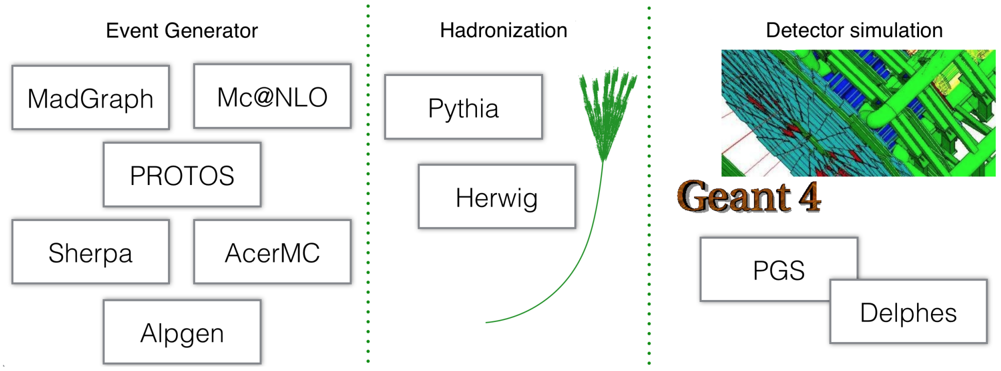

Figure 4.1: The steps of an event simulation ordered from the left to the right. Examples of software used in each step are given.

4.1 Parton Distribution Functions

In 1969 Feynman proposed that the proton and the neutron (as well other hadrons) were made of particles that he called partons [67]. Nowadays we associate these partons with the quarks and the gluons. Then inside the proton (or any other hadron) we can find quarks, gluons and a sea of virtual quark-antiquark pairs generated by the gluons which hold the quarks inside the proton. The quarks that determine the quantum number of the proton (an hadrons in general) are called valence quarks. In the case of the proton the valence quarks are two up quarks and one down quarks. In the sea of virtual quark-antiquark pairs we can find other quark flavours (e.g. strange quark).

At the LHC we are colliding protons with protons. Since the protons are made of partons, the events we observe are the result of a collision between their partons. This demands a detailed knowledge momentum distribution of all the partons. Moments before the collision the protons have a very large momentum since their energies are much higher than their masses. In this frame the momentum of the parton is almost collinear with the proton momentum. This means that we can think of the proton as a stream of partons before the collision. A given parton will have a fraction x of the longitudinal momentum of the proton. The distribution functions that give the probability of a parton having a fraction x of the longitudinal momentum of the proton at a squared energy scale Q^2 are known as the Parton Distribution Functions (PDFs) of the proton.

The PDFs cannot be calculated perturbatively and are determined experimentally through deep inelastic scattering between leptons and the proton or in jet production at colliders. Their evolution as a function of the energy scale involvel Q^2 is given by the DGLAP equations [68, 69, 70]. These equations are not capable of giving the x dependence which is extracted by data gathered in experiments.

4.2 Signal and Background processes

In this work we analyze the properties of $t\gamma$, tZ and tH production. In the $t\gamma$ and tH production we perform only a basic analysis at the parton-level and neglect the decay products, while in tZ processes we perform an analysis at parton-level and at reconstruction-level. In the tZ case the events $tZ \to W^+bl^+l^-$ and $\bar{t}Z \to W^-\bar{b}l^+l^-$ in which the W bosons decay in the leptonic channel $W \to l\nu_l$ constitute our signal

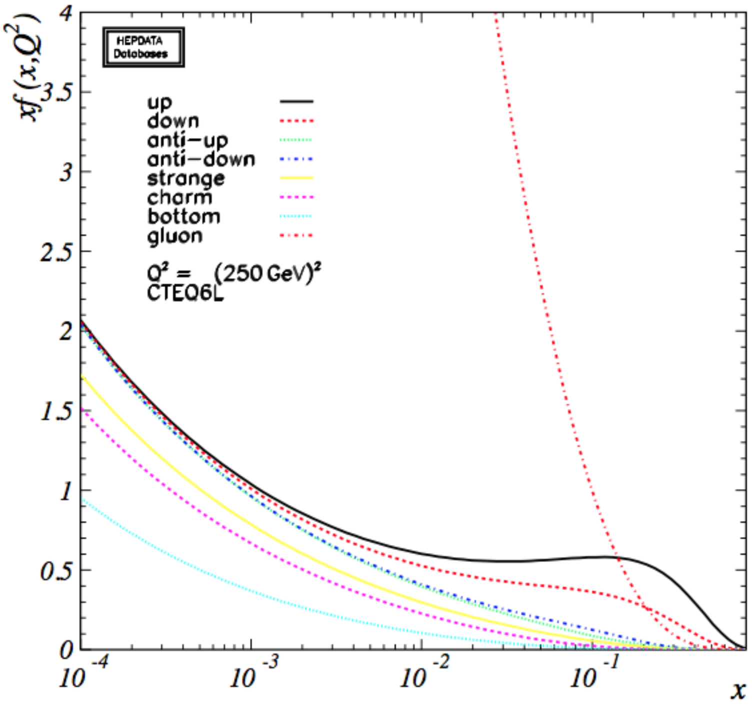

Figure 4.2: Parton Distribution Functions for $Q^2 = (250GeV)^2$, evaluated by CTEQ Collaboration. Extracted from [65]

events. The topology of these events is characterized by three leptons with high p_T, a b -tagged jet and missing transverse energy due to the existence of a neutrino. The Standard Model processes that mimic are the diboson processes WW + jets, WZ + jets and ZZ + jets decaying fully leptonically, Z + jets in the dilepton channel, Standard Model tZq production in the three lepton channel , $t\bar{t}$ + jets and single top production in the tW channel. These last two are allowed to decay in any channel. In this work we will only consider the Diboson background processes, since at a centre-of-mass energy of $\sqrt{s} = 7$ TeV they account to approximately 75 % of the background events [19].

4.3 Event Generation, MadGraph and FeynRules

The sample generation was performed using the Monte Carlo generator MadGraph5@MCNLO [72]. Madgraph5@MCNLO (from now on referred just as MadGraph) is capable of generating parton-level samples of any process within the Standard Model or of any process of any New Physics model provided we pass to MadGraph the model in an appropriate format. MadGraph is very versatile since it allows to generate Standard Model processes at Next-to-Leading Order (NLO), to apply cuts in the phase-space during the parton-level generation as well as change the value of the parameters of the model which allows us to study how physical observables depend on the parameters of the model. After the parton-level generation it is possible to simulate radiation and hadronization of the events through the packages Herwig [73] and Pythia [74]. It is also possible to perform a detector simulation using Delphes [75] or PGS after the step of radiation and hadronization.

To generate processes within the context of a physical model, MadGraph needs a set of files that contains the Feynman rules in momentum-space of the model as well relevant information like the particles masses and coupling constants of the model. In the past this set of files needed to be written manually, that is, we needed first to compute all the Feynman rules of the model an then implement them one by one in a very specific readable format. Nowadays the Mathematica FeynRules [76] package allows to write these files in a fast and efficient way. The FeynRules process is divided in two stages. In the first stage we write a .fr file where we define the gauge groups of the model, the particles of the model, the parameters of the model and the lagrangian. After this we write a Mathematica notebook where we load FeynRules which contain a set of functions that after reading the .fr file created in the previous step write the relevant files to MadGraph in an Universal FeynRules Output (UFO) format [77]. This UFO format is basically a folder with the name of the model that has inside Python files with all the Feynman rules defined. To see how a detailed explanation of how to implement a model in FeynRules we refer to the FeynRules manual. In the next section we show how we implemented our model in FeynRules. The UFO model produced will enable MadGraph to generate events at leading order only.

4.3.1 Model Implementation in FeynRules

In our model we do not have additional particles and symmetries in comparison with the Standard Model. However since we are defining new interactions between the top quark , up and charm quarks and gauge bosons we need to write in a .fr file the lagrangian and define the parameters that appear in the lagrangian. All the model parameters are implemented as elements of the list M$ Parameters,

```
M\$Parameters = {
  param1 = = {options1},
  param2 = = {options2},
             ...
```

```
    };
```

param1 and param2 are user defined names that are used when writing the lagrangian. The parameters can either be scalar or tensorial. In our model we use only scalar parameters. In general the parameters can be classified as internal or external. The external parameters are the ones with values set by the user while internal parameters are the ones which are defined in terms of the external parameters or even in terms of other internal parameters. We can think of the external parameters as the ones we can measure experimentally. The internal parameters can be either real or complex but the external parameters can only be real parameters.

The parameters in the lagrangian 2.6 are complex numbers in general but they must be defined in FeynRules as external parameters. To solve this difficulty we define in FeynRules our external parameters as the real and imaginary parts of the parameters that appear in the lagrangian. We give the example of the definition of the real and imaginary parts of the parameter X^L_{ut} :

```
ReXLut == { TeX -> Subscript[ReX,Lut], ParameterType -> External, Value -> 0.0,
     BlockName -> NEWCOUP, OrderBlock -> 1, InteractionOrder -> {NP,1} },
ImXLut  == { TeX -> Subscript[ImX,Lut], ParameterType -> External, Value -> 0.0,
     BlockName -> NEWCOUP, OrderBlock -> 2, InteractionOrder -> {NP,1} },
```

In generating the UFO we also load a file called SM.fr which is necessary to incorporate the Standard Model. This file is downloadable from the MadGraph online page. In tables 4.1 and 4.2 you find respectively a summary of all the SM parameters and of the anomalous couplings of our model.

With the parameters defined we only need to write our lagrangian in the .fr file. We did that by considering the total lagrangian as the sum of the Standard Model lagrangian with the lagrangian 2.6. We also broke the lagrangian 2.6 in four lagrangians: a lagrangian that describes the Higgs couplings, a lagrangian that describes the gluon couplings, a lagrangian that describes the Z couplings and a lagrangian that describes the couplings with the photon. We will not reproduce this part of the code entirely here. We just show the implementation of the Higgs couplings. The entire code used is public and the interested reader can examine it with more detail in [78]. The FeynRules for the Higgs couplings is

```
LHiggsFCNC := Block[{la},
la = -((ReEtaLut+I*ImEtaLut)/Sqrt[2])*(ubar.ProjM.t)*H-((ReEtaRut+I*ImEtaRut)/Sqrt
    [2])*(ubar.ProjP.t)*H
```

Parameter	Symbol	MG Symbol	Value
SMINPUTS BLOCK			
Inverse of the electromagnetic coupling	$\alpha_{EW}^{-1}(M_Z)$	aEWM1	127.9
Fermi constant	G_F	Gf	$1.166 \times 10^{-5}\ GeV^{-2}$
Strong coupling	$\alpha_s(M_Z)$	aS	0.118
MASS BLOCK			
u quark pole (Yukawa) mass	$m_u^{(Yuk.)}$	MU (ymup)	5.04×10^{-3} GeV
d quark pole (Yukawa) mass	$m_d^{(Yuk.)}$	MD (ymdo)	2.55×10^{-3} GeV
c quark pole (Yukawa) mass	$m_c^{(Yuk.)}$	MC (ymc)	1.27 GeV
s quark pole (Yukawa) mass	$m_s^{(Yuk.)}$	MS (yms)	1.01×10^{-1} GeV
t quark pole (Yukawa) mass	$m_t^{(Yuk.)}$	MT (ymb)	172 GeV
b quark pole (Yukawa) mass	$m_b^{(Yuk.)}$	MB (ymb)	4.7 GeV
Z pole mass	m_Z	MZ	91.19 GeV
Higgs mass	m_h	MH	125 GeV
electron pole (Yukawa) mass	$m_e^{(Yuk.)}$	Me (yme)	5.11×10^{-4} GeV
muon pole (Yukawa) mass	$m_\mu^{(Yuk.)}$	MMU (ymmm)	1.0566×10^{-1} GeV
τ pole (Yukawa) mass	$m_\tau^{(Yuk.)}$	MTA (ymtau)	1.777 GeV
DECAY BLOCK			
t quark width		WT	1.508 GeV
Z boson width		WZ	2.495 GeV
W boson width		WW	2.085 GeV
Higgs boson width		WH	4.07×10^{-3}
CKM BLOCK			
Cabibbo angle	$\sin\theta_C$	cabi	2.277×10^{-1}

Table 4.1: SM default parameters in param_card.dat. Neutrino masses and Yukawa couplings are set to zero and by this reason are omitted in the table. In the CKM matrix it is assumed that there is only mixing between the first and second quark families

```
-((REtaLct+I*ImEtaLct)/Sqrt[2])*(cbar.ProjM.t)*H-((REtaRct+I*ImEtaRct)/Sqrt[2])
    *(cbar.ProjP.t)*H;
    la + HC[la]];
```

where ProjM and ProjP are respectively the projectors $\frac{1-\gamma^5}{2}$ and $\frac{1+\gamma^5}{2}$; ubar/cbar is $\bar{u}/\bar{c}$; I is the imaginary unit; and H is the Higgs field. To verify that no mistakes were committed we checked for the hermiticity of the lagrangian and the mass spectrum of our model using the functions CheckHermiticity and CheckMassSpectrum of FeynRules. The function CheckHermiticity basically computes de number of vertices $\mathcal{L}-\mathcal{L}^\dagger$ which must be zero if the lagrangian is hermitian. Our implemented lagrangian passed this test. The function CheckMassSpectrum checks if the mass terms are diagonal and displays a comparison between the input values (see table 4.1) and a numerical value computed by it. It is found that the mass terms are diagonal and that the computed values are the same the ones in table 4.1.

Parameter	Symbol	MG Symbol	Default Value
Real part of X_{ut}^L	$\mathrm{Re}X_{ut}^L$	ReXLut	0
Imaginary part of X_{ut}^L	$\mathrm{Im}X_{ut}^L$	ImXLut	0
Real part of X_{ut}^R	$\mathrm{Re}X_{ut}^R$	ReXRut	0
Imaginary part of X_{ut}^R	$\mathrm{Im}X_{ut}^R$	ImXRut	0
Real part of X_{ct}^L	$\mathrm{Re}X_{ct}^L$	ReXLct	0
Imaginary part of X_{ct}^L	$\mathrm{Im}X_{ct}^L$	ImXLct	0
Real part of X_{ct}^R	$\mathrm{Re}X_{ct}^R$	ReXRct	0
Imaginary part of X_{ct}^R	$\mathrm{Im}X_{ct}^R$	ImXRct	0
Real part of K_{ut}^L	$\mathrm{Re}K_{ut}^L$	ReKLut	0
Imaginary part of K_{ut}^L	$\mathrm{Im}K_{ut}^L$	ImKLut	0
Real part of K_{ut}^R	$\mathrm{Re}K_{ut}^R$	ReKRut	0
Imaginary part of K_{ut}^R	$\mathrm{Im}K_{ut}^R$	ImKRut	0
Real part of K_{ct}^L	$\mathrm{Re}K_{ct}^L$	ReKLct	0
Imaginary part of K_{ct}^L	$\mathrm{Im}K_{ct}^L$	ImKLct	0
Real part of K_{ct}^R	$\mathrm{Re}K_{ct}^R$	ReKRct	0
Imaginary part of K_{ct}^R	$\mathrm{Im}K_{ct}^R$	ImKRct	0
Real part of ζ_{ut}^L	$\mathrm{Re}\zeta_{ut}^L$	ReZetaLut	0
Imaginary part of ζ_{ut}^L	$\mathrm{Im}\zeta_{ut}^L$	ImZetaLut	0
Real part of ζ_{ut}^R	$\mathrm{Re}\zeta_{ut}^R$	ReZetaRut	0
Imaginary part of ζ_{ut}^R	$\mathrm{Im}\zeta_{ut}^R$	ImZetaRut	0
Real part of ζ_{ct}^L	$\mathrm{Re}\zeta_{ct}^L$	ReZetaLct	0
Imaginary part of ζ_{ct}^L	$\mathrm{Im}\zeta_{ct}^L$	ImZetaLct	0
Real part of ζ_{ct}^R	$\mathrm{Re}\zeta_{ct}^R$	ReZetaRct	0
Imaginary part of ζ_{ct}^R	$\mathrm{Im}\zeta_{ct}^R$	ImZetaRct	0
Real part of η_{ut}^L	$\mathrm{Re}\eta_{ut}^L$	ReEtaLut	0
Imaginary part of η_{ut}^L	$\mathrm{Im}\eta_{ut}^L$	ImEtaLut	0
Real part of η_{ut}^R	$\mathrm{Re}\eta_{ut}^R$	ReEtaRut	0
Imaginary part of η_{ut}^R	$\mathrm{Im}\eta_{ut}^R$	ImEtaRut	0
Real part of η_{ct}^L	$\mathrm{Re}\eta_{ct}^L$	ReEtaLct	0
Imaginary part of η_{ct}^L	$\mathrm{Im}\eta_{ct}^L$	ImEtaLct	0
Real part of η_{ct}^R	$\mathrm{Re}\eta_{ct}^R$	ReEtaRct	0
Imaginary part of η_{ct}^R	$\mathrm{Im}\eta_{ct}^R$	ImEtaRct	0
Real part of λ_{ut}^L	$\mathrm{Re}\lambda_{ut}^L$	ReLambdaLut	0
Imaginary part of λ_{ut}^L	$\mathrm{Im}\lambda_{ut}^L$	ImLambdaLut	0
Real part of λ_{ut}^R	$\mathrm{Re}\lambda_{ut}^R$	ReLambdaRut	0
Imaginary part of λ_{ut}^R	$\mathrm{Im}\lambda_{ut}^R$	ImLambdaRut	0
Real part of λ_{ct}^L	$\mathrm{Re}\lambda_{ct}^L$	ReLambdaLct	0
Imaginary part of λ_{ct}^L	$\mathrm{Im}\lambda_{ct}^L$	ImLambdaLct	0
Real part of λ_{ct}^R	$\mathrm{Re}\lambda_{ct}^R$	ReLambdaRct	0
Imaginary part of λ_{ct}^R	$\mathrm{Im}\lambda_{ct}^R$	ImLambdaRct	0

Table 4.2: Adjustable parameters of $\mathcal{L}_{topFCNC}$ in param_card.dat . Remember that in general the parameters are complex, hence you need to specify both their real and imaginary parts.

4.4 Hadronization

After the collision between two protons free quarks and gluons are created. According to color confinement the color charged particles cannot be directly observed. This means that the quarks and gluons must combine themselves in colour neutral states known as hadrons, being the proton an example. This process is known as hadronization.

This process is a non-perturbative one [79] and as a consequence there is not an explicit calculation of this process. However phenomenological models have been created [80] and implemented in Monte Carlo generators like Pythia or Herwig. Pythia and Herwig use different models to simulate hadronization [81, 82, 82].

4.5 Detector Simulation - Delphes

In order to compare a theory prediction to experiment in particle physics it is mandatory to perform a full detector simulation. This simulation is usually done with Geant4 [71]. In the proton collisions at the LHC a lot of particles are produced including long-lived and small-lived particles. The former also decay to long-lived particles an is this kind of particles that is detected. The detection process is just the interaction of the long-lived particles with the matter present in the detectors. The Geant4 simulates these interactions taking in to account the geometry of the detector, the matter composition of the detector, the magnetic field an even showering processes inside the detector. However, this precise description has the cost of being computationally heavy and only accessible to large collaborations like ATLAS or CMS. To do phenomenological work it is sufficient to do a fast-simulation of the detectors. This goal is achieved by the Delphes framework [75].

In Delphes the detector is assumed to be composed of an inner tracker, an electromagnetic and hadron calorimeter and a muon system. The detector has cylindrical symmetry around the beam axis and the components are concentric to each other. The user can specify its active volume, calorimeter segmentation and magnetic field intensity. The firs step carried by Delphes is to simulate how the particles propagate in the inner tracker. Of course neutral particles will propagate in a straight line and charged ones will have a helicoidal trajectory. The probability of reconstruction a track and energy and momentum resolutions can be set by the user based on the particle type, transverse momentum and pseudo-rapidity.

After the long-lived particle leaves the inner tracker it reaches the electromagnetic calorimeters and hadronic calorimeters where energy deposits will be simulated. Each calorimeter is divided in cells with each cell having coordinates (η, ϕ) and a size set by the user. The granularity of the electromagnetic calorimeter is the same as the granularity of the hadronic calorimeter. The geometric centre of each cell is the coordinate of the deposited energy of the particle. In general long-lived particles reach both calorimeters and deposit a fraction of their energies in each calorimeter (f_{ECAL} and f_{HCAL}). A calorimeter tower is then formed. In Delphes it is assumed that electrons, positrons and photons deposit all their energy in the electrogmanetic calorimeter ($f_{ECAL} = 1$) and that stable hadrons are assumed to deposit all their energy in the hadronic calorimeter ($f_{HCAL} = 1$). Particles like Kaons and Λ are assumed to deposit energy according to the dominant decay products of such particles. These value of the fractions can be also be changed by the user. The resolutions of the calorimeters are independent and calculated by the equation

$$(\frac{\sigma}{E})^2 = (\frac{S(\eta)}{\sqrt{E}})^2 + (\frac{N(\eta)}{E})^2 + C(\eta)^2 \tag{4.1}$$

where S,N and C are respectively the stochastic, noise and constant terms. The energy of the tower is then

$$E_{Tower} = \sum_{particles} \ln \mathcal{N}(f_{ECAL} \cdot E, \sigma_{ECAL}(E, \eta)) + \ln \mathcal{N}(f_{HCAL} \cdot E, \sigma(E, \eta)) \tag{4.2}$$

where the sum is over all the particles that reach the tower and $\mathcal{N}(m, s)$ is the log-normal distribution with mean m and variance s. A uniform smearing of the position is used to avoid discrete tower positions.

From the information of the subdetectors Delphes reconstructs the event through the particle-flow approach. In Delphes this algorithm creates two collections of 4-vectors : particle-flow tracks and particle-flow towers. Let E_{ECAL} and E_{HCAL} be the total energy deposition at the electromagnetic and hadronic calorimeter respectively. Also, let $E_{ECAL,trk}$ and $E_{HCAL,trk}$ be the total energy deposited respectively in the electromagnetic and hadronic calorimeter that originates from charged particles for which the tracks have been reconstructed. Then they define

$$\Delta_{ECAL} = E_{ECAL} - E_{ECAL,trk}, \quad \Delta_{HCAL} = E_{HCAL} - E_{HCAL,trk} \tag{4.3}$$

$$E^{eflow}_{Tower} = max(0, \Delta_{ECAL}) + max(0, \Delta_{HCAL}) \tag{4.4}$$

The particle flow is then performed by assigning a particle-flow track to each reconstructed track and a particle-flow tower is created if $E^{eflow}_{Tower} > 0$

After this stage of event reconstruction Delphes performs a reconstruction of the relevant physics objectos. Like in a real life experiment this reconstruction is done using the information collected in the inner trackers and calorimeters. The reconstruction efficiency can be set by the user and is a function of the p_T , η and of energy. The resolutions are also parameterized by the user. Concerning jets in general Delphes uses the FASTJET package to reconstruct jets. Specifically in the case of b and τ - tagged jets a potential jet becomes $b - jet$ or a $\tau - jet$ if for a distance inferior to $\Delta R = \sqrt{(\eta^{jet} - \eta^{b,\tau})^2 + (\phi^{jet} - \phi^{b,\tau})^2}$ from the jet axis there is a generated b or τ from simulation. Tagging and mis-tagging efficiencies can also be set by the user. The missing transverse energy is defined by

$$\vec{E}^{miss}_T = -\sum_i \vec{p}_T(i) \tag{4.5}$$

where i runs over the selected input. There is also a E^{miss}_T associated with tracks and a E^{miss}_T with calorimeters.

If we want to study the sensibility of the LHC to the tZ production we should use a fast-simulation of either ATLAS or CMS detectors. The Delphes framework has at disposal cards that parametrize these detectors. In this work we focus only on one that parameterizes the CMS detector. In this card you can set all the parameters previously described. In the following section we explain how and where all these parameters can be set in the card.

4.5.1 Delphes parameterization

Delphes starts to compute how the charged particles propagate inside a cylinder of radius R with a magnetic field B. These values are set in the module ParticlePropagator. Then you can set the charged hadrons, electrons and muons tracking efficiencies as functions of the pseudo-rapidity and transverse momentum in the modules Charged-

HadronTrackingEfficiency , ElectronTrackingEfficiency and MuonTrackingEfficiency respectively. Then particles momentum and energies are smeared with the user parameterized funcions ChargedHadronMomentumSmearing, ElectronEnergySmearing and MuonMomentumSmearing.

The response of the calorimeters is set on the module Calorimeter. Here you can set the granularity of the calorimeters , the energy fraction that a given particle deposits in each calorimeter and the resolution of the calorimeters as a function of energy and pseudo-rapidity. The reconstruction efficiencies as functions of pseudo-rapidity and transverse momentum can be costumized in the modules PhotonEfficiency, ElectronEfficiency and MuonEfficiency respectively. The definition of an isolated photon, electron or muon are set in PhotonIsolation, ElectronIsolation and MuonIsolation. At the end of calorimeter response simulation Delphes can compute the missing transverse energy and this is done in MissingET module.

The reconstruction jet algorithms and their parameters can be set in the modules GenJetFinder and FastJetFincer. The efficiencies for tagging and misidentification of b and τ tagged jets can be changed in the modules BTagging and TauTagging. The probability of mistag for τ leptons is set to 40 % while for the electron and muon leptons this probability is 0.1 %. Concerning jets and b-jets the R parameter in FastJet algorithm [84] is defined to be 0.4. The efficiency for b-tag efficiency as well as misidentification is a function of the transverse momentum of the b-jet as well of its pseudo-rapidity.

Chapter 5

Event Analysis

After event generation we started to study the physical properties of the samples obtained. In this section we describe the analysis performed for $t\gamma$, tH and tZ processes. Parton-level results were obtained by using the MadAnalysis framework which is described in section 5.1. The implemented analysis and the results obtained for $t\gamma$ and tH are presented in sections 5.2 and 5.3 respectively. For tZ we did not only an analysis at parton-level but also a reconstruction-level analysis based on CMS [19] which is described in section 5.4. The reconstruction-level analysis was performed using a dedicated code.

5.1 Parton-level Analysis with MadAnalysis

The parton-level analysis performed on the $t\gamma$, tH and tZ processes with the MadAnalysis [85, 86] framework. Basically a C++ code was designed to read events from the output of MadGraph and for each event the desired particles were searched for. The code is divided in two files: a .h header file were we define the histograms and global variables; and a .cpp source file where the analysis is defined.

In order to explain the structure of the code let us focus in the $t\gamma$ case. Although the other processes have different particles involved the structure of the corresponding codes is very similar. In .cpp file we have three defined functions: Initialize, Finalize and Execute.

In the Initialize function is where we define the properties of the histograms such has its name, the number of bins as well as the minimum and the maximum of the X axis. An example is given by the following code :

```
bool analise_tgamma::Initialize(function parameters)
{
    PHYSICS->mcConfig().Reset();
    topPTHisto = new TH1F ("topPTHisto", "top␣PT",50,0,500);
    topEtaHisto = new TH1F("topEtaHisto","top␣Eta",50,-6,6);
    topPhiHisto = new TH1F("topPhiHisto","top␣Phi",20,-3.15,3.15);
    topEnergyHisto = new TH1F("topEnergyHisto","top␣Energy",50,0,500);
        ....
}
```

The last function to be called by the program is Finalize. Within this function the user can draw and store histograms of relevant physical quantities in a root file. The structure of this function is the following :

```
void analise_CMS::Finalize(function parameters)
{
    TFile* myOutput = new TFile("myOutput.root","RECREATE");
    myOutput->cd();

    topPTHisto->Write();
    topEtaHisto->Write();
    topPhiHisto->Write();
    topEnergyHisto->Write();
        ....
}
```

The function Execute is the core of the analysis because it is within this function that we define the cuts to apply to the events as well where we fill the histograms of the physical observables. Here MadAnalysis provides a set of tools that allows us to extract relevant from the particles present in the event that can be used for the application of the cuts and filling the histograms. The following code is a portion of the one we used for $t\gamma$. The code for the other processes is very similar to this one :

```
bool analise_tgamma::Initialize(function parameters)
{
    unsigned int n = event.mc()->particles().size();
    for (unsigned int i=0; i<n; i++){
        MCParticleFormat* prt = &event.mc()->particles()[i];
        if (fabs(prt.pdgid())==6){
            topPTHisto->Fill(prt.pt());
            topPhiHisto->Fill(prt.phi());
            topEtaHisto->Fill(prt.eta());
            topEnergyHisto->Fill(prt.e());
        }
        ....
}
```

A for cycle over the vector `event.mc()->particles()` , which contains all the particles of the event, is done in order to fill the histograms of the kinematics under study. The particles are a MCParticleFormat object and are identified by their PDG-id [38]. In order to fill the histograms of the p_T, η, ϕ and Energy of the top quark we wrote an if clause that selects particles whose absolute value of the PDG-id is equal to six. MCParticleFormat objects have functions that allow us to get the values of kinematical variables as well as their 4-momentum (through the function `prt.momentum()`). To get the histograms of the photon we did a similar if clause, but the condition is a particle with a PDG-id value of 22.

5.2 tγ Analysis

The effect of the anomalous couplings in $t\gamma$ processes was searched in the energy , p_T , η and ϕ distributions of the top quark and of the photon as well on the energy and mass distributions of the $t\gamma$ system. To achieve several samples with $t\gamma$ processes were generated at $\sqrt{s} = 13$ TeV using MadGraph and the UFO we implemented. The PDF set used for this generations was NN23LO1 [87]. The Feynman diagrams that contribute for this process are presented in figure 5.1.

From those Feynman diagrams we conclude that there are four kinds of anomalous couplings : a coupling between the up and top quarks with the gluon (gut); a coupling between the charm and top quarks with the gluon (gct); a coupling between the up and top quarks with the photon(γut); and a coupling between the charm and top quarks with the photon (γct). Each of this couplings is described by left-handed and right-handed parameters whose values define the chirality of the coupling (see 2.6). Because the cross-section of $t\gamma$ is proportional to the sum of the squares of the modulus of these two parameters we define the coupling strength of a given coupling as the square root of this sum.

In order to study the physical properties of tγ as a function of the coupling nature, of the chirality and of the coupling strength each generated sample had different values for the anomalous couplings. To study the effect of the coupling nature, we used samples with the same chirality and coupling strength but with different coupling nature behind the production. To study the effect of chirality, we used samples with the same coupling nature and coupling strength but with different chiralities. The study of the effect of the coupling strength was performed using samples with the

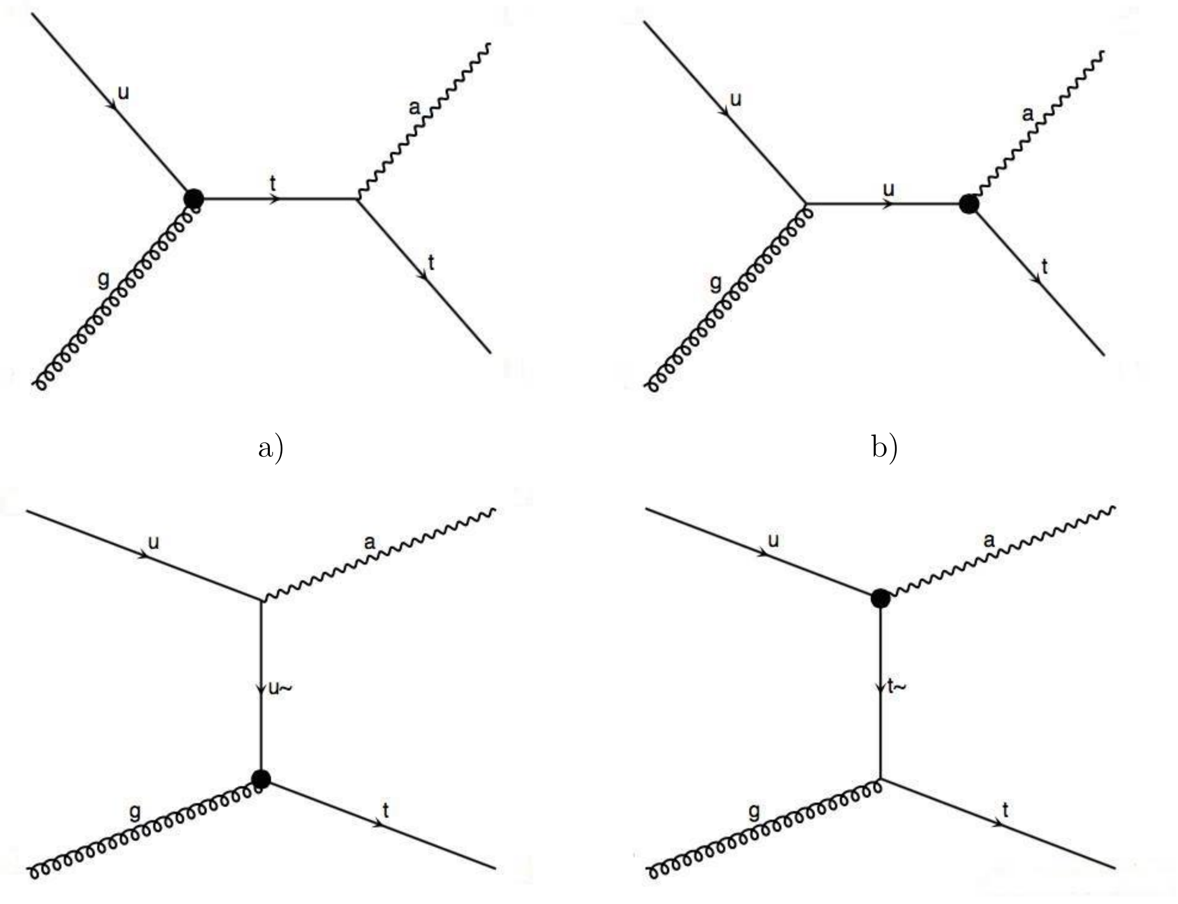

a) b)

c) d)

Figure 5.1: Feynman diagrams for $t\gamma$ production involving couplings with an up quark. Diagrams a) and b) are the s-channel diagrams while c) and d) are the t-channel diagrams. Diagrams with a charm quark are analogous to these ones.

same chirality and coupling nature but with different coupling strengths

The energy, p_T, η and ϕ distributions were obtained by using built-in functions of MadAnalysis. The distributions of the $t\gamma$ system were obtained by computing its 4-momentum. MadAnalysis has a function that for a given particle in the event it returns its 4-momentum. Hence we asked MadAnalysis for the 4-momentum of the top quark and of the photon and added these two Lorentz vectors.

We only observed differences in the kinematical distributions with the same chiralities and coupling strength but with different coupling natures and hence only these differences will be shown. These results are presented in figures 5.2, 5.3 and 5.4. As can be seen from these figures anomalous couplings with the photon produce more energetic photons and top quarks than anomalous couplings with the gluon. Also, by conservation of energy, anomalous couplings with the photon produce events with higher energy in the $t\gamma$ system. Another thing we can notice is that anomalous couplings with the up quark produce more energetic photons and top quarks than the anomalous couplings with the charm quark. The same conclusions can be taken for the transverse momentum of the photon of the top quark.

5.3 tH Analysis

The sample generation and analysis of the tH system is analogous to the analysis of the $t\gamma$. For this reason we will only present in this section the Feynman diagrams (see figure 5.5) responsible for the production of this process as well as the distributions obtained (see figures 5.6, 5.7 and 5.8). From these distributions we conclude that the anomalous couplings with the up quark are more likely to produce more energetic top quarks and Higgs bosons than the anomalous couplings with the charm quark. In this case there is not a big difference between the distributions of an anomalous coupling with the gluon and the distributions of an anomalous coupling with the Higgs boson. This can be seen by comparing the distributions of a gut and Hut coupling as well as comparing the distributions of a gct and Hct coupling. There are also some differences between the distributions of the transverse momentum although they are not so big as in the case of the tγ process.

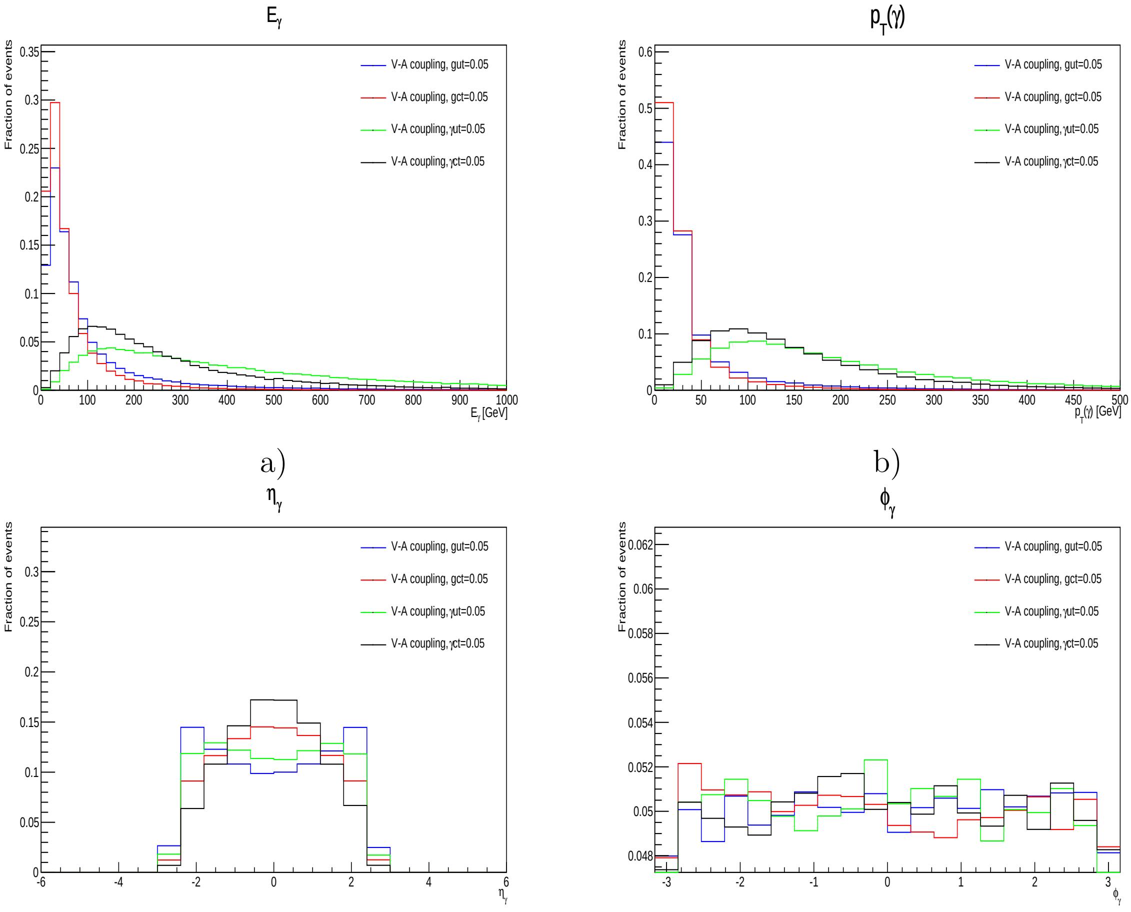

a)

b)

c)

d)

Figure 5.2: Distributions of the photon energy , p_T, η and ϕ for different coupling natures in $t\gamma$ processes. Here the anomalous couplings ζ_{ut}^L, ζ_{ct}^L , λ_{ut}^L and λ_{ct}^L take the value 0.05. The distributions are shown in a) and b) respectively.

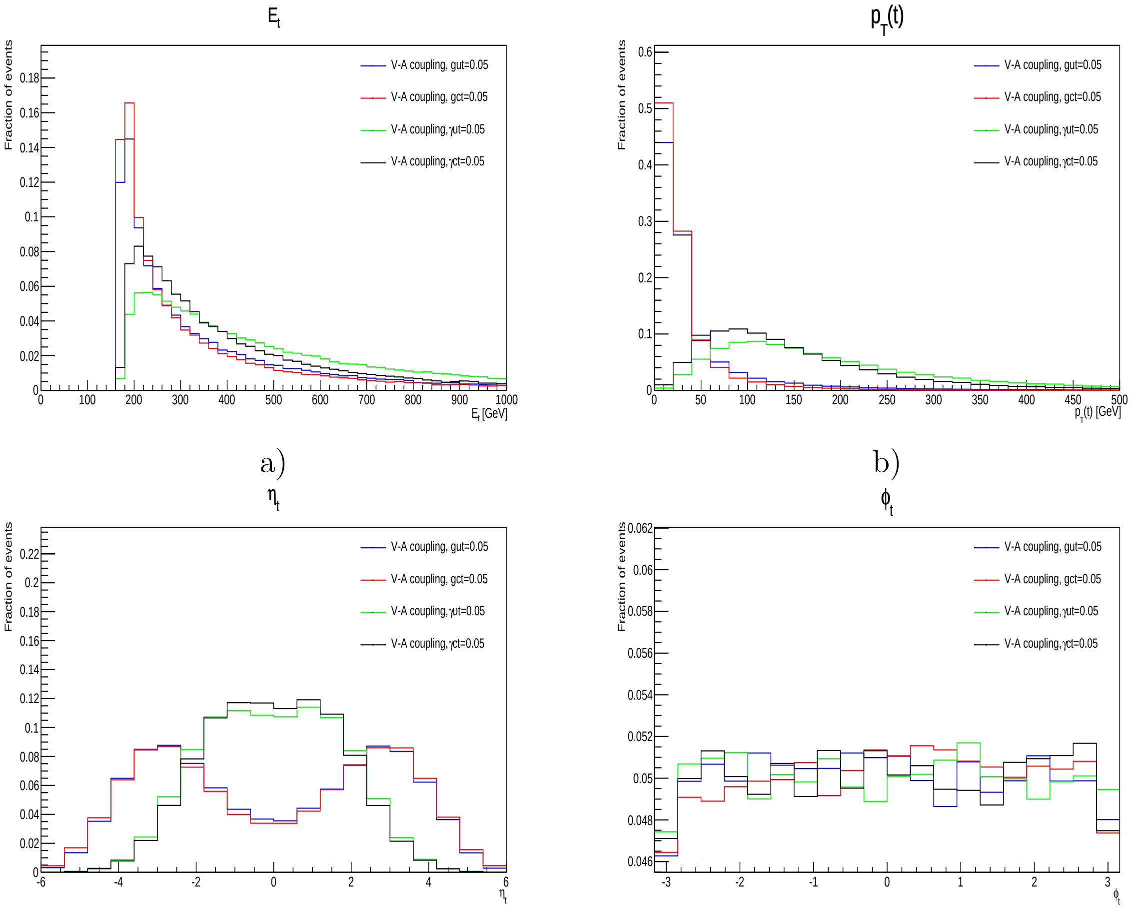

a) b)

c) d)

Figure 5.3: Distributions of the top energy , p_T, η and ϕ for different coupling natures in $t\gamma$ processes. Here the anomalous couplings ζ^L_{ut}, ζ^L_{ct} , λ^L_{ut} and λ^L_{ct} take the value 0.05. The distributions are shown in a) and b) respectively.

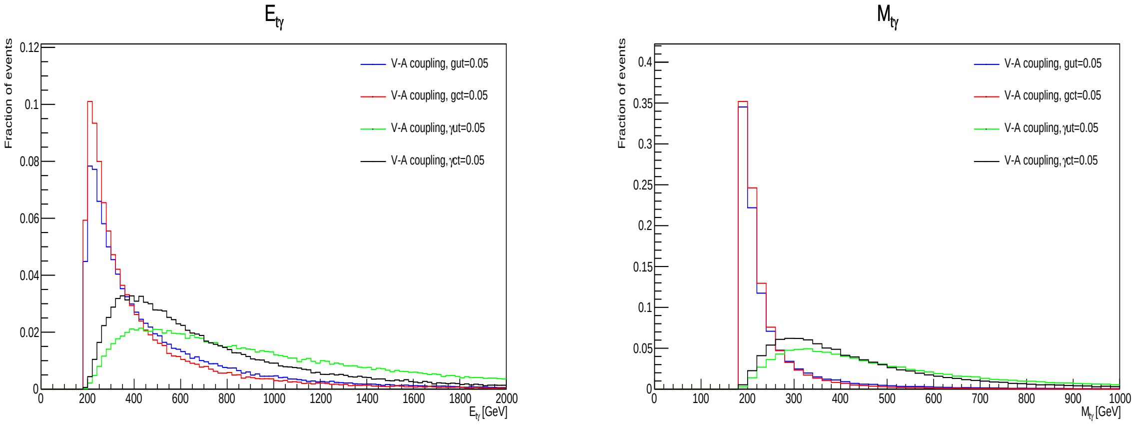

a) b)

Figure 5.4: Distributions of the $t\gamma$ system energy and mass for different coupling natures in $t\gamma$ processes. Here the anomalous couplings ζ^L_{ut}, ζ^L_{ct} , λ^L_{ut} and λ^L_{ct} take the value 0.05. The distributions are shown in a) and b) respectively.

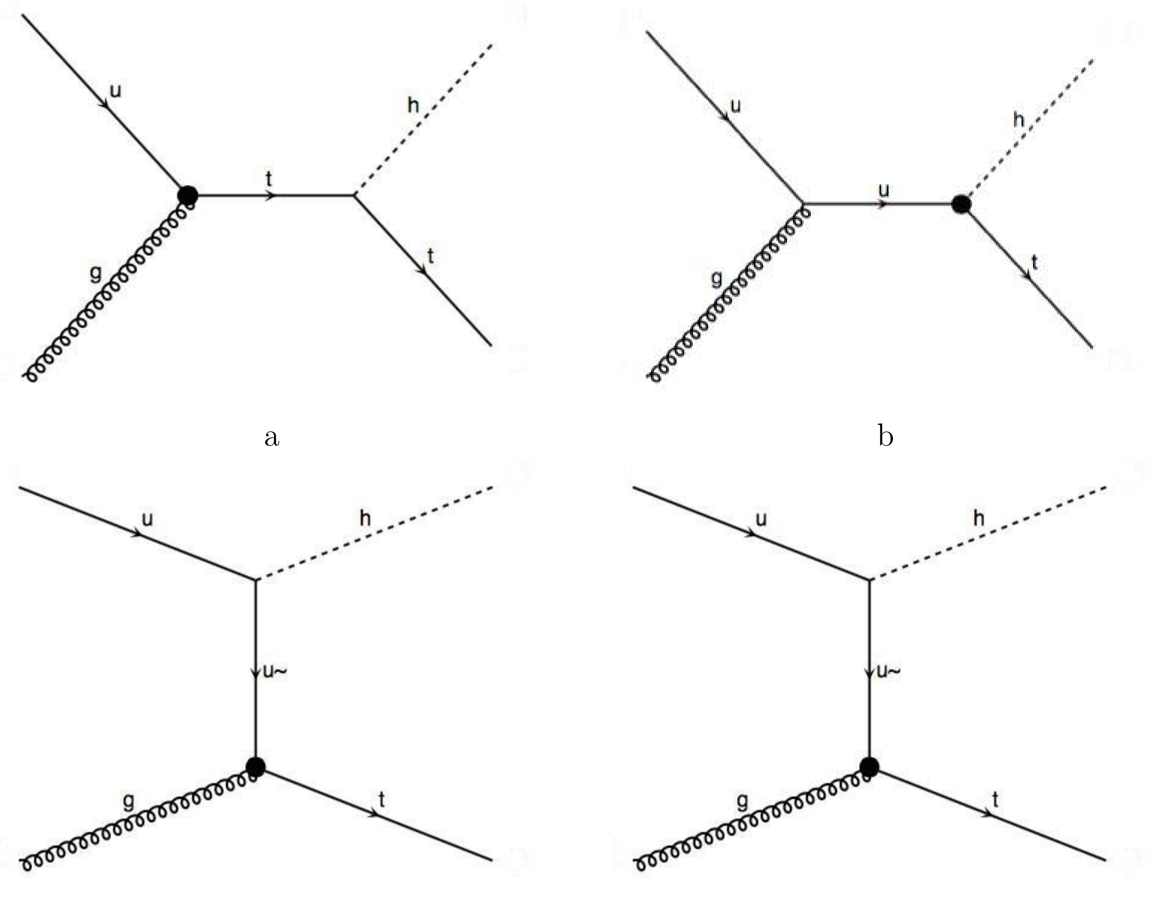

a b

c d

Figure 5.5: Feynman diagrams for tH production involving couplings with an up quark. Diagrams a) and b) are the s-channel diagrams while c) and d) are the t-channel diagrams. Diagrams with a charm quark are analogous to these ones.

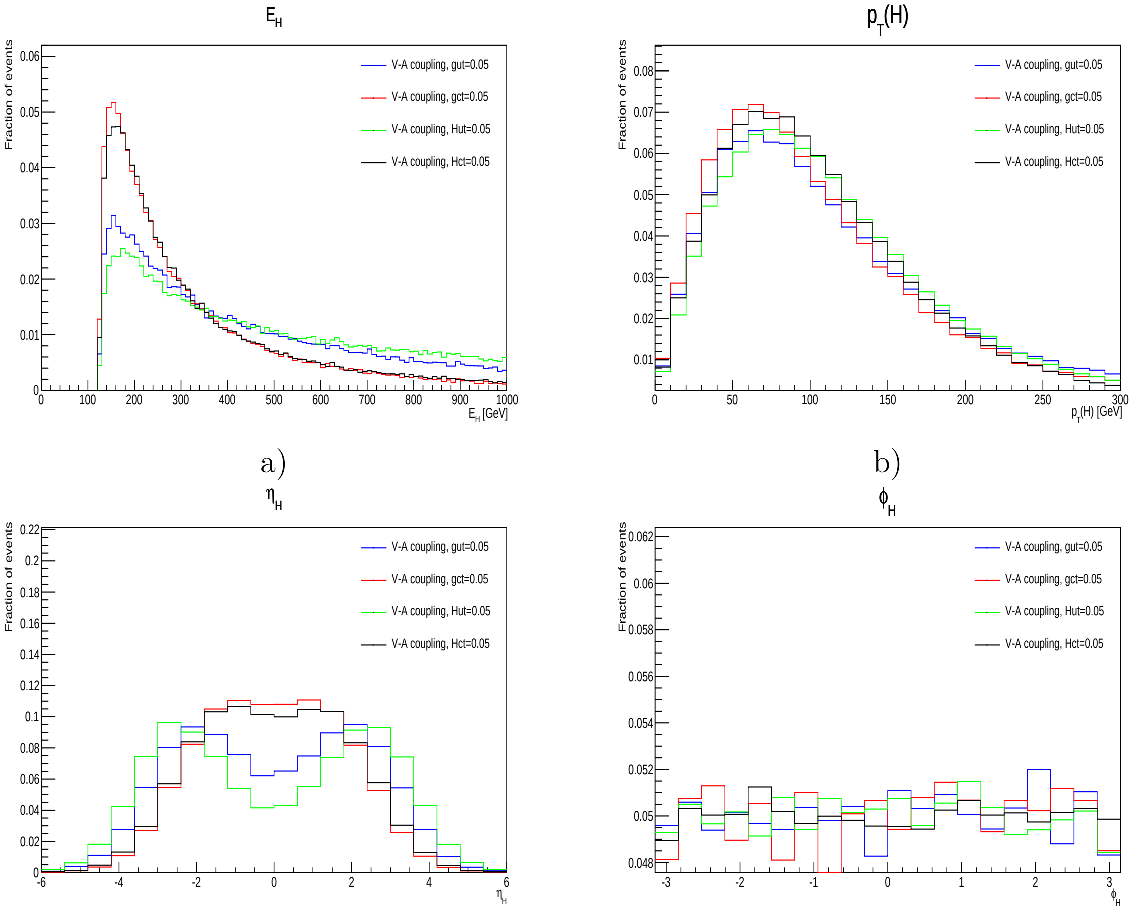

a) b)

c) d)

Figure 5.6: Distributions of the Higgs boson energy , p_T, η and ϕ for different coupling natures in tH processes. Here the anomalous couplings ζ^L_{ut}, ζ^L_{ct} , η^L_{ut} and η^L_{ct} take the value 0.05. The distributions are shown in a), b) , c) and d) respectively.

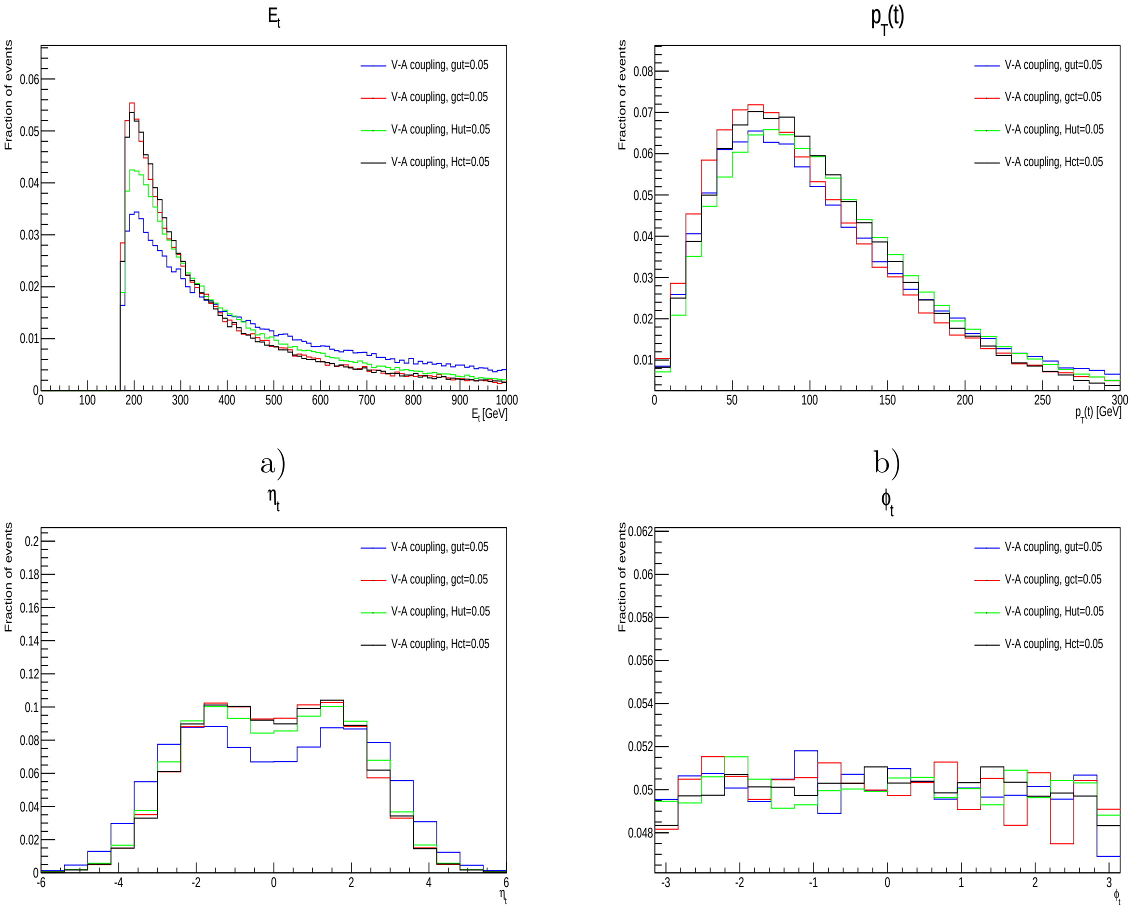

a) b)

c) d)

Figure 5.7: Distributions of the top quark energy , p_T, η and ϕ for different coupling natures in tH processes. Here the anomalous couplings ζ^L_{ut}, ζ^L_{ct} , η^L_{ut} and η^L_{ct} take the value 0.05. The distributions are shown in a), b) , c) and d) respectively.

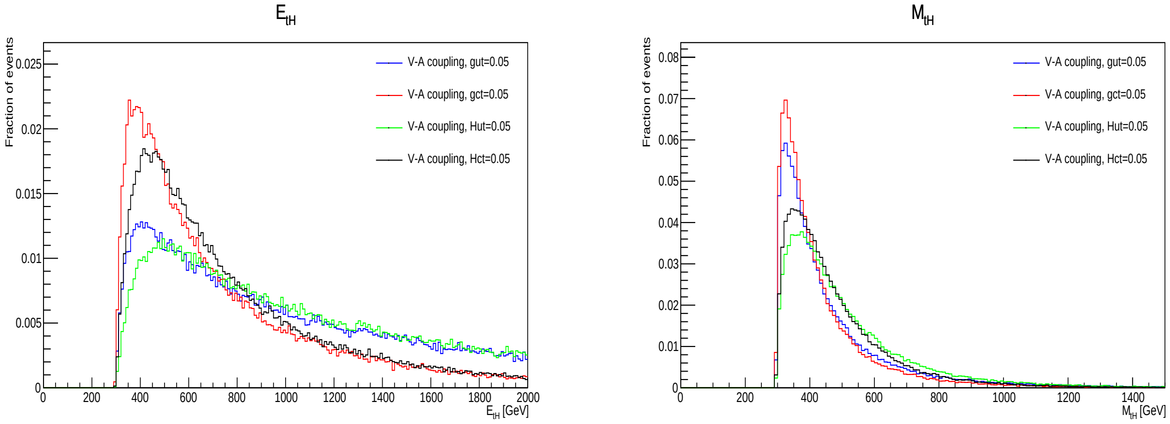

a) b)

Figure 5.8: Distributions of the tH system energy and mass for different coupling natures in tH processes. Here the anomalous couplings ζ^L_{ut}, ζ^L_{ct} , η^L_{ut} and η^L_{ct} take the value 0.05. The distributions are shown in a) and b) respectively.

5.4 tZ Analysis

In the tZ process we did not only performed studies on the top quark, Z boson and the tZ system but also on its multileptonic channel. We are also interested in the sensibility of the LHC to these processes. In this section we will explain our analysis as well as present the obtained results.

5.4.1 Sample generation

We generated both parton-level and reconstruction-level samples of tZ events in the multileptonic channel with MadGraph. In the reconstruction-level samples hadronization and detector simulation was done respectively by Pythia6.4 and by Delphes using a card that is included within the Delphes framework. The search for tZ production by CMS [19] will be used as cross-check of our work. For this reason we generated tZ samples at $\sqrt{s} = 7$ TeV and at $\sqrt{s} = 13$ TeV. The PDF set used for the generation was NN23LO1 [87]. From now on we will only consider tensor anomalous couplings to the Z boson. i.e we will not consider the terms $\bar{q}\gamma^\mu(X^L_{qt}P_L + X^R_{qt}P_R P_R)tZ_\mu$ in the tZ production. The reason for such a choice is that we want to compare our results with CMS at $\sqrt{s} = 7$ TeV with integrated luminosity of 5 fb^{-1} and they only consider tensor couplings with the Z boson.

To the sensibility study we also generated samples of WW,WZ and ZZ at NLO in the fully leptonic decay modes with MadGraph using the PDF set NN23NLO [88]. Hadronization and detector simulation were performed with Herwig6 and Delphes loaded with the CMS card. At $\sqrt{s} = 7$ TeV the corresponding cross-sections computed by MadGraph are 4.68, 0.6 and 0.06 pb while the corresponding cross-sections at $\sqrt{s} = 13$ TeV are 11.28, 1.537 and 0.1455 pb.

5.4.2 Parton-level results

The Feynman diagrams responsible for the production of this process are shown in figure 5.5. Like the tγ and tH processes we performed studies in physical observables of the top quark, Z boson and on the system tZ and only found differences between distributions with different coupling natures but equal chiralities and coupling strengths. These results can be found on the figures 5.10, 5.11 and 5.12. This time the analysis is more complex because in the case of tZ we also have vector couplings with the Z boson. Concerning anomalous couplings with the up quark we see that the vector coupling is less likely to produce energetic Z bosons and top quarks. The energy distribution of the Z boson in the case of a gut coupling is almost the same as the same distribution in the case of a tensorial Zut coupling. In the case of the top quark it is more likely to have energetic tops in the case of the gut coupling. Again we see that anomalous coupling with the charm quark produce less energetic Z bosons and top quarks than the case of the anomalous couplings with the up quark. This comments also apply when discussing the p_T distributions of the Z boson and of the top quark where the differences are higher than the energy case.

Among all the physical observables of the decay products of tZ we focused on the transverse momentum of the quark bottom p_T^b, on the transverse momentum of the lepton that comes from the decay of the resulting W of the decay of the top $p_T^{lepton-top}$ and the cosine of the angle between the direction of the lepton that comes from the decay of the top in the top reference frame with the direction of the top in the laboratory frame.

As can be seen in figures 5.14,5.15 and 5.16 these kinematical variables are very sensitive to the chirality of the coupling. That is not the case for the top quark and Z boson. Physically this makes sense, because changing the chirality of the coupling changes the spin states of the produced top quark and Z boson. Depending on its spin state the decay products of the top quark will have different angular distributions as well different spin states. As an example if we produce a top that propagates along

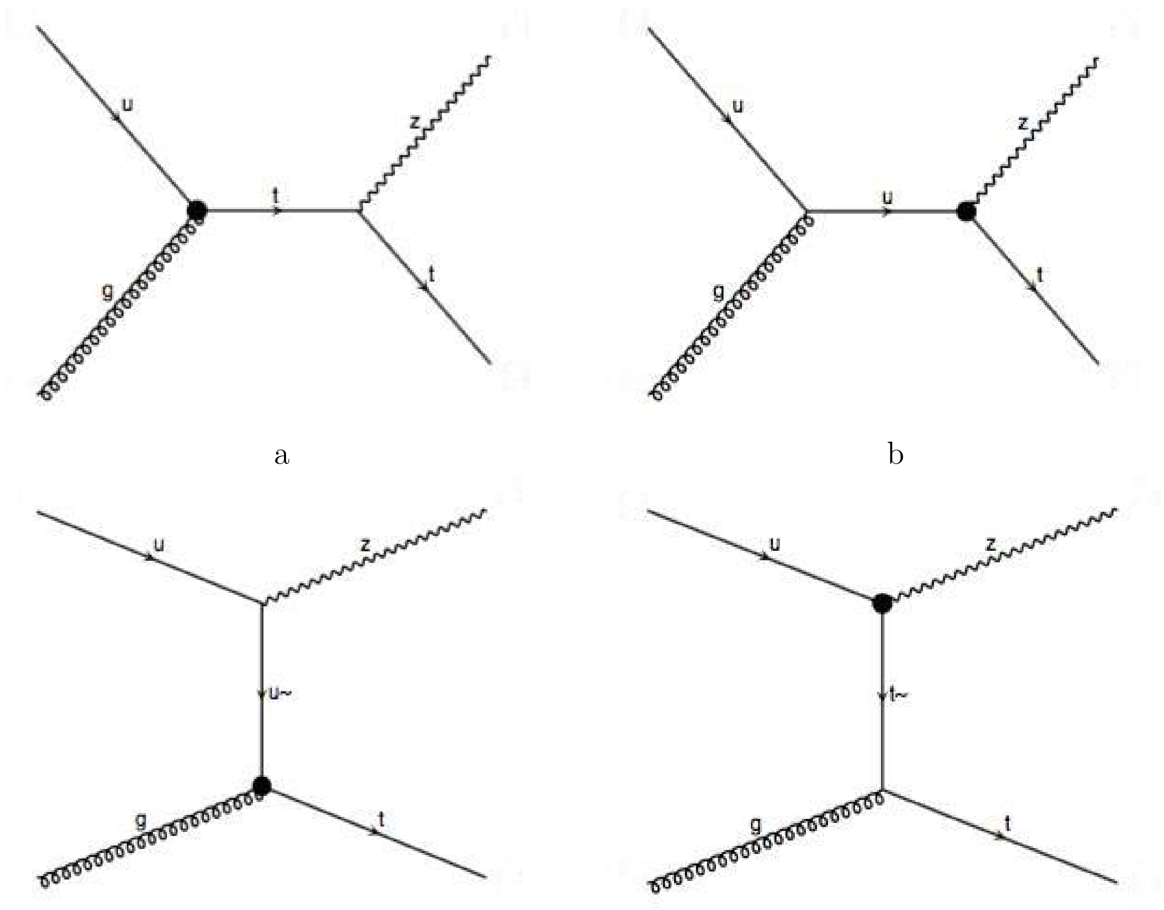

a b

c d

Figure 5.9: Feynman diagrams for tZ production involving couplings with an up quark. Diagrams a) and b) are the s-channel diagrams while c) and d) are the t-channel diagrams. Diagrams with a charm quark are analogous to these ones.

the z-axis, depending on if the top is left or right-handed, in the laboratory frame, it is possible to the W boson to be forbidden to be in +1 ou -1 spin state along the z axis. Although this happens at the parton-level it may not be the case at the detector-level because of hadronization and detector effects. If this differences are also observed at detector-level this means that the efficiencies of the signal (i.e. the ratio of events that passed through a series of cuts in an analysis by the number of expected events) may change with the chirality of the coupling. This translates in different limits in the cross-section of tZ production. Although this question is of interest by itself we also want to know if the CMS results for $\sqrt{s} = 7$ TeV and a luminosity of 5 fb^{-1} are conservative or optimistic [19]. They assume a left-handed coupling through their analysis without discussing the potential effect of the chirality in the limits. In the following sections we will describe our analysis that enabled us to answer these questions.

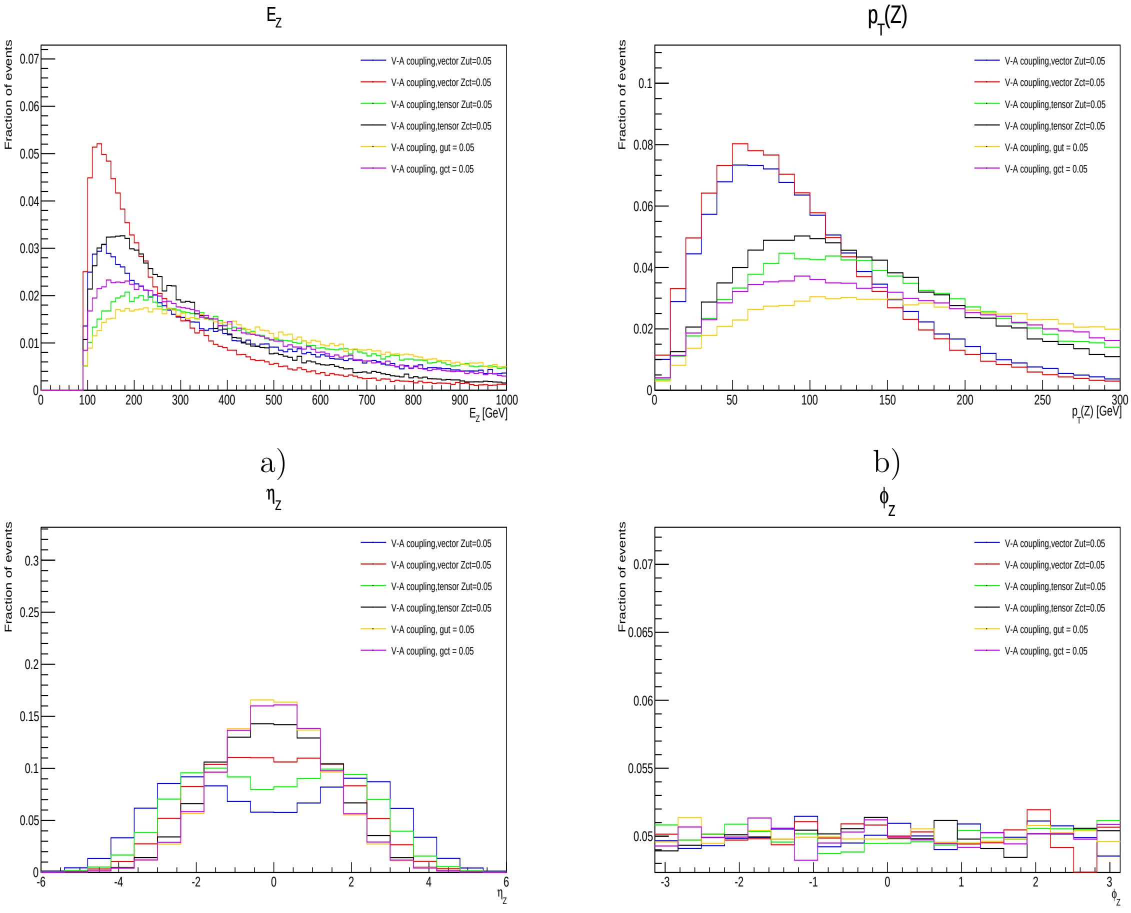

a) b) c) d)

Figure 5.10: Distributions of the Z boson energy , p_T, η and ϕ for different coupling natures in tZ processes. Here the anomalous couplings ζ^L_{ut}, ζ^L_{ct} , X^L_{ut}, X^L_{ct}, K^L_{ut} and K^L_{ct} take the value 0.05. The distributions are shown in a), b) , c) and d) respectively.

5.4.3 Physics Objects Definition

The primary objects used in this analysis are electrons, muons, missing transverse energy due to a neutrino and hadronic jets, including jets that have been tagged for the presence of a b hadron, also known as b-tagged jets.

From the simulated electrons in the detector only the ones with $p_T > 20$ GeV and $|\eta| < 2.4$ are considered while muons must satisfy $p_T > 20$ GeV and $|\eta| < 2.5$. Also only jets with $p_T > 30$ GeV and $|\eta| < 2.5$ will be considered as signal jets.

Because of the presence of a neutrino signal events it is expected a high value of missing transverse energy. The $\vec{E}_T$ is computed as refered in section 4.5.

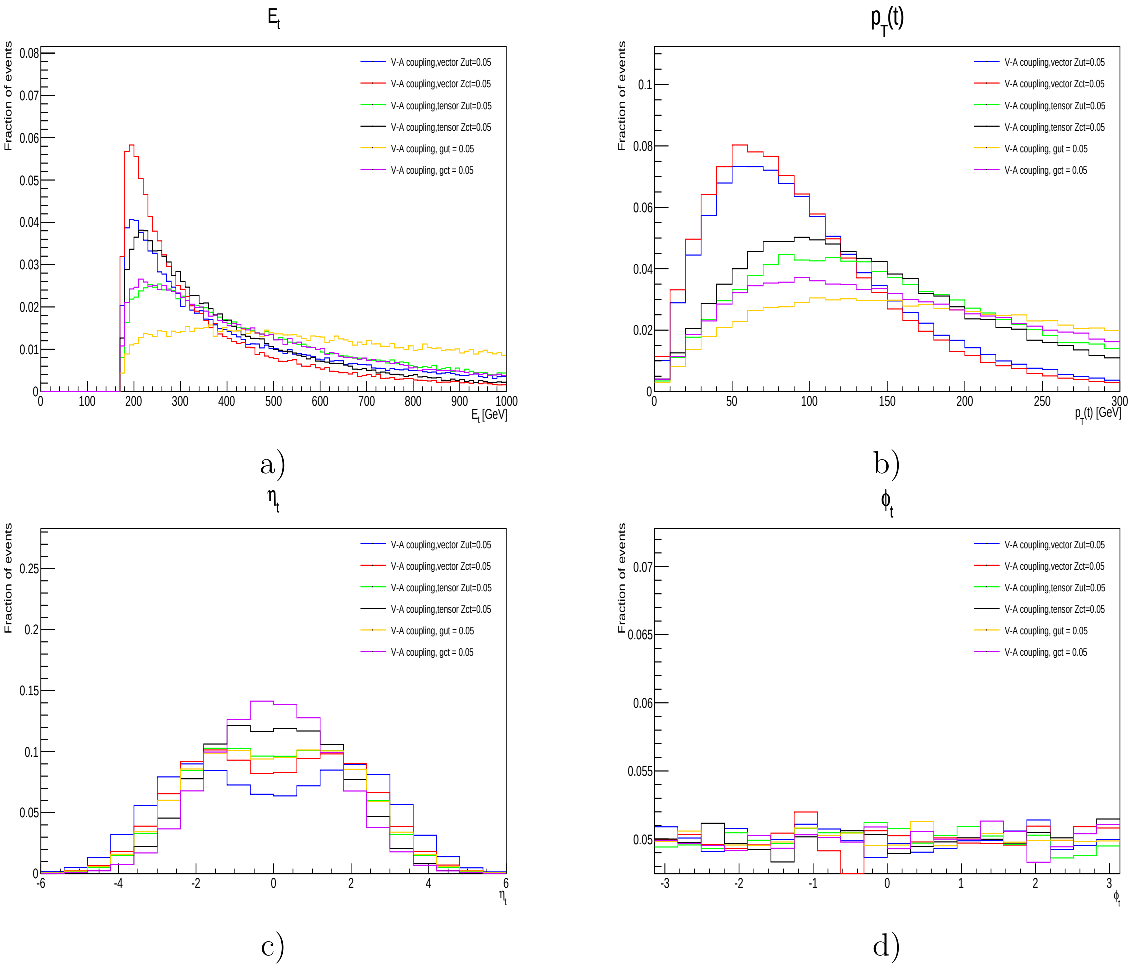

a) b) c) d)

Figure 5.11: Distributions of the top quark energy , p_T, η and ϕ for different coupling natures in tZ processes. Here the anomalous couplings ζ^L_{ut}, ζ^L_{ct} , X^L_{ut}, X^L_{ct} , K^L_{ut} and K^L_{ct} take the value 0.05. The distributions are shown in a), b) , c) and d) respectively.

5.4.4 Event Selection

In each event we look for two leptons coming from a Z boson, one b-tagged jet, a W boson from the decay of a top-quark. The leptons can be either electrons or muons and are allowed to come from the decay of a tau. Since the W boson also decays leptonically it also expected a third lepton as well a neutrino in the form of missing transverse energy.

Events with exactly three leptons with a transverse momentum,p_T, greater than 20 GeV and with pseudorapidity $|\eta| < 2.4$ for muons and $|\eta| < 2.5$ for electrons are selected. From these three leptons we have three Z boson candidates reconstructed from pairs of leptons with the same flavour but with opposite charge. The candidate with the mass closest to the Z mass is taken as the Z boson. Events with a Z boson

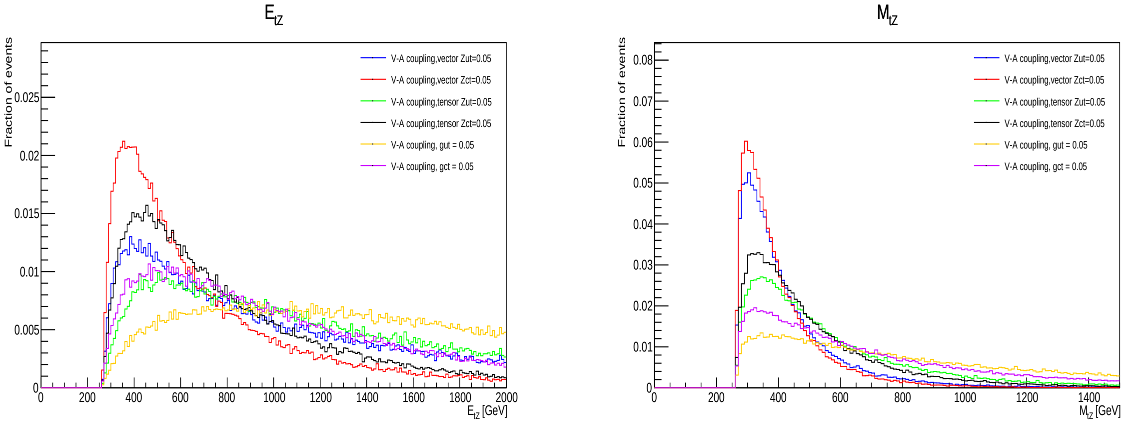

a) b)

Figure 5.12: Distributions of the tZ system energy and mass for different coupling natures in tZ processes. Here the anomalous couplings ζ^L_{ut}, ζ^L_{ct} , X^L_{ut}, X^L_{ct} , K^L_{ut} and K^L_{ct} take the value 0.05. The distributions are shown in a), b) , c) and d) respectively.

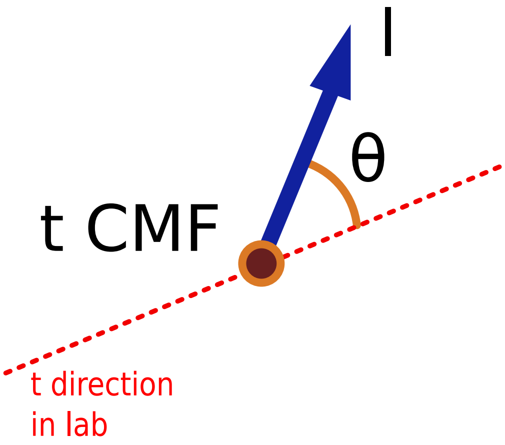

Figure 5.13: The blue arrow is the momentum of the lepton that results from the decay of the W boson in the reference frame in which the top is at rest. θ is the angle between the momentum of this lepton with the direction of the top in the laboratory reference frame.

mass not lying within 76 and 106 GeV are excluded. The remaining lepton is assumed to be the lepton that comes from the decay of the W boson.

Turning to jets, only the ones with $p_T > 30$ GeV and $|\eta| < 2.5$ are considered. If from these selected jets there are more than 1 b-tagged jet the event is vetoed. If there is exactly one b-tagged jet among the selected jets it is taken as the jet coming from the decay of the quark top. If there are no b-tagged jets the jet with the highest p_T is taken as the b-tagged jet.

The $\not{p}_x$ and $\not{p}_y$ component of the missing transverse energy are associated with the neutrino four-vector components $p_{x\nu}$ and $p_{y\nu}$. The longitudinal component is determined ,with a quadratic ambiguity, by constraining the W mass to its on-shell value

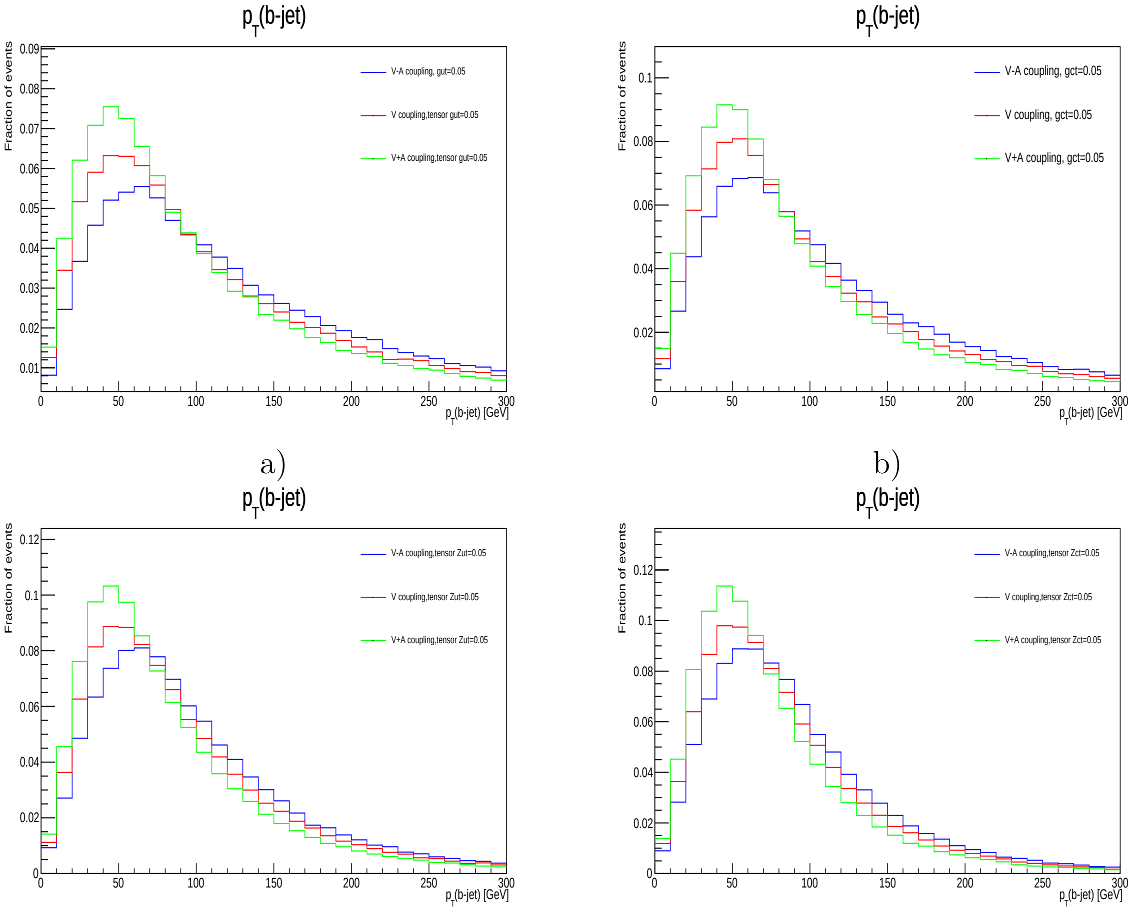

a) b) c) d)

Figure 5.14: Comparison of the p_T distributions of the b quark from samples with different chirality but with the same coupling nature and copling strength. The results for a gut, gct, Zut and Zct coupling are the ones found in a), b), c) and d) respectively

$m_W = 80.385$:

$$p_{z\nu} = \frac{-b \pm \sqrt{b^2 - 4ac}}{2a} \tag{5.1}$$

$$a = (\frac{p_{zl}}{p_l})^2 - 1 \tag{5.2}$$

$$b = 2(\frac{p_{xl}\not{p}_x + p_{yl}\not{p}_y}{p_l} + \frac{m_W^2}{2p_l})\frac{p_{zl}}{p_l} \tag{5.3}$$

$$c = (\frac{p_{xl}\not{p}_x + p_{yl}\not{p}_y}{p_l} + \frac{m_W^2}{2p_l})^2 - \not{p}_T^2 \tag{5.4}$$

Events with $b^2 - 4ac$ are rejected. The ambiguity is solved by reconstructing the top quark. With two possible values for $p_{z\nu}$ we will have two W boson candidates. Because we already defined the b-tagged jet that comes from the decay of the top, we will also

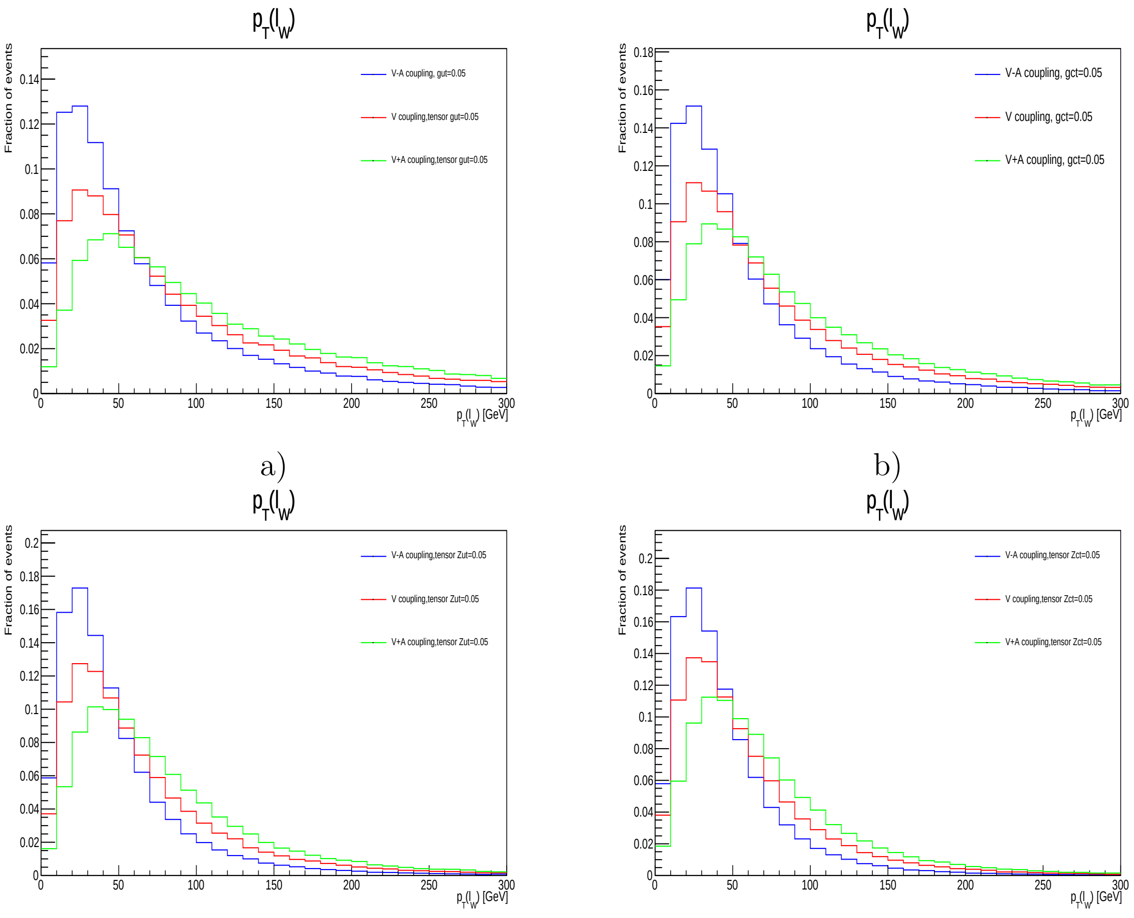

a) b)

c) d)

Figure 5.15: Comparison of the p_T distributions of the lepton that comes from the W decay from samples with different chirality but with the same coupling nature and coupling strength. The results for a gut, gct, Zut and Zct coupling are the ones found in a), b), c) and d) respectively

have two top quark candidates. We choose the $p_{z\nu}$ value whose top quark candidate has the mass closest to 172 GeV.

One final cut is made on the transverse mass of the W boson m_T^W. This observable is computed with the lepton that is associated with the W boson and with the missing transverse energy by

$$m_T^W = \sqrt{(E_T^{l_W} + \not{E}_T)^2 - (p_{xl} + \not{p}_x)^2 - (p_{yl} + \not{p}_y)^2} \tag{5.5}$$

Events with $m_T^W < 20$ GeV are rejected.

In table 5.1 we reproduce the results obtained by CMS in their search for tZ at $\sqrt{s} =$ 7 Tev with a luminosity of 5 fb^{-1}. Our results at $\sqrt{s} = 7$ Tev with a luminosity of 5 fb^{-1}. are presented in 5.2. Our number of events that pass through all cuts differs no

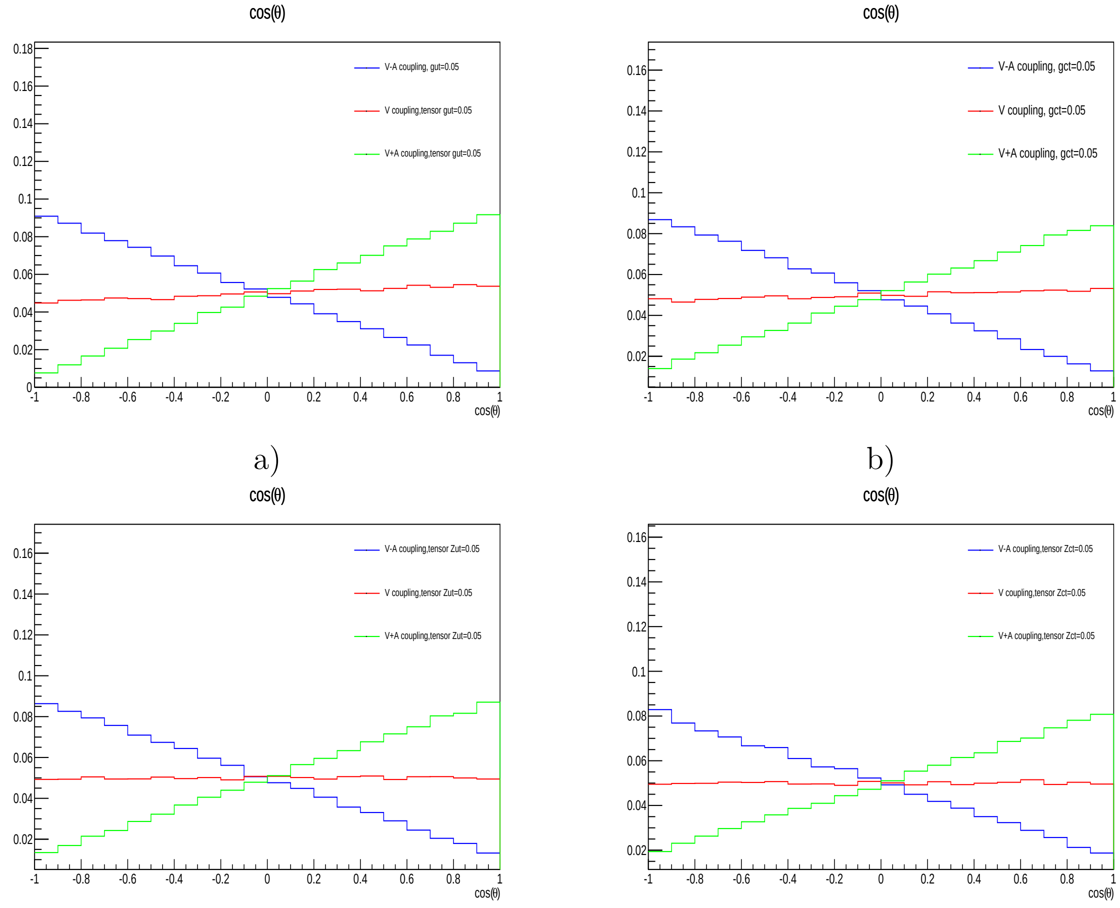

a)

b)

c)

d)

Figure 5.16: Comparison of the $\cos\theta$ from samples with different chirality but with the same coupling nature and coupling strength. The results for a gut, gct, Zut and Zct coupling are the ones found in a), b), c) and d) respectively

more than 20 % than the corresponding numbers of CMS. For a centre-of-mass energy of 13 TeV and a luminosity of 10 fb^{-1} we obtained the results presented in table 5.3. We also confirmed that left-handed and right-handed anomalous couplings reproduce different distributions for p_T^{b-jet}, $p_T^{l_W}$ and $\cos\theta$ at the detector-level as is show in figures 5.17, 5.18 and 5.19. After this event selection we perform a Multivariate Analysis on the samples of the events that passed all these cuts. The description of the Multivariate Analysis is the topic of the following section.

Cut	signal(0.1 pb)	Diboson
lepton selection	98.6	775.9
Z mass cut	89.7	471.1
jet multiplicity	78.6	197.6
b-jet multiplicity	73.8	179.3
m_T^W	62.4	157.1

Table 5.1: Event yield after the different steps of the event selection by CMS assuming that tZ is produced through an anomalous gut coupling. The signal corresponds to an anomalous gut coupling and is rescaled to a cross-section of 0.1 pb. Adapted from [19]

Cut	signal(0.1 pb)	Diboson
lepton selection	116.314	775.9
Z mass cut	112.693	754.194
jet multiplicity	102.363	274.236
b-jet multiplicity	101.883	274.208
m_T^W	71.4	182.38

Table 5.2: Event yield after the different steps of the event selection using our generated samples at $\sqrt{s} = 7$ TeV with a luminosity of 5 fb^{-1}. The signal corresponds to an anomalous gut coupling and is rescaled to a cross-section of 0.1 pb

Cut	signal(0.1 pb)	Diboson
lepton selection	157.775	3222.441
Z mass cut	152.720	3128.345
jet multiplicity	138.480	1393.655
b-jet multiplicity	137.645	1393.092
m_T^W	94.830	922.067

Table 5.3: Event yield after the different steps of the event selection for samples generated at $\sqrt{s} = 13$ TeV with a luminosity of 10 fb^{-1}. The signal corresponds to an anomalous gut coupling and is rescaled to a cross-section of 0.1 pb.

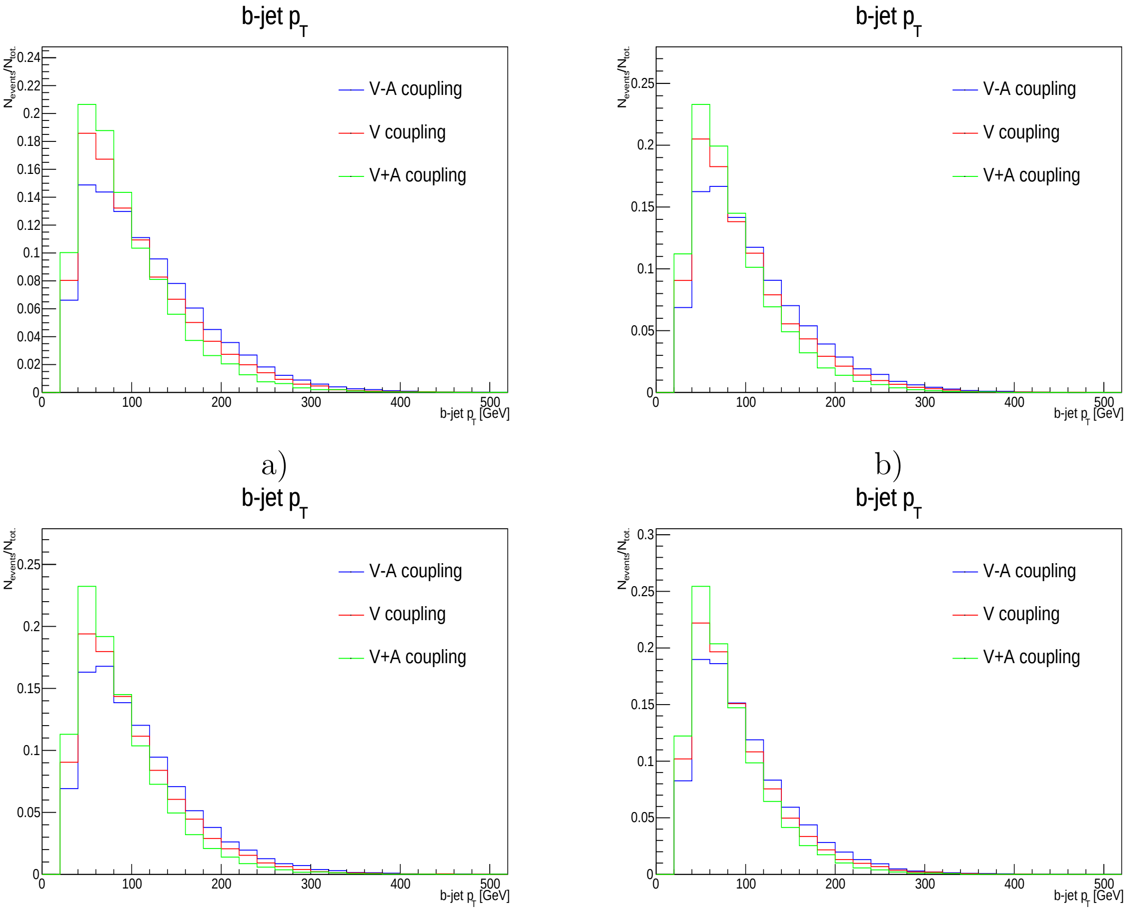

a) b)

c) d)

Figure 5.17: Distributions of the p_T of the b-jet candidate. a), b) , c) and d) are the corresponding distributions for gut, gct, Zut and Zct anomalous couplings.

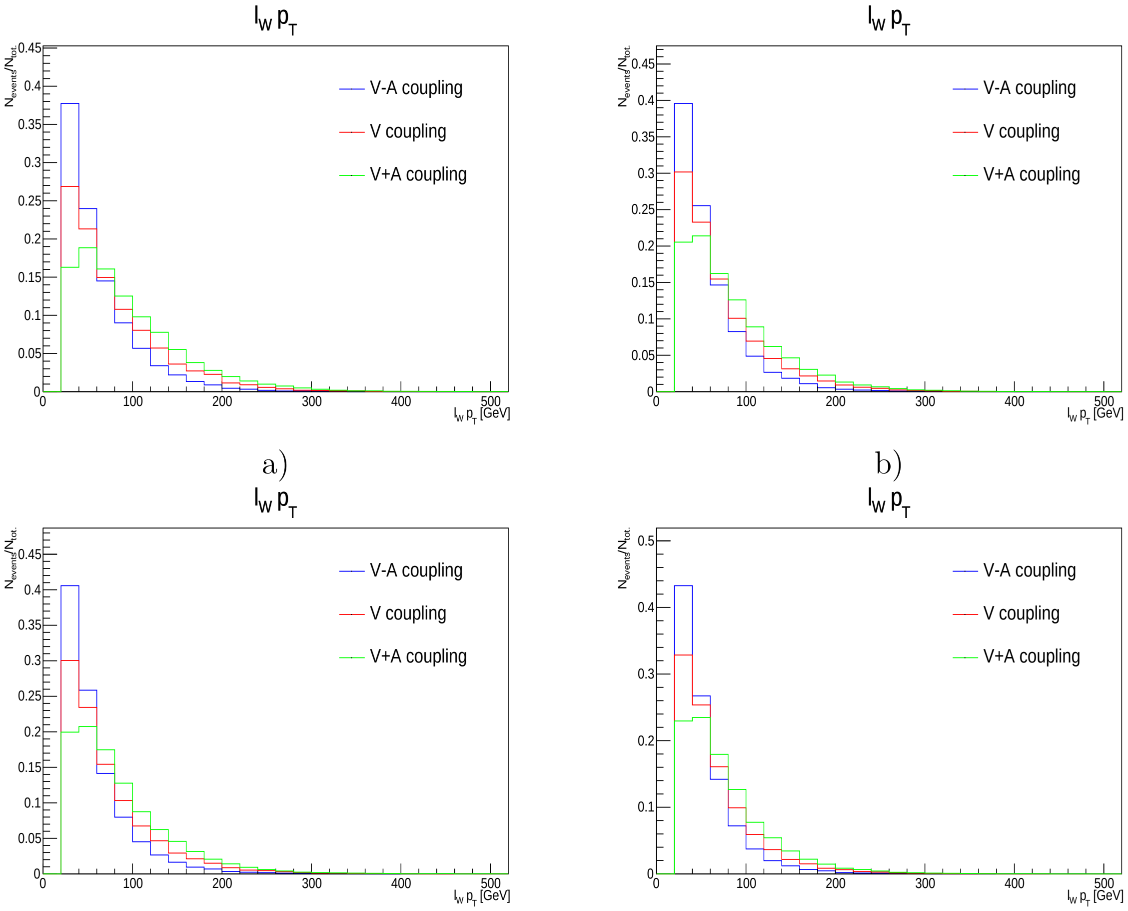

a)

b)

c)

d)

Figure 5.18: Distributions of the p_T of the lepton resulting from the decay of the W candidate. a), b) , c) and d) are the corresponding distributions for gut, gct, Zut and Zct anomalous couplings.

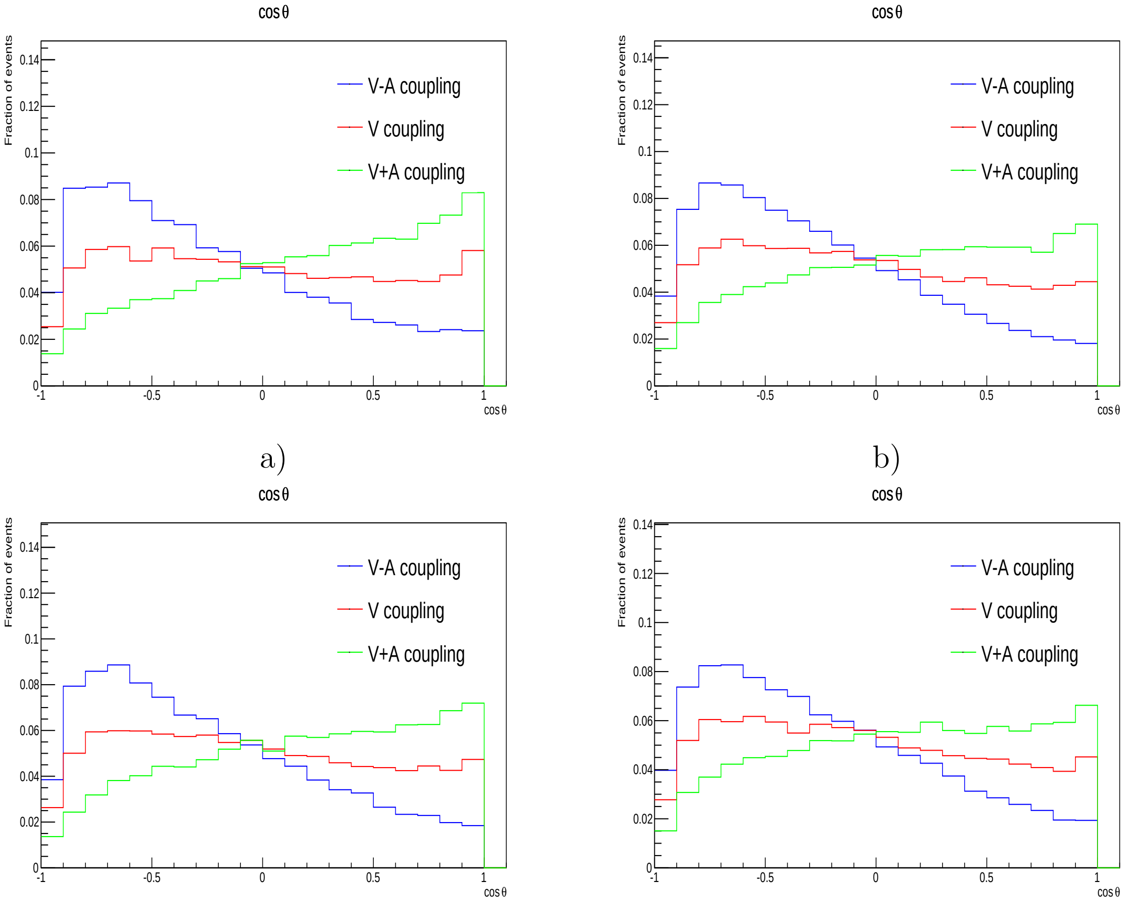

a)

b)

c)

d)

Figure 5.19: Distributions of $\cos\theta$, where θ is the angle between the direction of the lepton from the W candidate in the top rest frame with the direction of the top in the laboratory reference frame. a), b) , c) and d) are the corresponding distributions for gut, gct, Zut and Zct anomalous couplings.

Chapter 6

Multivariate Analysis

In this chapter we will describe the Multivariate Analysis using Boosted Decision Trees (BDTs) employed in the study of tZ production. This chapter is divided as follows: in section 6.1 we explain the concept of a BDT; in section 6.2 we talk about the input variables given; section 6.3 explains how the training and test of the BDTs was done; finally in section 6.4. Both the training/test phase and application phases were performed using the software Toolkit for Multivariate Analysis (TMVA) [89].

6.1 Multivariate Analysis with Boosted Decision Trees

As we saw in section 2.5 a FCNC process in the Standard Model is an extremely rare event. On the other hand at high centre-of-mass energy collisions at high luminosity produce huge data sets. It is then mandatory to extract as much relevant information as possible from the data. This difficulty can be surpassed by applying a Multivariate Analysis (MVA). In a MVA we employ variables that potentially discriminate the signal events from the background events as input for multivariate classifiers. These multivariate classifiers usually produce an output that we can apply cuts in order to achieve a greater ratio between signal and background. The MVA methods have the advantage that results can be improved without the need to apply cuts that continuously decrease statistics of both signal and background.

In this work only one multivariate classifier was used, a *Boosted Decision Tree* (BDT).

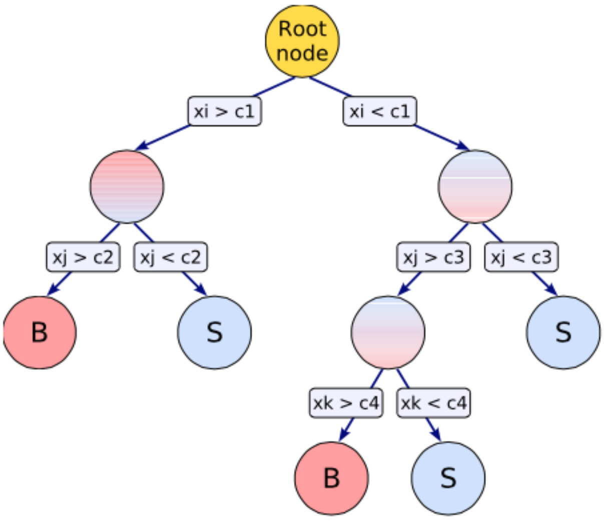

Figure 6.1: Schematic view of a decision tree. Starting from the root node, a sequence of binary splits using the discriminating variables xi is applied to the data. Each split uses the variable that at this node gives the best separation between signal and background when being cut on. The same variable may thus be used at several nodes, while others might not be used at all. The leaf nodes at the bottom end of the tree are labeled “S” for signal and “B” for background depending on the majority of events that end up in the respective nodes. Extracted from [89]

As can be seen in figure 6.1 a BDT is a sequence of left/right (yes/no) decisions based on the value of a given variable at the time until a stop criterion is fulfilled. The phase space of these variables is then separated in regions that can be labeled as signal or background, depending on the majority of training events that end up in the final leaf mode. The BDTs are unstable since a small change in the training data can produce a large change in the tree. This is fixed by the use of boosting. For boosting, the training events which were misclassified have their weights increased, and a new tree is formed. In this new tree we apply the same procedure. This extends the concept from one tree to several trees which constitute a forest. To each event at the end of each tree is assigned a given score. The final classifier is the weighted average of all the individual scores. Boosting increases the statistical stability of the classifier trees as well the separation performance when compared with a single decision tree.

6.2 Discriminating variables used

As was mentioned in the previous section discriminating variables allow to do a better separation between signal and background without sacrificing too much the amount of statistics. The discriminant variables used to train and compute BDT output are related to reconstructed leptons, jets, Z-boson and top candidates. Above we have the list of discriminant variables. Their distributions for $\sqrt{s} = 13$ TeV and an integrated luminosity of 10 fb^{-1} are presented in figures 6.2, 6.3, 6.4 and 6.5.

- Reconstructed top mass,
- $\Delta\phi(l_W - b)$, the azimuthal angle between the lepton from the W candidate and the b-jet candidate,
- $q|\eta|$, with q and η the electric charge and the pseudorapidity of the W candidate, respectively,
- p_T of the Z boson candidate,
- η of the Z boson candidate,
- jet multiplicity,
- b-tagged jet multiplicity,
- $\Delta\phi(Z - \not{E}_T)$. the azimuthal angle between the Z candidate and the direction of the $\not{E}_T$ vector,
- η of the leading jet,
- $\Delta\phi(l_W - Z)$, the azimuthal angle between the lepton from the W candidate and the Z candidate,
- p_T of the b-jet candidate,
- p_T of the lepton from the W candidate,
- $\cos\theta$, where θ is the angle the direction of lepton from the W candidate in the top rest-frame makes with the direction of the top in the laboratory frame.

6.3 Training/testing BDTs

Separating signal from background is a classification problem: given an event we classify it as signal or as background. To do that our method must first learn how to separate signal events from background events. For this reason we must first train the BDT. We trained the BDT eight times each time we used the same WZ + jets

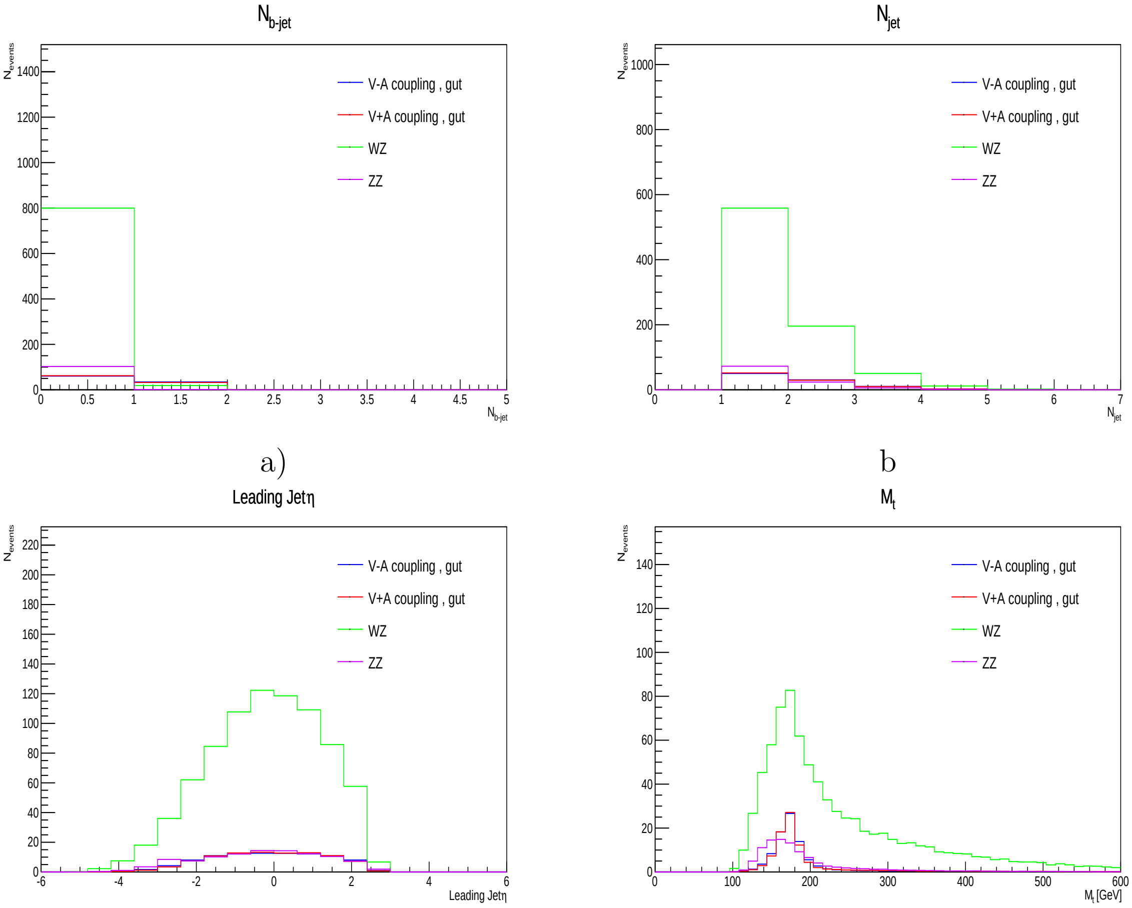

a) b c) d)

Figure 6.2: The chosen discriminant variables: (a) b-jet multiplicity, (b) jet multiplicity, (c) leading jet η and (d) reconstructed top mass after event selection (see section 5.4.4). These distributions were obtained for a centre-of-mass energy of 13 TeV and an integrated luminosity of 10 fb^{-1}

sample but a different sample. The samples differed by coupling nature and chirality since we wanted to study the sensibility of the LHC to each coupling and to see if the results depend on the chirality. The training was performed with half of the sample with events selected in a random way. The testing of the BDT was done with the remaining half of the sample. The input variables used were the discriminating variables presented in section 6.2.

In figure 6.6 we have the linear correlation coefficients between the discriminating variables for a signal sample of a left-handed gut coupling and for a WZ + jets sample. As can be seen the correlations are stronger between the angular distributions. First of all the kinematics of the particles in the event is subject to conservation of 4-momentum. Secondly the spin states of the top quark, Z boson and W bosons are a function of the coupling chirality which has an impact on the form of the

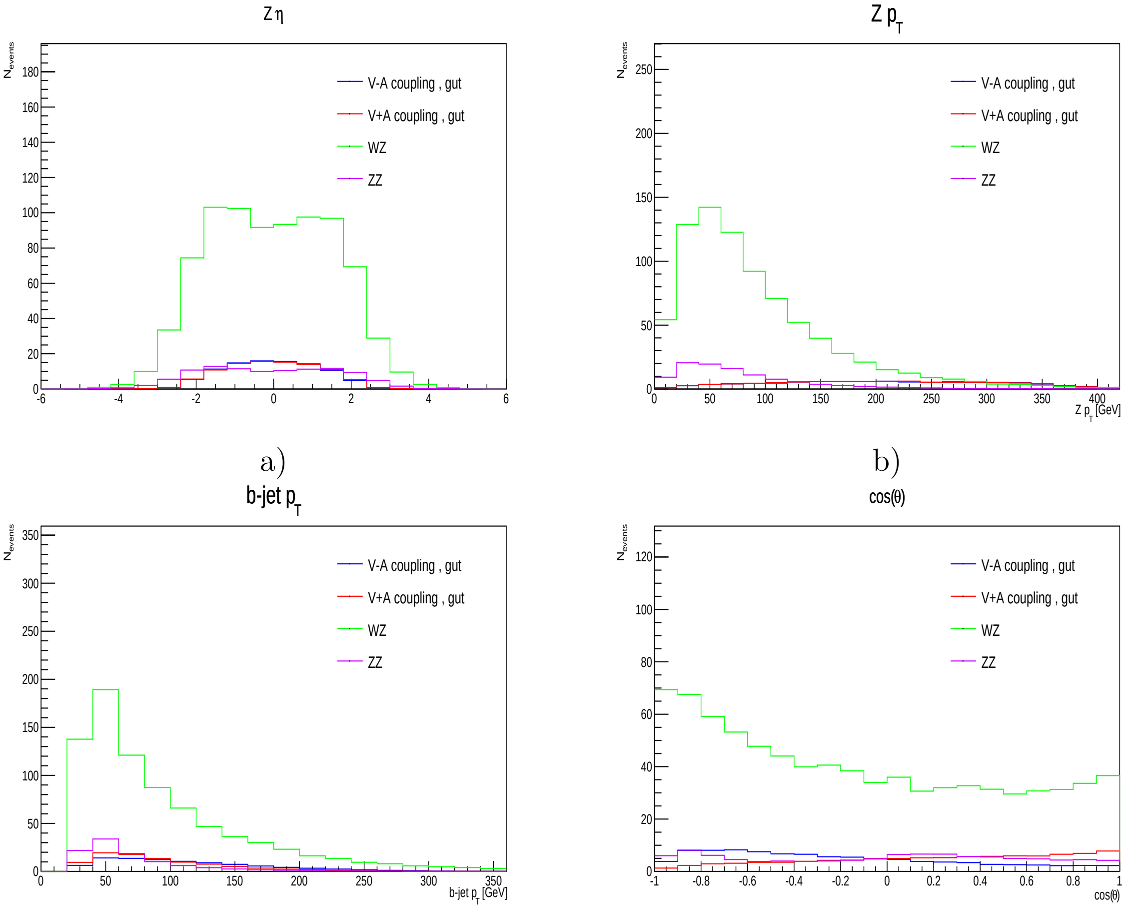

a) b) c) d)

Figure 6.3: The chosen discriminant variables: (a) Z η, (b) Z p_T, (c) b-jet p_T and (d) $\cos\theta$ after event selection (see section 5.4.4). These distributions were obtained for a centre-of-mass energy of 13 TeV and an integrated luminosity of 10 fb^{-1}

angular distributions. Note that these correlations are stronger on the signal where the spin state of the top quark is imposed by the chirality. Nevertheless the correlation coefficients are not high enough for exclusion of some variables from the analysis.

After the training and testing it is mandatory to do a performance test of the BDT. This can be done by studying the background rejection as a function of the signal efficiency (efficiency = 1 - background reduction), also known as ROC (receiver operating characteristic) curve. The ideal performance would be rejecting a lot of background while maintaining a good signal efficiency which means that the greater the area of a ROC curve the better the performance. As can be seen in figure 6.7 the BDT has a good performance. In that figure you find ROC curves for left-handed gut, gct, Zut and Zct anomalous couplings. The right-handed ROC curves are omitted because they are similar to the left-handed ones.

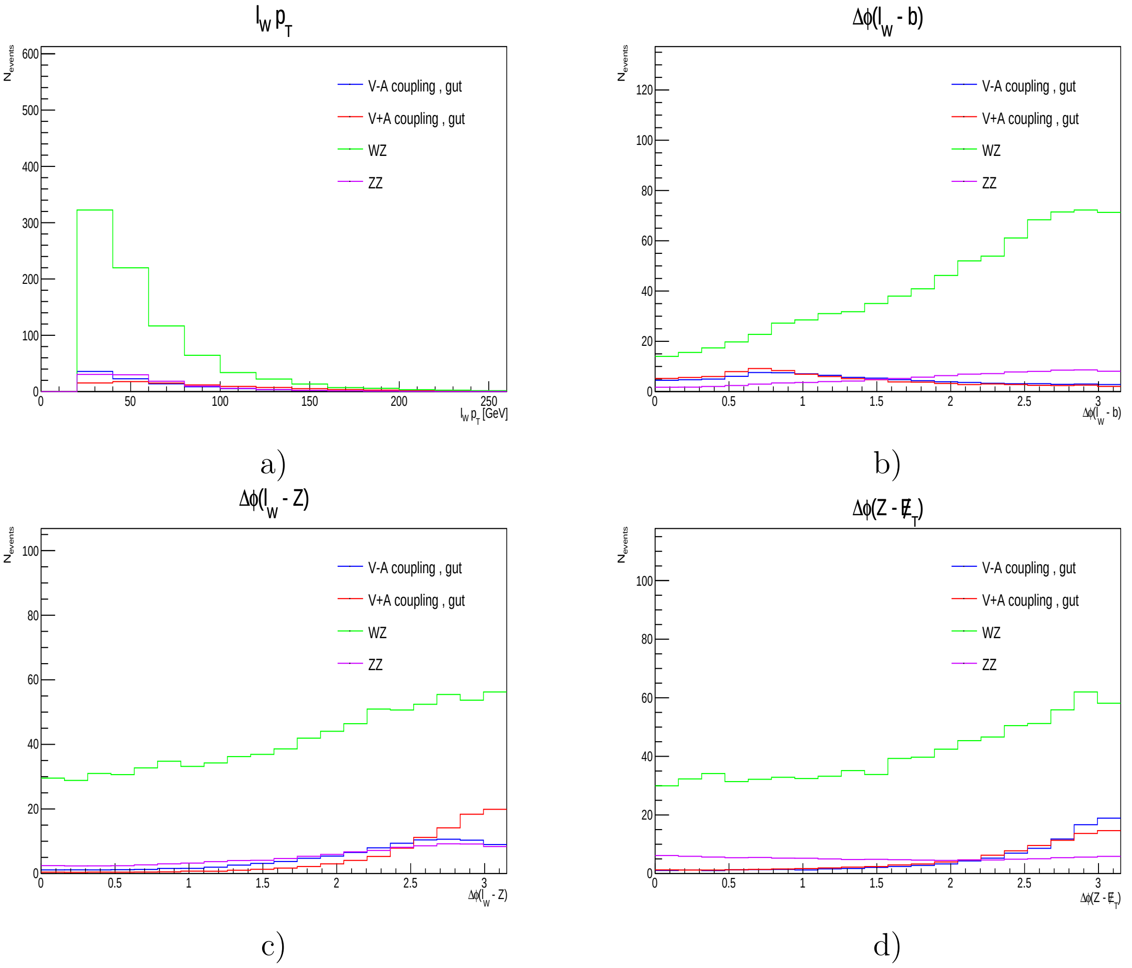

Figure 6.4: The chosen discriminant variables: (a) lepton from W candidate p_T, (b) $\Delta\phi(l_W - b - jet)$, (c) $\Delta\phi(l_W - Z)$ and (d) $\Delta\phi(Z - \not{E}_T)$ after event selection (see section 5.4.4). These distributions were obtained for a centre-of-mass energy of 13 TeV and an integrated luminosity of 10 fb^{-1}

After training we test the BDT for overtraining. We have overtraining when have very good performance on the training sample but a poorer performance in a statically independent sample. This undesirable behaviour occurs when a machine learning problem has a very small number of degrees of freedom. In particular BDTs are at least subject to partial overtraining. To train the BDT we used the default parameters of TMVA for this method [89]. To monitor overtraining the BDT output of distribution of the training samples was compared with the BDT output distribution of the test samples. The superimposed training and testing results are show in figure **??**. The distributions have similar shapes , showing no evidence of small overtraining. Now that the BDTs are trained and their performance is checked we can now focus on the application phase.

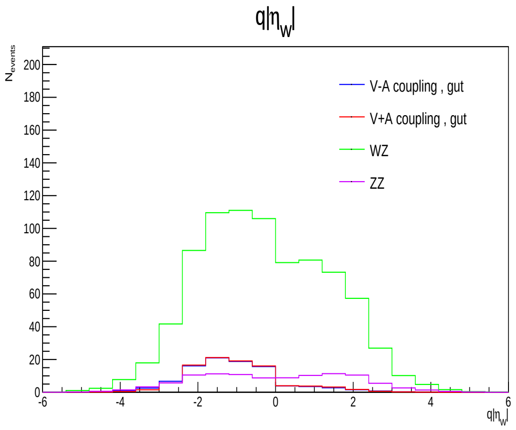

Figure 6.5: The chosen discriminant variable $q|\eta_W|$ after event selection (see section 5.4.4). These distributions were obtained for a centre-of-mass energy of 13 TeV and an integrated luminosity of 10 fb^{-1}

6.4 Applying BDT Classification

We applied the trained BDT to the same signal samples we used to train/test the BDT and to a Diboson sample containing the sample WZ+jets that was also used to train/test the BDT. In the training/testing phase one half was used to train and the other half to test. Here both halves are used. The BDT output for both the signal samples and Diboson sample are show in figure 6.9. We do not plot the outputs for right-handed couplings because the distributions are similar although not the same. Next we perform different cuts on the BDT output and perform a counting experiment in order to extract limits on the cross-section. This is the subject of the next chapter.

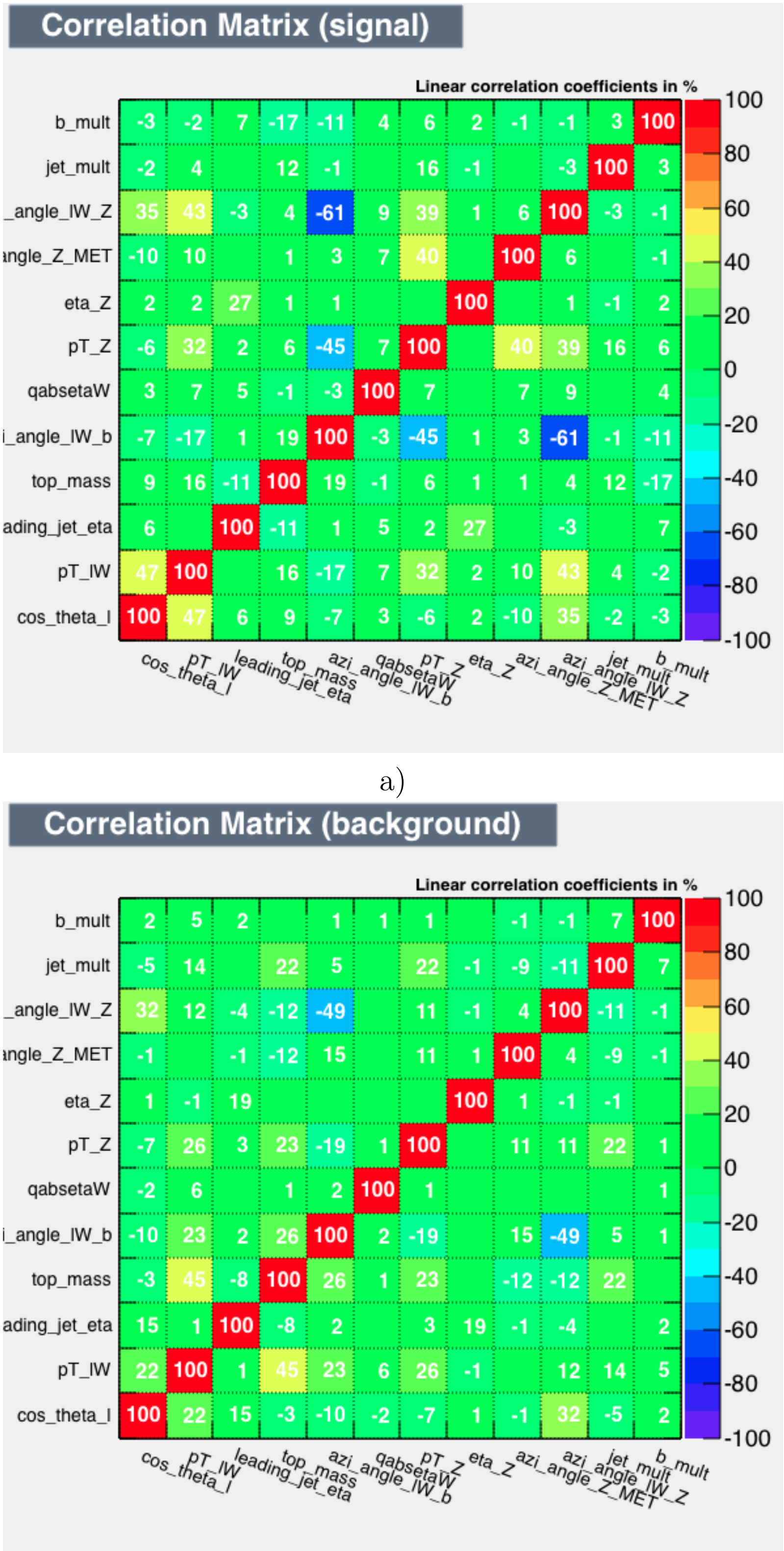

	cos_theta_l	pT_lW	leading_jet_eta	top_mass	azi_angle_lW_b	qabsetaW	pT_Z	eta_Z	azi_angle_Z_MET	azi_angle_lW_Z	jet_mult	b_mult
b_mult	-3	-2	7	-17	-11	4	6	2	-1	-1	3	100
jet_mult	-2	4		12	-1		16	-1		-3	100	3
_angle_lW_Z	35	43	-3	4	-61	9	39	1	6	100	-3	-1
ıngle_Z_MET	-10	10		1	3	7	40		100	6		-1
eta_Z	2	2	27	1	1			100		1	-1	2
pT_Z	-6	32	2	6	-45	7	100		40	39	16	6
qabsetaW	3	7	5	-1	-3	100	7		7	9		4
i_angle_lW_b	-7	-17	1	19	100	-3	-45	1	3	-61	-1	-11
top_mass	9	16	-11	100	19	-1	6	1	1	4	12	-17
ading_jet_eta	6		100	-11	1	5	2	27		-3		7
pT_lW	47	100		16	-17	7	32	2	10	43	4	-2
cos_theta_l	100	47	6	9	-7	3	-6	2	-10	35	-2	-3

a)

	cos_theta_l	pT_lW	leading_jet_eta	top_mass	azi_angle_lW_b	qabsetaW	pT_Z	eta_Z	azi_angle_Z_MET	azi_angle_lW_Z	jet_mult	b_mult
b_mult	2	5	2		1	1	1		-1	-1	7	100
jet_mult	-5	14		22	5		22	-1	-9	-11	100	7
_angle_lW_Z	32	12	-4	-12	-49		11	-1	4	100	-11	-1
ıngle_Z_MET	-1		-1	-12	15		11	1	100	4	-9	-1
eta_Z	1	-1	19					100	1	-1	-1	
pT_Z	-7	26	3	23	-19	1	100		11	11	22	1
qabsetaW	-2	6		1	2	100	1					1
i_angle_lW_b	-10	23	2	26	100	2	-19		15	-49	5	1
top_mass	-3	45	-8	100	26	1	23		-12	-12	22	
ading_jet_eta	15	1	100	-8	2		3	19	-1	-4		2
pT_lW	22	100	1	45	23	6	26	-1		12	14	5
cos_theta_l	100	22	15	-3	-10	-2	-7	1	-1	32	-5	2

b)

Figure 6.6: Linear correlation coefficients between the discriminating variables used: (a) for a tZ production through a left-handed gut coupling sample and (b) for a WZ + jets background sample. These coefficients are obtained after training (and testing) the BDT with the aforementioned samples as input.

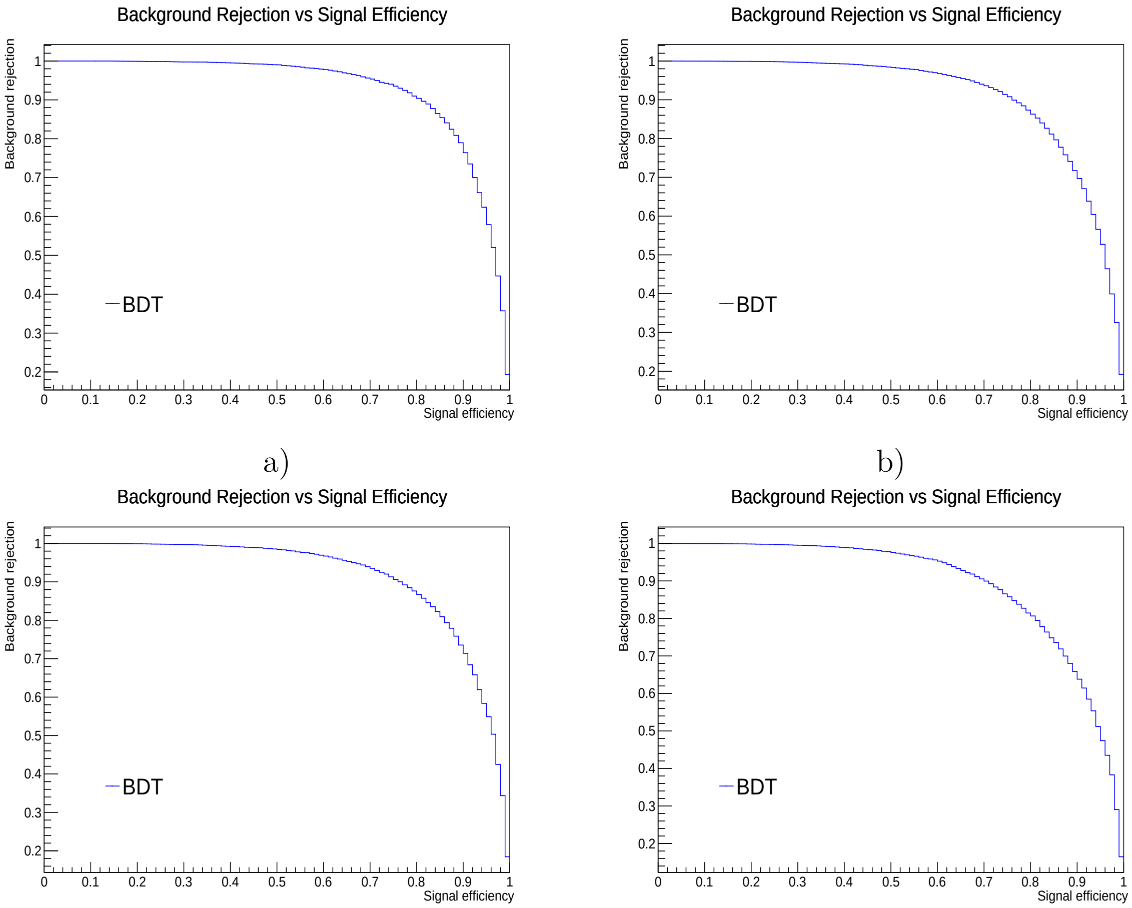

a)

b)

c)

d)

Figure 6.7: ROC curves for left-handed (a) gut, (b) gct, (c) Zut and (d) Zct anomalous couplings. As can be seen from this figure the BDT has a good performance.

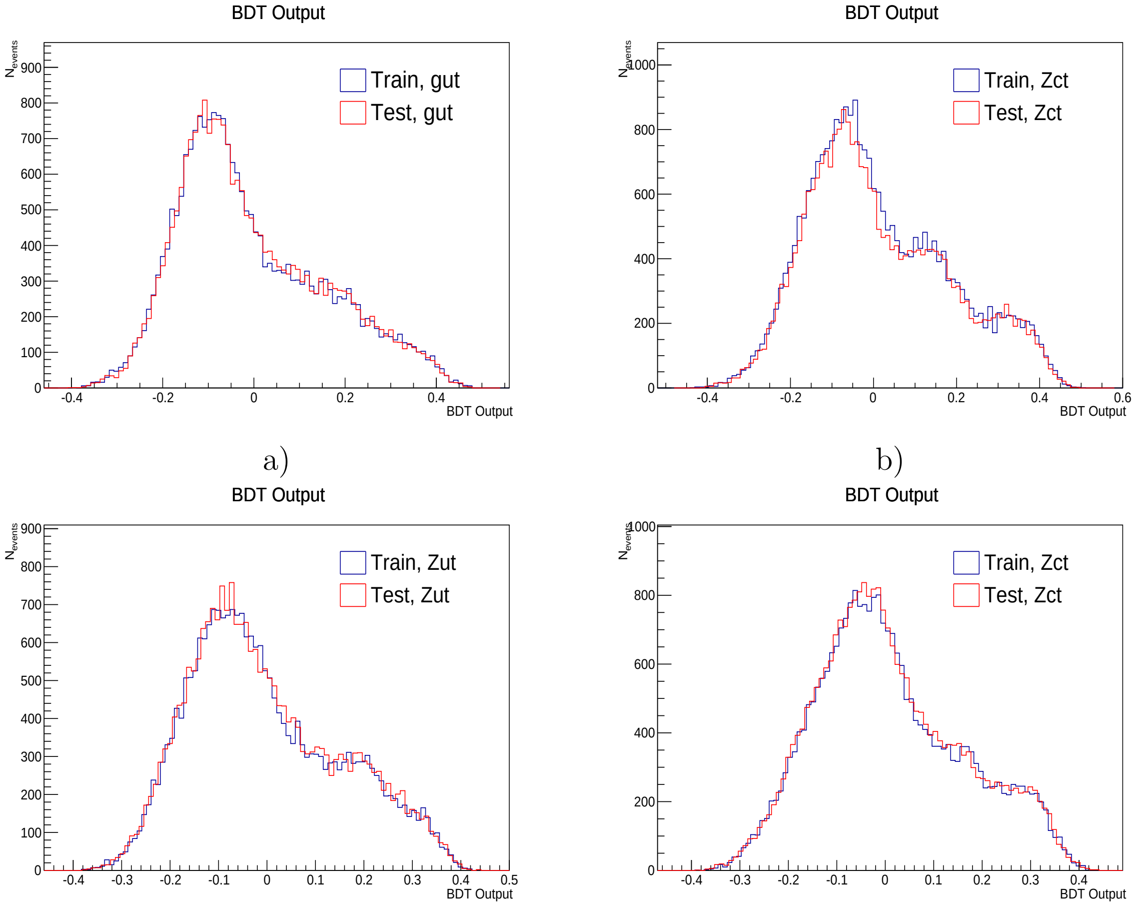

a) b) c) d)

Figure 6.8: BDT output for the events used during the training and testing phase of the BDT for a left-handed a) gut, b) gct, c) Zut and d) Zct anomalous coupling. In each figure the overlap between the distributions is almost complete.

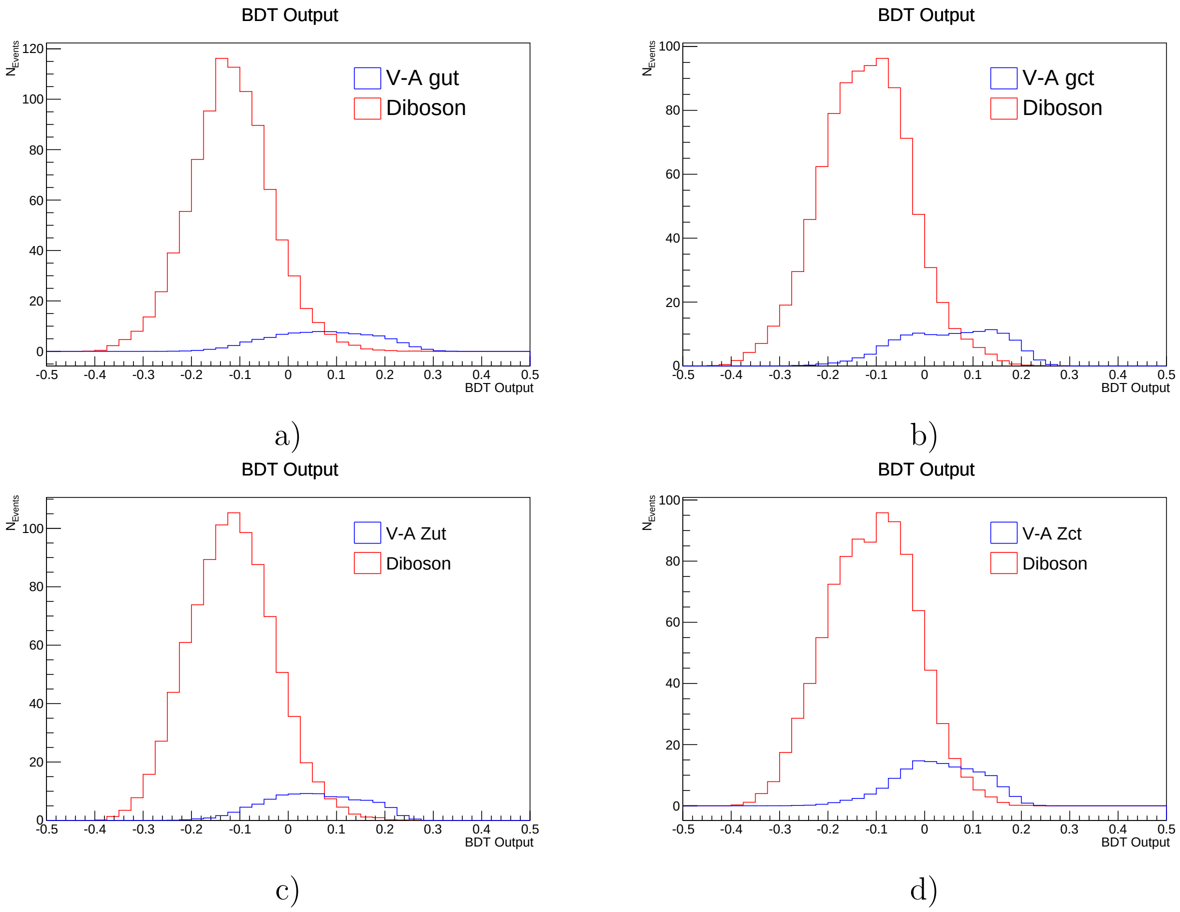

Figure 6.9: BDT output comparison between Diboson processes (WW+jets,WZ+jets,ZZ+jets) and a left-handed (a) gut coupling , (b) gct coupling , (c) Zut coupling and (d) Zct coupling.

Chapter 7

Results

Using a counting experiment upper limits are derived according to the CLs prescription at the 95 % confidence level (C.L.) on the tZ production cross-section through different coupling natures and chiralities. With these cross-section limits we will put limits on anomalous couplings found in the literature. In section 7.1 we briefly describe the CLs method [90, 91] and in section 7.2 limits on anomalous couplings are presented.

7.1 The CLs Method

In particle physics one of the objectives of a search is to either exclude as much as possible the existence of a signal in its absence or to confirm the existence of a true signal as much as possible while the probabilities of discovering a non-existent signal and falsely excluding a true signal at or below specified levels. This is achieved by a hypothesis test. In this context the null hypothesis is that there is no signal while the alternative hypothesis is that the signal exists.

In order to test this hypothesis it is defined a test statistic Q which is optimal when it is the likelihood ratio of Poisson probabilities

$$Q = \frac{P_{poiss}(data|signal + background)}{P_{poiss}(data|background)} \tag{7.1}$$

where for a counting experiment

$$P_{poiss}(data|signal + background) = \frac{(s+b)^n e^{-(s+b)}}{n!} \tag{7.2}$$

and

$$P_{poiss}(data|background) = \frac{b^n e^{-b}}{n!} \tag{7.3}$$

where s and b are the signal and background expected events after an analysis and n is the observed number of events.

Associated to the test statistic Q is a probability distribution P which is used both to test the consistency of the data with the background hypothesis and to test the consistency of the data with the signal plus background hypothesis. Given this we can define the confidence level $1 - CL_b$

$$1 - CL_b = P(Q \geq Q_{obs}|background) \tag{7.4}$$

as well the confidence level CL_{s+b}

$$CL_{s+b} = P(Q \leq Q_{obs}|background) \tag{7.5}$$

The confidence level CLs is then defined as

$$CL_s = \frac{CL_{s+b}}{CL_b} \tag{7.6}$$

A signal hypothesis is excluded at 95 % CL if $CL_s < 0.05$. Because the number of expected signal events s depends on the expected cross-section or other model parameters we can compute upper or lower limits for the values of these unknown quantities. In the particular case of the cross-section, upper limits on the expected cross-section can be computed by solving the equation

$$CL_s(\sigma) = \alpha \tag{7.7}$$

where the fixed value of α is set depending on the chosen confidence level $1 - \alpha$.

7.2 Limits

7.2.1 Anomalous Couplings in the Literature

In the literature it is usual to find limits on the anomalous couplings $\frac{k_{gqt}}{\Lambda}$ and $\frac{k_{Zqt}}{\Lambda}$ with $q = u, c$. Our lagrangian can be written in terms of those anomalous coupling by a change of variables. In the search for tZ production CMS considered the lagrangian

$$\begin{aligned}\mathcal{L} = \sum_{q=u,c} [\sqrt{2} g_s \frac{k_{gqt}}{\Lambda} \bar{t} \sigma^{\mu\nu} T_a (f_q^L P_L + f_q^R P_R) q G^a_{\mu\nu} + \\ + \frac{g}{\sqrt{2} c_W} \frac{k_{Zqt}}{\Lambda} \bar{t} \sigma^{\mu\nu} (\hat{f}_q^L P_L + \hat{f}_q^R P_R) q Z_{\mu\nu}] + h.c. \end{aligned} \tag{7.8}$$

If we do the following assignments

$$\frac{\zeta_{qt}^{R*}}{2m_t} = \sqrt{2} \frac{k_{gqt}}{\Lambda} f_q^L, \qquad \frac{\zeta_{qt}^{L*}}{2m_t} = \sqrt{2} \frac{k_{gqt}}{\Lambda} f_q^R \tag{7.9}$$

$$\frac{K_{qt}^{R*}}{4M_Z} = \frac{\hat{f}_q^L}{\sqrt{2}} \frac{k_{Zqt}}{\Lambda}, \qquad \frac{K_{qt}^{L*}}{4M_Z} = \frac{\hat{f}_q^R}{\sqrt{2}} \frac{k_{Zqt}}{\Lambda} \tag{7.10}$$

in our lagrangian we obtain the same lagrangian used by CMS. Note that what we call as a left-handed coupling ir a right-handed coupling in the CMS lagrangian and vice-versa. From now on we will assume the CMS convention.

7.2.2 Limits On the tZ Production Hypothesis

To compute the limit for a given anomalous coupling with a given handedness we considered four different cuts on the BDT output. More precisely we computed the number of tZ and Diboson events that had a BDT output greater than 0, 0.05, 0.1 and 0.15. With the resulting efficiencies of the signal as well as the number of the Diboson processes we used the CLs method to compute four different cross-section limits at 95 % confidence level. Among the four we choose the smaller cross-section value as our limit. With this value of the cross-section we computed the corresponding limit on the anomalous couplings. In figure 7.1 you can find the limits for each anomalous coupling for both chiralities as well as the theoretical cross-section computed by MadGraph. As can be seen although the limits do not differ more than 5 % , the left-handed limits are inferior to the right-handed limits.

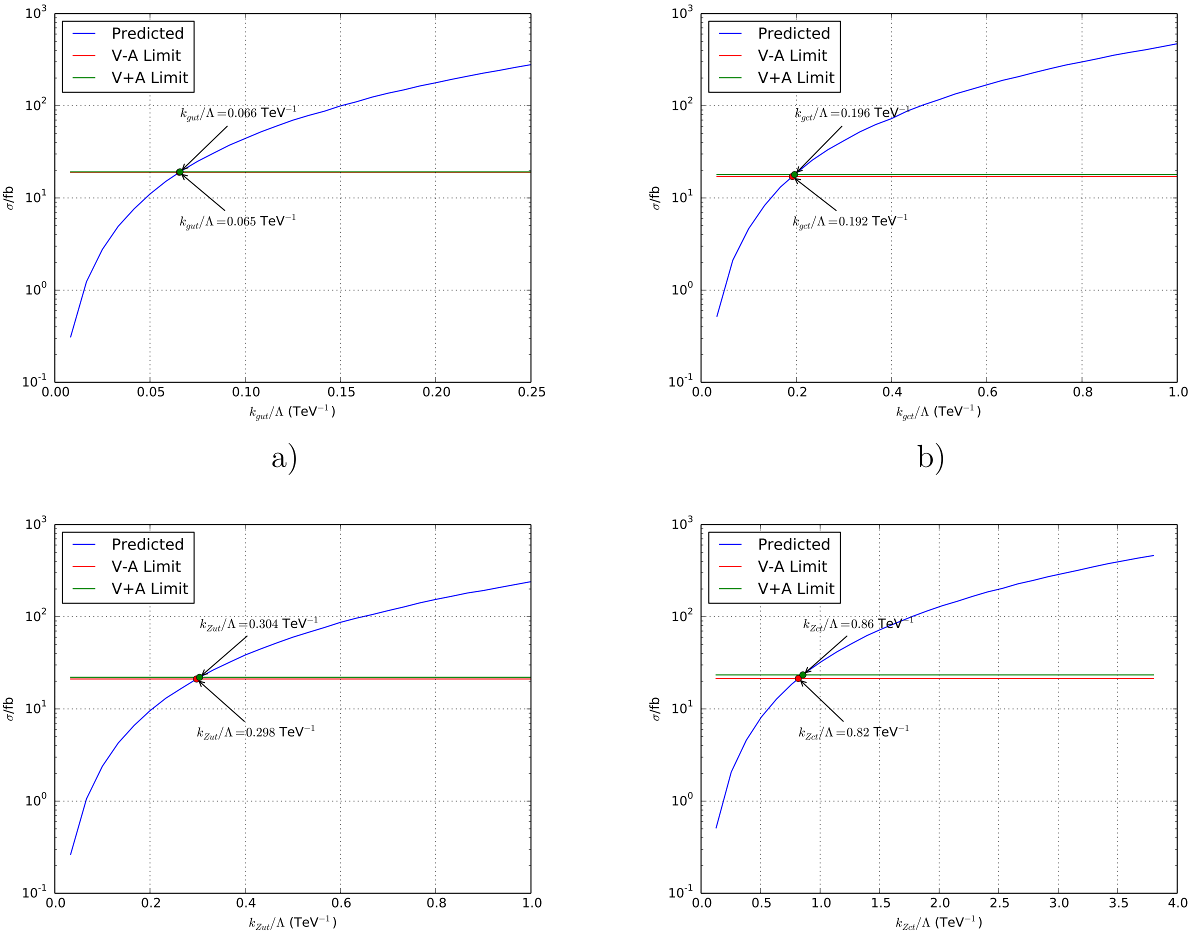

a) b)

c) d)

Figure 7.1: Limits on the anomalous couplings in the case of a left-handed and right-handed coupling. The limits for a gut, gct, Zut and Zct are presented respectively in a), b), c) and d).

Chapter 8

Conclusions and Further Work

In this dissertation we implemented in an UFO model a lagrangian that describes top FCNCs interactions in the context of dimension-six gauge invariant operators. From the parton-level results obtained in sections 5.2, 5.3 and 5.4 we concluded that the coupling nature of the anomalous coupling responsible for the process produces different kinematical distributions of the top quark, of the the boson that is produced with the top as well as of the composite system. In the case of tZ for $\sqrt{s} = 13$ TeV and luminosity of 10 fb^{-1} these differences are reflected in the differences we obtained in the limits on the anomalous couplings : the gut anomalous coupling is the most constrained one while the Zct anomalous coupling is the least constrained. For the tZ production we also observed at parton-level that the chirality of the anomalous coupling changes the kinematics of the decay products of the top quark and Z boson. These changes were also preserved at detector-level simulation. However after a Multivariate Analysis performed with samples generated at $\sqrt{s} = 13$ TeV and luminosity of 10 fb^{-1} we conclude that the differences we achieve in the anomalous couplings limits are not greater than 5 % and that in general the left-handed limit is better than a right-handed limit.

Concerning the limits it is important to keep in mind that they were obtained considering only Diboson events as source of background. To continue this work we should consider the other background events mainly Z+jets. It would also be interesting to study in more detail the effect of the coupling chirality for the case of tγ and tH production. In principle we expect a similar effect but how much the differences would be demands a more detailed study.

Appendices

Appendix A

gtq vertices

According to [53] the relevant operators for the gtc vertex are $O^{32}_{uG\phi}$ and $O^{23}_{uG\phi}$:

$$
\begin{aligned}
O^{32}_{uG\phi} &= (\bar{q}_{L3}\lambda^a\sigma^{\mu\nu}u_{R2})\tilde{\phi}G^a_{\mu\nu} \\
O^{23}_{uG\phi} &= (\bar{q}_{L2}\lambda^a\sigma^{\mu\nu}u_{R3})\tilde{\phi}G^a_{\mu\nu}
\end{aligned}
$$

Since $\bar{q}_{L3} = (\bar{t}_L, \bar{b}_L)$ and $\bar{q}_{L2} = (\bar{c}_L, \bar{s}_L)$ and using the definition of $\tilde{\phi}$ we get

$$
\begin{aligned}
O^{32}_{uG\phi} &= \frac{v+H}{\sqrt{2}}(\bar{t}\lambda^a\sigma^{\mu\nu}P_Rc)G^a_{\mu\nu} \\
O^{23}_{uG\phi} &= \frac{v+H}{\sqrt{2}}(\bar{c}\lambda^a\sigma^{\mu\nu}P_Rt)G^a_{\mu\nu}
\end{aligned}
$$

To the gtc vertex only the term without the Higgs is relevant. Then, our lagrangian is

$$
\mathcal{L}_{gtc} = \frac{C^{32}_{uG\phi}}{\Lambda^2}\frac{v}{\sqrt{2}}(\bar{t}\lambda^a\sigma^{\mu\nu}P_Rc)G^a_{\mu\nu} + \frac{C^{23}_{uG\phi}}{\Lambda^2}\frac{v}{\sqrt{2}}(\bar{c}\lambda^a\sigma^{\mu\nu}P_Rt)G^a_{\mu\nu} + H.c.
$$

Noting that the Hermitian conjugate of $\bar{t}\lambda^a\sigma^{\mu\nu}P_Rc$ is $\bar{c}\lambda^a\sigma^{\mu\nu}P_Lt$ and defining

$$
\begin{aligned}
\zeta^L_{ct} &= \frac{\sqrt{2}}{g_s}C^{32*}_{uG\phi}\frac{vm_t}{\Lambda^2} \\
\zeta^R_{ct} &= \frac{\sqrt{2}}{g_s}C^{23}_{uG\phi}\frac{vm_t}{\Lambda^2}
\end{aligned}
$$

we find the final form of $\mathcal{L}_{gct}$

$$
\mathcal{L}_{gct} = \frac{g_s}{2m_t}\bar{c}\lambda^a\sigma^{\mu\nu}(\zeta^L_{ct}P^L + \zeta^R_{ct}P^R)tG^a_{\mu\nu} + H.c.
$$

The lagrangian describing the gtu interaction is exactly the same with u in the place of c and can be obtained by doing analogous computations with the operators $O_{uG\phi}^{31}$ and $O_{uG\phi}^{13}$.

Appendix B

Ztq and γtq vertices

According to [53] the relevant operators to the vertices Ztc and γtc are $O_{\phi q}^{(3,23)}$, $O_{\phi q}^{(3,32)}$, $O_{\phi q}^{(1,23)}$, $O_{\phi q}^{(1,32)}$, $O_{\phi u}^{23}$, $O_{\phi u}^{32}$, O_{uW}^{32} , $O_{uB\phi}^{32}$, O_{uW}^{23} and $O_{uB\phi}^{23}$. We will start by analyzing the first six operators. All this operators involve the covariant derivative of the Higgs doublet ϕ. Because the doublet does not have colour and ϕ has weak hypercharge 1/2 the covariant derivative of ϕ is

$$D_\mu \phi = (\partial_\mu + i g_W \frac{\tau^I}{2} W_\mu^I + i \frac{g_Y}{2} B_\mu)\phi$$

Using the definition of the Pauli matrices τ^I and the mixing relations between the gauge fields W_μ^I and B_μ with the vector fields $W_\mu^\pm$, Z_μ^0 and A_μ and the fact that $g_Y c_W = g_W s_W = e$ we arrive at the expression

$$D_\mu \phi = \partial_\mu \phi + \frac{i}{2} \begin{bmatrix} g_W \frac{c_W^2 - s_W^2}{c_W} Z_\mu + 2eA_\mu & \sqrt{2} W_\mu^+ \\ \sqrt{2} W_\mu^- & -\frac{g_W}{c_W} Z_\mu \end{bmatrix} \phi$$

Because $\phi = \begin{pmatrix} 0 \\ \frac{v+H}{\sqrt{2}} \end{pmatrix}$ after EWSB we find

$$D_\mu \phi = \begin{pmatrix} i \frac{g_W}{2} (v+H) W_\mu^+ \\ \frac{\partial_\mu H}{\sqrt{2}} - \frac{i g_W}{2 c_W} \frac{(v+H)}{\sqrt{2}} Z_\mu \end{pmatrix}$$

We can finally start to compute the contributions from the first six operators.

$$\begin{aligned}
O_{\phi q}^{(3,23)} &= i(\phi^\dagger \tau^I D_\mu \phi)\bar{q}_{L2}\gamma^\mu \tau^I q_{L3} \\
O_{\phi q}^{(3,32)} &= i(\phi^\dagger \tau^I D_\mu \phi)\bar{q}_{L3}\gamma^\mu \tau^I q_{L2} \\
O_{\phi q}^{(1,23)} &= i(\phi^\dagger D_\mu \phi)\bar{q}_{L2}\gamma^\mu q_{L3} \\
O_{\phi q}^{(1,32)} &= i(\phi^\dagger D_\mu \phi)\bar{q}_{L3}\gamma^\mu q_{L2} \\
O_{\phi u}^{23} &= i(\phi^\dagger D_\mu \phi)\bar{u}_{R2}\gamma^\mu u_{R3} \\
O_{\phi u}^{32} &= i(\phi^\dagger D_\mu \phi)\bar{u}_{R3}\gamma^\mu u_{R2}
\end{aligned}$$

In the first two operators only the term with $I = 3$ contributes to these vertices because it is the only term that couples the top quark with the charm quark. Then we have

$$\phi^\dagger \tau^3 D_\mu \phi = i(0, \frac{v+H}{\sqrt{2}}) \begin{pmatrix} 1 & 0 \\ 0 & -1 \end{pmatrix} \begin{pmatrix} i\frac{g_W}{2}(v+H)W_\mu^+ \\ \frac{\partial_\mu H}{\sqrt{2}} - \frac{ig_W}{2c_W}\frac{(v+H)}{\sqrt{2}}Z_\mu \end{pmatrix} =$$

$$= i(0, \frac{v+H}{\sqrt{2}}) \begin{pmatrix} i\frac{g_W}{2}(v+H)W_\mu^+ \\ -\frac{\partial_\mu H}{\sqrt{2}} + \frac{ig_W}{2c_W}\frac{(v+H)}{\sqrt{2}}Z_\mu \end{pmatrix} = i(-\frac{(v+H)\partial_\mu H}{2} + \frac{ig_W}{2c_W}\frac{(v+H)^2}{2}Z_\mu)$$

From the last expression only terms with the Z boson are relevant to us in this computation so the only relevant term is

$$-\frac{g_W v^2}{4c_W}Z_\mu$$

Also

$$\bar{q}_{L2}\gamma^\mu \tau^3 q_{L3} = (\bar{c}_L, \bar{s}_L)\gamma^\mu \begin{pmatrix} 1 & 0 \\ 0 & -1 \end{pmatrix} \begin{pmatrix} t_L \\ b_L \end{pmatrix} = \bar{c}_L\gamma^\mu t_L - \bar{s}_L\gamma^\mu b_L$$

From this last two expressions we conclude that the first two operators contribute with the terms

$$\begin{aligned}
-\frac{g_W v^2}{4c_W}\bar{c}_L\gamma^\mu t_L Z_\mu &= -\frac{g_W v^2}{4c_W}\bar{c}\gamma^\mu P_L t Z_\mu \\
-\frac{g_W v^2}{4c_W}\bar{t}_L\gamma^\mu c_L Z_\mu &= -\frac{g_W v^2}{4c_W}\bar{t}\gamma^\mu P_L c Z_\mu
\end{aligned}$$

The operators $O_{\phi q}^{(1,23)}$, $O_{\phi q}^{(1,32)}$, $O_{\phi u}^{23}$ and $O_{\phi u}^{32}$ will contribute respectively with the terms

$$\begin{aligned}
&\frac{g_W v^2}{4c_W}\bar{c}\gamma^\mu P_L t Z_\mu \\
&\frac{g_W v^2}{4c_W}\bar{t}\gamma^\mu P_L c Z_\mu \\
&\frac{g_W v^2}{4c_W}\bar{c}\gamma^\mu P_R t Z_\mu \\
&\frac{g_W v^2}{4c_W}\bar{t}\gamma^\mu P_R c Z_\mu
\end{aligned}$$

Now we compute the contributions from the remaining operators

$$\begin{aligned}
O_{uW}^{32} &= (\bar{q}_{L3}\sigma^{\mu\nu}\tau^I u_{R2})\tilde{\phi}W_{\mu\nu}^I \\
O_{uB\phi}^{32} &= (\bar{q}_{L3}\sigma^{\mu\nu}u_{R2})\tilde{\phi}B_{\mu\nu} \\
O_{uW}^{23} &= (\bar{q}_{L2}\sigma^{\mu\nu}\tau^I u_{R3})\tilde{\phi}W_{\mu\nu}^I \\
O_{uB\phi}^{23} &= (\bar{q}_{L2}\sigma^{\mu\nu}u_{R3})\tilde{\phi}B_{\mu\nu}
\end{aligned}$$

Since $\tilde{\phi} = i\tau^2\phi$ only the term with $I = 3$ of the operators O_{uW}^{32} and O_{uW}^{23} contributes. Using again the the mixing relations between the gauge fields W_μ^3 and B_μ with the vector fields Z_μ^0 and A_μ , O_{uW}^{32} , $O_{uB\phi}^{32}$, O_{uW}^{23} and $O_{uB\phi}^{23}$ will respectively contribute with

$$\begin{aligned}
&\frac{v}{\sqrt{2}}\bar{t}\sigma^{\mu\nu}P_R c(c_W Z_{\mu\nu} + s_W A_{\mu\nu}) \\
&\frac{v}{\sqrt{2}}\bar{t}\sigma^{\mu\nu}P_R c(-s_W Z_{\mu\nu} + c_W A_{\mu\nu}) \\
&\frac{v}{\sqrt{2}}\bar{c}\sigma^{\mu\nu}P_R t(c_W Z_{\mu\nu} + s_W A_{\mu\nu}) \\
&\frac{v}{\sqrt{2}}\bar{c}\sigma^{\mu\nu}P_R t(-s_W Z_{\mu\nu} + c_W A_{\mu\nu})
\end{aligned}$$

After all this computations we are ready to write the lagrangian describing both Ztc and γtc interactions :

$$\begin{aligned}\mathcal{L}_{Ztc}+\mathcal{L}_{\gamma tc}=&\frac{C_{\phi q}^{(3,23)}}{\Lambda^2}(-\frac{g_W v^2}{4c_W}\bar{c}\gamma^\mu P_L t Z_\mu)+\frac{C_{\phi q}^{(3,32)}}{\Lambda^2}(-\frac{g_W v^2}{4c_W}\bar{t}\gamma^\mu P_L c Z_\mu)+\\ &+\frac{C_{\phi q}^{(1,23)}}{\Lambda^2}\frac{g_W v^2}{4c_W}\bar{c}\gamma^\mu P_L t Z_\mu+\frac{C_{\phi q}^{(1,32)}}{\Lambda^2}\frac{g_W v^2}{4c_W}\bar{t}\gamma^\mu P_L c Z_\mu+\frac{C_{\phi u}^{23}}{\Lambda^2}\frac{g_W v^2}{4c_W}\bar{c}\gamma^\mu P_R t Z_\mu+\\ &+\frac{C_{uB\phi}^{23}}{\Lambda^2}\frac{v}{\sqrt{2}}\bar{c}\sigma^{\mu\nu}P_R t(-s_W Z_{\mu\nu}+c_W A_{\mu\nu})+\frac{C_{uW}^{32}}{\Lambda^2}\frac{v}{\sqrt{2}}\bar{t}\sigma^{\mu\nu}P_R c(c_W Z_{\mu\nu}+s_W A_{\mu\nu})+\\ &+\frac{C_{uB\phi}^{32}}{\Lambda^2}\frac{v}{\sqrt{2}}\bar{t}\sigma^{\mu\nu}P_R c(-s_W Z_{\mu\nu}+c_W A_{\mu\nu})+\frac{C_{uW}^{23}}{\Lambda^2}\frac{v}{\sqrt{2}}\bar{c}\sigma^{\mu\nu}P_R t(c_W Z_{\mu\nu}+s_W A_{\mu\nu})+\\ &+\frac{C_{\phi u}^{32}}{\Lambda^2}\frac{g_W v^2}{4c_W}\bar{t}\gamma^\mu P_R c Z_\mu+H.c.\end{aligned}$$

The Hermitian conjugates of $\bar{t}\gamma^\mu P_L c$ and $\bar{t}\sigma^{\mu\nu}P_R c$ are $\bar{c}\gamma^\mu P_L t$ and $\bar{c}\sigma^{\mu\nu}P_L t$ respectively. If we define

$$\begin{aligned}X_{ct}^L&=\frac{1}{2}\frac{v^2}{\Lambda^2}[C_{\phi q}^{(3,23)}+C_{\phi q}^{(3,3w)*}-C_{\phi q}^{(1,23)}-C_{\phi q}^{(1,32)*}]\\ X_{ct}^R&=-\frac{1}{2}\frac{v^2}{\Lambda^2}[C_{\phi u}^{23}+C_{\phi u}^{32*}]\\ K_{ct}^L&=\sqrt{2}\frac{v^2}{\Lambda^2}(c_W C_{uW}^{32*}-s_W C_{uB\phi}^{32*})\\ K_{ct}^R&=\sqrt{2}\frac{v^2}{\Lambda^2}(c_W C_{uW}^{23}-s_W C_{uB\phi}^{23})\\ \lambda_{ct}^L&=\frac{\sqrt{2}}{e}\frac{vm_t}{\Lambda^2}(s_W C_{uW}^{32*}+c_W C_{uB\phi}^{32*})\\ \lambda_{ct}^R&=\frac{\sqrt{2}}{e}\frac{vm_t}{\Lambda^2}(s_W C_{uW}^{23*}+c_W C_{uB\phi}^{23*})\end{aligned}$$

and remembering that $m_W=g_W v/2$ and $m_W=m_Z c_W$ we finally arrive at

$$\begin{aligned}\mathcal{L}_{Zct}+\mathcal{L}_{\gamma ct}=&-\frac{g_W}{2c_W}\bar{c}\gamma^\mu(X_{ct}^L P_L+X_{ct}^R P_R)tZ_\mu+\frac{g_W}{4c_W m_Z}\bar{c}\sigma^{\mu\nu}(K_{ct}^L P_L+K_{ct}^R P_R)tZ_{\mu\nu}+\\ &+\frac{e}{2m_t}\bar{c}\sigma^{\mu\nu}(\lambda_{ct}^L P_L+\lambda_{ct}^R P_R)tA_{\mu\nu}+H.c.\end{aligned}$$

The same lagrangian for couplings with the u quark can be obtained with the same procedure but using the same operators with 2 → 1 in the upper index. The result is basically the same with the u quark field replacing the c quark field.

Bibliography

[1] UA1 Collaboration, "Observation of single isolated electrons of high transverse momentum in events with missing transverse energy at the CERN $\bar{p}p$ collider", Physics Letters B Vol. 122, 103-116, 1983.

[2] UA2 Collaboration, "Experimental observation of isolated large transverse energy electrons with associated missing energy a $\sqrt{s} = 540$ GeV", Physics Letters B Vol. 122, 476-485, 1983.

[3] UA1 Collaboration, "Experimental observation of lepton pairs of invariant mass around 95 GeV/c^2 at the CERN SPS collider", Physics Letters B Vol. 126 , 398-410, 1983

[4] D0 Collaboration, "Observation of the top quark", Phys. Rev. Lett. Vol. 74 , 2632-2637 1995

[5] CDF Collaboration, "Observation of the top quark in $\bar{p}p$ collisions", Phys. Rev. Lett. Vol. 74 , 2626-2631 1995

[6] ATLAS Collaboration, "Observation of a new particle in the search for the Standard Model Higgs boson with the ATLAS detector at the LHC", Physics Letters B, Vol. 716 ,1, 2012

[7] CMS Collaboration, "Observation of a new boson at a mass of 125 GeV with the CMS experiment at the LHC", Physics Letters B, Vol. 716, 30, 2012

[8] L. Susskind, "Dynamics of spontaneous symmetry breaking in the Weinberg-Salam theory", Phys.Rev. D 20 , 2619, 1979

[9] J.Ellis , "Outstanding questions : physics beyond the Standard Model", Phil. Trans. R. Soc. A 370, 818-830, 2012

[10] P. Langacker, "Introduction to the Standard Model and Electroweak Physics", arXiv:0901.0241 [hep-ph], 2009

[11] J. Lykken, "Introduction to Supersymmetry", arXiv:hep-th/9612114, 1996

[12] E. Ponton, "TASI 2011 : Four Lectures on TeV Scale Extra Dimensions", arXiv:1207.3827, 2012

[13] R. Contino, "TASI 2009 lectures : The Higgs as a Composite Nambu-Goldstone Boson", arXiv:1005.4269, 2010

[14] J.A. Aguilar-Saavedra, R. Benbrik, S. Heinemeyer, M. Prez- Victoria, "Handbook of vector-like quarks : mixing and single production", arXiv:1306.0572, 2013

[15] ATLAS,CDF,CMS,D0 Collaborations, "Combination of Tevatron and LHC measurements of the top-quark mass", arXiv:1403.4427 [hep-ex], 2014

[16] S.L. Glashow, J. Iliopoulos, L. Maiani, "Weak Interactions with Lepton–Hadron Symmetry", Phys. Rev. D **2**(7):1285

[17] CDF Collaboration, "Search for the flavour changing neutral current decay $t \to Z^0 q$ in $p\bar{p}$ collisions at $\sqrt{s} = 1.96$ TeV, Phys.Rev. Lett. 101 (2008) 192002

[18] D0 Collaboration, "Search for flavor changing neutral currents in decays of top quarks", Phys. Lett. B 701 (2011) 313

[19] CMS Collaboration, "Search for Flavour-Changing Neutral Currents in tZ events in proton-proton collisions at $\sqrt{s} = 7$ TeV" CMS PAS TOP-12-021, 2013

[20] ATLAS Collaboration, "Search for single top-quark production via FCNC in strong interac- tions in $\sqrt{s} = 8$ TeV ATLAS data", ATLAS-CONF-2013-063, 2013

[21] CMS Collaboration, Search for anomalous single top quark production in association with a photon in pp collisions at $\sqrt{s} = 8$ TeV, CMS PAS TOP-14-003, 2014

[22] ALEPH Collaboration, "Search for Single Top Production in e^+e^- Collisions at $\sqrt{s}$ up to 209 GeV", arXiv:hep-ex/0206070v1, 2002

[23] DELPHI Collaboration, "Search for single top production via FCNC at LEP at $\sqrt{s} = 189 - 208$ GeV", arXiv:hep-ex/0404014v1, 2004

[24] L3 Collaboration, "Search for Single Top Production at LEP", arXiv:hep-ex/0210041v1, 2002

[25] OPAL Collaboration, "Search for Single Top Quark Production at LEP2", arXiv:hep-ex/0110009v1, 2001

[26] H1 Collaboration, "Search for Single Top Quark Production at HERA", Phys. Lett. B678, 450 (2009).

[27] ZEUS Collaboration, "Search for single-top production in ep collisions at HERA", arXiv:1111.3901, 2011

[28] ATLAS Collaboration, Top Physics Combined Summary Plots, https://atlas.web.cern.ch/Atlas/GROUPS/PHYSICS/CombinedSummaryPlots/TOP/, Accessed : 24/10/2015

[29] M. Y. Han, Y. Nambu, "Three-triplet model with double SU(3) symmetry", Phys.Rev. 139 (1965) B1006–B1010

[30] O. Greenberg, "Spin and Unitary Spin Independence in a Paraquark Model of Baryons and Mesons", Phys.Rev.Lett. 13 (1964) 598–602

[31] D.J. Gross, F. Wilczek, Ultraviolet Behavior of Non-Abelian Gauge Theories, Phys.Rev.Lett. 30, 1343, 1973

[32] H.D. Politzer, "Reliable Perturbative Results for Strong Interactions ?", Phys.Rev.Lett. 30, 1346 1973

[33] P. Skands, "Introduction to QCD", arXiv:1207.2389 [hep-ph], 2012

[34] "The Nobel Prize in Physics 1979", Nobelprize.org. Nobel Media AB 2014. Web. Accessed : 24/10/2015

[35] F. Englert, R. Brout, "Broken Symmetry and the Mass of Gauge Vector Mesons", Phys. Rev. Lett. 13, 321-323 1964

[36] P. Higgs, "Broken Symmetries and the Masses of Gauge Bosons", Phys. Rev. Lett. 13, 508-509, 1964

[37] G.S. Guralnik, C.R. Hagen, T.W.B. Kibble, "Global Conservation Laws and Massless Particles", Phys. Rev. Lett. 13, 585-587, 1964

[38] K.A. Olive et al. (Particle Data Group), "Review of Particle Physics", Chinese Physics C Vol. 38, No. 9 (2014) 090001

[39] T. Inami, C.S. Lim , Effects of Superheavy Quarks and Leptons in Low-Energy Weak Processes $K_L \to \mu\bar{\mu}$, $K^+ \to \pi^+\nu\bar{\nu}$ and $K^0 \leftrightarrow \bar{K}^0$, Prog. Theor. Phys. Vol. 65,N°1, 1981

[40] G. Buchalla , J. Buras, Two-Loop Large-m_t Electroweak Corrections to $K \to \phi\nu\nu$ for Arbitrary Higgs Boson Mass, arXiv:hep-ph/9707243, 1997

[41] J.A. Aguilar-Saavedra, Top flavour changing neutral interactions: theoretical expectations and experimental detection, arXiv:hep- ph/0409342v4, 2004

[42] G.A. González-Sprinberg, R. Martínez, J.-A. Rodriguez, FCNC top quark decays in extra dimensions, Eur. Phys. J. C 51, 919–926, 2007

[43] T.-J. Gao, T.-F. Feng, J.-B. Chen, $t \to cg$ and $t \to cg$ in warped extra dimensions, arXiv:1303.0082 [hep-ph], 2013

[44] S.Casagrande, F. Goertz, U. Haisch, M. Neubert, T. Pfoh, Flavor Physics in the Randall-Sundrum Model I. Theoretical Setup and Elec-troweak Precision Tests, arXiv:0807.4937v3, 2008

[45] P.M. Ferreira, O. Oliveira, R. Santos, "Flavour changing strong interaction effects on top quark physics at the LHC", arXiv:hep-ph/0510087, 2005

[46] P.M. Ferreira, R. Santos, "Strong flavour changing effective operator contributions to single top quark production", arXiv:hep-ph/0601078v3, 2006

[47] R. Davis, D.S. Harmer, K.C. Hoffman, "Search for Neutrinos from the Sun", Phys. Rev. Lett. 20, 1205-1209, 1968

[48] Q. Ahmad et al. (SNO Collaboration), "Measurement of the Rate of $\nu_e + d \to p + p + e^-$ Interactions Produced by ^{8}B Solar Neutrinos at the Sudbury Neutrino Observatory", Phys. Rev. Lett. 87, 2001

[49] Y.Fukudae, et al. (Super-Kamiokande Collaboration), "Evidence for Oscillation of Atmospheric Neutrinos", Phys. Rev. Lett. 81, 1562-1567, 1998

[50] F.P. An, et al. (Daya Bay Collaboration), "Observation of Electron-Antineutrino Disappearance at Daya Bay", Phys. Rev. Lett. 108 (17), 2012

[51] K. Soo-Bong; for RENO Collaboration, "Observation of Reactor Electron Antineutrino Disappearance in the RENO Experiment", arXiv:1204.0626[hep-ex], 2012

[52] N.Agafonova, et. al. (OPERA Collaboration), "Observation of a first ν_τ candidate event in the OPERA experiment in the CNGS beam", Phys. Rev. Lett. B 691, 138-145, 2010

[53] J.A. Aguilar Saavedra, A minimal set of top anomalous couplings, arXiv:0811.3842v2 [hep-ph], 2008

[54] J.A. Aguilar Saavedra, A minimal set of top-Higgs anomalous couplings, arXiv:0904.2387v2 [hep-ph], 2009

[55] ATLAS Collaboration, The ATLAS Experiment at the CERN Large Hadron Collider, JINST 3 S08003, 2008

[56] CMS Collaboration, The CMS Experiment at the CERN LHC, JINST 3 (2008) S08004, 2008

[57] ALEPH Collaboration, DELPHI Collaboration, L3 Collaboration, OPAL Collaboration, SLD Collaboration, Precision Electroweak Measurements on the Z Resonance, arxiv-hep-ex/0509008, 2005

[58] NA48 Collaboration, "A new measurement of direct CP violation in two pion decays of the neutral kaon", Phys. Lett. B 465 (1–4), 335–348, 1999

[59] O.S. Brüning, et al., "LHC Design Report", CERN-2004-003-V-1, 2004

[60] "Large Hadron Collider on a map", http://scienceplx.com/the-large-hadron-collider-all-you-need-to-know-about-the-worlds-most-expensive-experiment-ever/, Accessed : 24/10/2015

[61] M. C. N. Fiolhais, "Study of the wtb vertex structure in top quark decays with the atlas experiment and future prospects", CERN-THESIS-2012-305, 2012

[62] "The ATLAS Detector", http://scipp.ucsc.edu/personnel/atlas.html, Accessed : 24/10/2015

[63] T. Sakuma, T. McCauley, "Detector and event visualization with SketchUp at the CMS experiment", J.Phys: Conf. Ser. 513 (2014) 022032

[64] J. Nielsen, "Fundamentals of LHC Experiments", arXiv:1106.2516 [hep-ex], 2011

[65] N.F.S.F Castro, "Study of the Wtb vertex structure at the ATLAS experiment", CERN-THESIS-2008-083, 2008

[66] D. Froidevaux, P. Sphicas, "General-Purpose Detectors For the Large Hadron Collider", Annu. Rev. Nucl. Part. Sci. 2006. 56:375–440, 2006

[67] R.P. Feynman, "The Behaviour of Hadron Collisions at Extreme Energies", High Energy Collisions: Third International Conference at Stony Brook N.Y, pp 237-249, 1969

[68] G. Altarelli, G. Parisi, "Asymptotic Freedom in Parton Language", Nucl. Phys. B126 (1977) 298, 1977

[69] Yu.L. Dokshitzer, "Calculation of structure functions of deep-inelastic scattering and e+e- annihilation by perturbation theory in quantum chromodynamics", Sov.Phys. JETP 46:641 (1977), 1977

[70] V.N. Gribov, L.N. Lipatov, Sov.J.Nucl.Phys. 15:438 (1972)

[71] S. Agostinelli et al. , GEANT4- a simulation toolkit, Phys.Research Sec. A: Accel. ,Spect. , Detect. and Assoc. Equip. , Vol. 506, 3, 250-303 2003

[72] J. Alwall et al, "The automated computation of tree-level and next-to-leading order differential cross sections, and their matching to parton shower simulations", arXiv:1405.0301 [hep-ph], 2014

[73] M. Bahr, "Herwig++ Physics and Manual", arXiv:0803.0883, 2009

[74] T. Sjostrand, S. Mrenna, P. Skands, "PYTHIA 6.4 Physics and Manual", arXiv:hep-ph/0603175, 2006

[75] J. de Favereau et al, DELPHES 3, A modular framework for fast simulation of a generic collider experiment, arXiv:1307.6346v3 [hep-ex], 2013

[76] A. Alloul, N. Christensen, C. Degrande, C. Duhr, B. Fuks, "FeynRules 2.0 - A complete toolbox for tree-level phenomenology", arXiv:1310.1921, 2013

[77] C. Degrande, C. Duhr, B. Fuks, D. Grellscheid, O. Mattelaer, T. Reiter, UFO - The Universal FeynRules Output, Comput. Phys. Commun. 183 (2012) 1201-1214 [1108.2040]

[78] A. Amorim et. al., "FCNC Top interactions", http://feynrules.irmp.ucl.ac.be/wikiGeneralFCNTop, Access : 25/10/2015

[79] E. S. Swanson, "Aspects of confinement: A brief review", AIP Conf. Proc. 717 (2004) 636–645 [arXiv:hep-ph/0310089]

[80] B.R. Webber, "Fragmentation and hadronization", arXiv:hep-ph/9912292, Proceedings of 19th International Symposium on Lepton and Photon Interactions at High-Energies (LP 99), Stanford, California, 9-14 Aug 1999, pp 577-606,

[81] B. Andersson, G. Gustafson, G. Ingleman, T. Sjostrand, "Parton Fragmentation and String Dynamics", Phys. Rept. 97 (1983) 31-145

[82] G. Marchesini, B.R. Webber, "Simulation of QCD Jets Including Soft Gluon Interference", Nucl.Phys. B283 (1984) 1

[83] G. Marchesini, B.R. Webber, "Monte Carlo Simulation of General Hard Processes and Coherent QCD Radiation", Nucl.Phys. B310 (1988) 461

[84] M. Cacciari, G.P. Salam, G.Soyez, "FastJet User Manual", Eur. Phys. J. C72 (2012) 1896 [1111.6097]

[85] E. Conte, B. Fuks, G. Serret, "MadAnalysis 5, a user-friendly framework for collider phenomenology", Comp. Phys. Comm. 184, 1, pp. 222-256, 2013

[86] E. Conte, B. Dumont, B. Fuks, C. Wymant, "Designing and recasting LHC analyses with MadAnalysis 5", arXiv:1405.3982 [hep-ph], 2014

[87] R.D.Ball, V.Bertone, S.Carrazza, C.S.Deans, L. Del Debbio, S. Forte, A. Guffanti, N.P. Hartland et al. , Parton distributions with LHC data, Nucl. Phys. B 867 (2013) 244 [arXiv:1207.1303[hep-ph]], 2013

[88] NNPDF Collaboration, R. D. Ball, V. Bertone, S. Carrazza, L. Del Debbio, S. Forte, A. Guffanti, N. P. Hartland,J. Rojo, Parton distributions with QED corrections, Nucl.Phys. B877 (2013) 290–320, 2013:q

[89] A. Hocker, P. Speckmayer J. Stelzer, J. Therhaag, E. von Toerne, H. Voss et. al. TMVA 4 -Toolkit for Multivariate Data Analysis with ROOT Users Guide, arXiv:physics/0703039 , 2007

[90] T. Junk, "Confidence level computation for combining searches with small statistics", Nucl. Insturm. Meth. A434:435, 1999

[91] A.L. Read, "Presentation of search results : The CL(s) technique", J. Phys., G28:2693, 2002